ABSTRACT

Title of Dissertation: MODEL-BASED ESTIMATION AND CONTROL FOR LITHIUM-SULFUR BATTERIES

Chu Xu
Doctor of Philosophy, 2021

Dissertation Directed by: Professor Hosam K. Fathy
Department of Mechanical Engineering

This dissertation examines the challenge of (i) estimating the internal states of lithium-sulfur (Li-S) batteries based on an experimentally-parameterized multi-physics model, and (ii) optimizing the discharge trajectory to maximize the energy release of a Li-S battery over a fixed time horizon. This research is motivated both by the potential of Li-S batteries to provide higher energy densities compared to traditional lithium-ion batteries and the potential of model-based estimation/control to improve the performance of a Li-S battery. Previous work in the literature optimizes the materials used in Li-S batteries for better performance, and also develops multiple types of models for these batteries, ranging from simple equivalent circuit models (ECMs) to sophisticated diffusion-reaction models. The dissertation builds on the insights from the existing literature, and focuses on the control-oriented study/analysis of Li-S batteries. From the battery management perspective, the essential components include a computationally tractable model, an internal state estimator, and eventually an optimal control strategy. This research addresses the

gaps corresponding these key components.

First, this dissertation explores the problem of parameterizing a zero-dimensional physics-based Li-S model. Due to the dependency between the parameters, a simulation-based sensitivity study is performed to provide guidance on the choice of to-be-identified parameters. These parameters are identified by fitting the simulated voltage profile to the experimental data for four models considering different reaction chains. The best fitted model is suggested for the following state estimation study.

Second, there is a need for online state estimation algorithms that take into account the multiplicity of active species in Li-S batteries. This dissertation addresses this gap by developing a model-based unscented Kalman filter for state estimation in Li-S batteries, using the parameterized zero-dimensional model. Simulation-based analysis and study is performed to validate the estimator. This uncovers fundamental insights regarding the observability of Li-S battery states, particularly in the low plateau region.

Third, this dissertation demonstrates the fundamental insight that battery SOC estimation accuracy can benefit from the dependence of battery resistance on SOC. Fisher information is used for developing this fundamental insight, based on a first-order equivalent circuit battery model. Moreover, experimental data from laboratory prototype coin cells are used to parameterize the equivalent circuit model, and the model is utilized in a Monte Carlo simulation study to support this theoretical insight. The simulation study shows a 50% improvement in SOC estimation accuracy in the low plateau region, where the slope of open-circuit battery voltage

with respect to SOC is particularly shallow.

Fourth, this dissertation examines the problem of optimizing the discharge trajectory of a Li-S battery to maximize its energy release over a fixed time horizon. This optimization study utilizes a coupled thermal/electrical equivalent circuit model, based on the existing literature, that captures the dependence of battery resistance on both temperature and state of charge. The optimization problem is solved using direct collocation. Simulation results show that trajectory optimization improves total energy delivery over a 2-hour time window compared to both constant-current and constant-power discharge.

The overall outcomes of this dissertation include insights/algorithms that can be implemented into battery management systems to improve the performance of Li-S batteries. These outcomes cover model parameterization/reformulation, state estimation, and optimal control.

MODEL-BASED ESTIMATION AND CONTROL FOR LITHIUM-SULFUR BATTERIES

by

Chu Xu

Dissertation submitted to the Faculty of the Graduate School of the
University of Maryland, College Park in partial fulfillment
of the requirements for the degree of
Doctor of Philosophy
2021

Advisory Committee:
Dr. Hosam K. Fathy, Chair/Advisor
Dr. Chunsheng Wang
Dr. Balakumar Balachandran
Dr. Miao Yu
Dr. Michael G. Pecht
Dr. Paul Stephen Albertus

Acknowledgments

As I put together this dissertation, mixed emotions arise: the gratitude to all the people who care about me and helped me, the sadness of ending this journey, the excitement to make a new beginning, and the pride of conquering the physical illness. I believe these emotions will expand even more later, and will provide me the courage to keep learning and exploring. I will cherish this experience forever, no matter where I am.

I would like to sincerely thank my advisor Dr. Hosam Fathy for giving me the priceless guidance, help, and support through our my Ph.D. journey. He has always made time for us when we need help and advice, even with his crazy schedule. He is always passionate about teaching, and devotes tremendous time to hold boot camps for the lab. He has built a lab with friendly members, diverse culture, inspiring environment, productive atmosphere, and open communication. He encourages me to believe that I could be an awesome scholar and our research could make a difference to the society. I am extremely lucky to have an advisor who cared so much about his students. It has been a pleasure to work with and learn from such an extraordinary individual. Additionally, I would like to thank Dr. Donghai Wang for providing us the opportunity to learn the battery fabrication process. I would like to thank Dr. Chris Rahn and Dr. Rajesh Rajamani for their valuable inputs. I also would like to

thank the members of my Ph.D. committee, Dr. Chunsheng Wang, Dr. Balakumar Balachandran, Dr. Miao Yu, Dr. Michael G. Pecht, Dr. Paul Stephen Albertus for their helpful research advice and suggestions.

I am always thankful to my families for their unconditional love and care. I would like to thank my mom, Yunxiang Ma, who has faith in me and has supported me when I made my decision to pursue a Ph.D. degree. I would not have made it this far without her encouragement. I would like to thank my husband, Dr. Yiming Wang, for being calm and caring when times are rough. These past several years have not been an easy ride, both academically and personally, but I know I always have him to count on. I truly thank Yiming for sticking by my side, even when I was irritable, depressed, or sick. I feel that what we both learned a lot about life and strengthened our determination to live life to the fullest.

I want to thank all the previous members of the COOL lab, Ji, Partha, Abdullah, Donald, and Michelle. They are so nice, friendly, and at the same time, extremely knowledgeable about control and optimization. I hope them best of luck in their future endeavors. I also would like to thank the present members of the lab. Mahsa is my best friend here in US, who provides me so much help in both research and life. She is so wonderful and cheerful with a big smile on her face. She is an awesome cook, a warming host, a caring friend, an enthusiastic scholar, a passionate teacher, and a sister I always wanted to have. I am sure she will have a bright future as a loving professor in academics. Xiaoling is the most calm, patient and peaceful person I have ever known. I am thankful that he connects me with a lot of friends and we had great hotpot parties in Penn State. I always love Manuel's

presentations because of all these cool demonstration videos. I can feel his passion for both research and life. I also love Miguel's presentations, because he explains things so clearly with perfect logic. He is nice, honest, and has good advice in everything. It was real fun to work with Deba in the Mechatronics class. And it was great experience to collaborate with Tim in the Li-S research.

I would like to thank all my friends in China for their support and company. I also would like to thank my housemates at my place of residence for introducing me to the world of music and art.

Lastly, I want to thank those who are not mentioned, who show kindness to others, who provide helps, who smile at strangers, who express empathy, because you are making the world a better place.

Table of Contents

List of Tables

List of Figures

Nomenclature

A	Magnitude of the sine wave (Chapter 5); Surface area of the battery (Chapter 6)
a_v	Active reaction area
a_v^0	Initial active reaction area
C_p	Effective specific heat capacity of the battery
e_k	Measurement noise at time step k
$\boldsymbol{e}$	Measurement noise vector
E_j	Reduction potential for reaction j
E_j^0	Standard reduction potentials
F	Faraday's constant
$\boldsymbol{F}$	Fisher information matrix
F_1	Fisher information generated by the first external current input
F_2	Fisher information generated by the second external current input
F_M	Fisher information matrix
h	Convection heat transfer coefficient
i	Sulfur species index
i_j	Current generated by reaction j
i_j^0	Exchange current density
I	Input (discharge) current
j	Reaction index
J	Objective function of an optimization problem
k	Time step index
k_p	Precipitation rate constant
K_k	Kalman gain at time step k
m	Mass of the battery
m_i	Mass of species i
m_i^0	Initial mass of species i
m_{S_p}	Mass of precipitated sulfur
M_S	Molar mass of a sulfur atom
M_{tot}	Total sulfur mass
n_{S_i}	Number of sulfur atoms in species i
n_j	Number of electrons exchanged in reaction j
N	Total number of the time steps
p	Number of reactions

p_i	Polynomial coefficient
P_{rev}	Reversible heat generation
P_{irrev}	Irreversible heat generation
P_0	Initial covariance matrix
P_k	Covariance matrix at time step k
P_{xz}	Cross-correlation covariance
P_z	Measurement covariance
q	Number of species
Q	Charge capacity of the battery
Q_k	Covariance of the process noise at time step k
R	Gas constant
R_0	Internal resistance
R_k	covariance of the measurement noise at time step k
s_i	Sigmoid function coefficient
$s_{i,j}$	Stoichiometric coefficients
S_{sat}	Saturation mass of S^{2-}
$\boldsymbol{S}$	Sensitivity matrix
t_{end}	End time of the optimization
T	Room temperature (Chapter 3&4); Total experiment time (Chapter 5); Battery temperature (Chapter 6)
T_{amb}	Ambient temperature
T_{end}	End time of the experiment
$\hat{T}_{end}$	End time of the simulation
u	External current input
u_0	A constant external current input
u_1	The first external current input
u_2	The second external current input
u_k	External current input at time step k
U_{oc}	Open circuit voltage
v	Cell volume
v_k	Process noise at time step k
V	Output voltage across the cell
V_{cutoff}	Cutoff voltage
$V_{m,k}$	Measured output voltages at time step k
$\hat{V}_k$	Estimated and measured output voltages at time step k
$\bar{V}$	Equilibrium cell voltage
w_k	Measurement noise at time step k
W_0^τ	Empirical observability gramian
x	SOC of the battery (Chapter 5)

	The total charge transferred out of the battery (Chapter 6)
x_0	Initial SOC
X_0	Initial states
$\hat{x}_0$	Estimated SOC of the battery
$\bar{x}$	Equilibrium SOC
$\hat{X}_0$	Estimated initial state
Y_k	A fictitious output variable at time step k
$\boldsymbol{Y}$	Cell voltage measurement vector
Z_k	Estimated measurement at time step k
α	Relative porosity
α_w	Weight factor in the optimization formulation
β	Tuning factor in UKF (Chapter 4);
	Slope of the internal resistance w.r.t. SOC (Chapter 5)
γ	Power of the relative porosity (Chapter 3&4);
	Slope of the open circuit voltage w.r.t. SOC (Chapter 5)
δt	Sampling time step
ε	A positive perturbation on the initial state
η_j	Overpotential for reaction j
$\boldsymbol{\theta}$	To-be-identified parameter vector
κ	Tuning factor in UKF
λ	Scaling factor in UKF
μ	Similitude scaling factor
σ_v	Standard deviation of the voltage measurement noise
τ	Time period of empirical observability gramian
χ_k	Sigma point at time step k
ω	Relative porosity change rate constant (Chapter 3&4);
	Frequency of the sine wave (Chapter 5)

Chapter 1: Introduction

1.1 Motivation

This dissertation examines the problem of estimating the internal states and optimizing the input trajectories of Li-S batteries. The algorithms solving this problem are usually embedded in a battery management system to achieve the best performance of the given battery.

As the performance of Lithium-ion (Li-ion) batteries approaches its practical limit (up to 500 Wh/kg) [1], researchers are actively seeking alternative, high energy density solutions. The Lithium-Sulfur (Li-S) chemistry is one such solution. It has attracted significant attention from the scientific community for at least four reasons. First, the Li-S chemistry offers very attractive theoretical limits for specific capacity (1672 Ah/kg) and specific energy (2600 Wh/kg) [1], significantly higher than the more traditional Lithium-ion chemistry. Prototype Li-S cells have already achieved specific energies around 700 Wh/kg [2]. Second, Li-S batteries have the potential to offer a range of operating temperatures from -40 to 60 °C [3]. This is especially beneficial for low temperature applications. Third, phenomena such as precipitation and the internal charge shuttle effect provide Li-S batteries with some degree of intrinsic overcharge protection [4, 5], thereby making them less vulnera-

ble to catastrophic failure compared to their Li-ion counterparts. Fourth, the use of sulfur, instead of rare earth materials, makes Li-S batteries quite appealing in terms of production cost and environmental footprint [6]. This makes Li-S batteries potentially attractive for applications requiring high specific energies and/or under relatively high/low temperatures, such as electric vehicles, electrically powered aircraft, unmanned underwater vehicles and satellites.

Great efforts have been made to push for the commercialization of Li-S batteries. This includes an extensive literature on addressing key challenges of Li-S batteries from the material/chemistry perspective, such as improving cycle life and inhibiting self-discharge [7, 8, 9, 10, 11], based on a fundamental understanding of the underlying reactions in Li-S batteries [12, 13, 14, 15, 16, 17, 18, 19]. Another important aspect of the technology readiness level of a new battery is the availability of a proper battery management system. An effective management strategy is essential for protecting cells from damage, prolonging battery cycle life, and increasing battery performance metrics such as output power. However, the problem of designing Li-S battery management systems is less explored than traditional Lithium-ion batteries. This is an important challenge because the Li-S chemistry exhibits fundamentally different behaviors compared to more traditional lithium-ion batteries, including the multi-step reaction chain, self-discharge through the shuttling effect, and the coupling between C-rate, temperature and degradation. Underlying insights from the existing lithium-ion battery management literature are not always directly applicable to the Li-S chemistry. This dissertation is part of a complementary effort to improve Li-S battery performance through modeling, estimation and control.

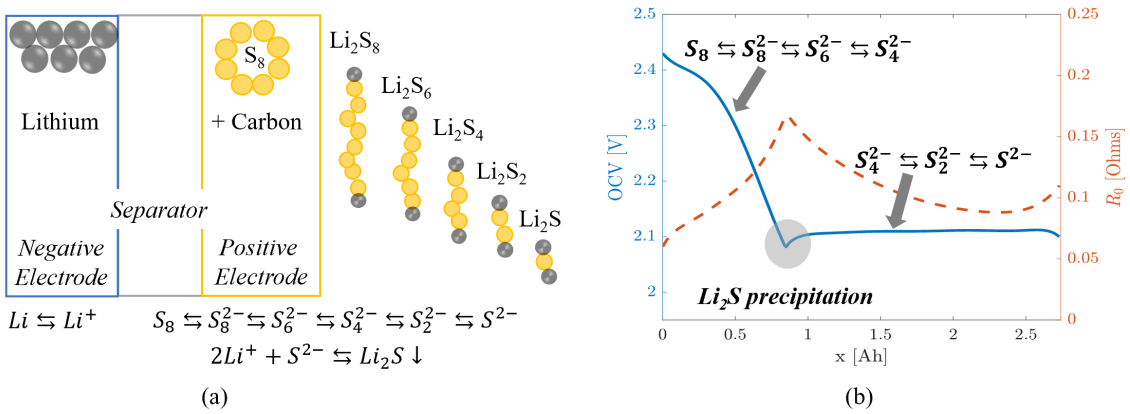

Figure 1.1: (a) Components of the cell and the reactions during discharge (b) Li-S cell voltage profile (constant discharge)

1.2 Working Principle of Li-S Batteries

Liquid electrolyte Li-S batteries consist of pure lithium as an anode, and carbon/sulfur composite as a cathode. During discharge, in the high plateau region, the active material, S_8, in the cathode accepts electrons to produce polysulfides, S_x^{2-} (x can be 8, 6, 4). Further polysulfide reduction takes place in the lower voltage plateau region [20]. In parallel, lithium is oxidized in the anode to furnish lithium ions, diffusing to the cathode side. The half-cell reactions happening in the cell are listed in Fig. 1.1 (a), leading to a full-cell reaction of:

$$16Li + S_8 \rightleftharpoons 8Li_2S \tag{1.1}$$

Due to the low solubility of S^{2-}, there exists precipitation inside the cell, generating a special cell voltage and internal resistance profile under a constant discharge current, as shown in Fig. 1.1 (b). Interestingly, if one wants to write the Nernst equation for the half-cell reactions, a total 5 equations are needed to describe

the cathode reaction chain. The same number of Butler-Volmer equations are needed to describe the relationships between overpotentials and current densities.

The Li-S chemistry suffers from low cycle life and relatively high self-discharge rates [9, 21]. The shuttle effect is the main cause of self-discharge. Since higher-order polysulfides are highly soluble in the common electrolytes used for Li–S batteries [9, 21], they are generated at the positive electrode during discharge, and leaked from the cathode, and then diffuse to the anode. At the anode side, they are reduced to short-chain polysulfide and diffuse back to the cathode. This process, shown in Fig. 1.2, results in the continuous leakage of active material from the cathode, reduced coulombic efficiency, and decreased battery capacity. The initial shuttling may help to create the SEI layer on the anode side, but its insulating property increases the ohmic polarization. The irreversible generation of Li_2S on both electrodes, the side reaction with the electrolyte, and the dendrite formation of lithium will all worsen the cycle life of Li-S batteries. Researchers in the materials/chemistry area have made improvements in prolonging the cycle life and inhibiting self-discharge [7, 8, 9, 10, 11]. This dissertation does not include the shuttle effect as the main focus of the battery management system.

One can identify the key challenges of Li-S batteries from a control perspective. The multi-reaction chain adds complexity to the modeling, parameter identification and estimation of the physics-based model; the nonlinearity and nonmonotonicity of the voltage profile worsens the observability of the system; the coupling between C-rate and temperature affects the output power. This dissertation aims to make contributions related to the above challenges. The goal is to develop algorithms

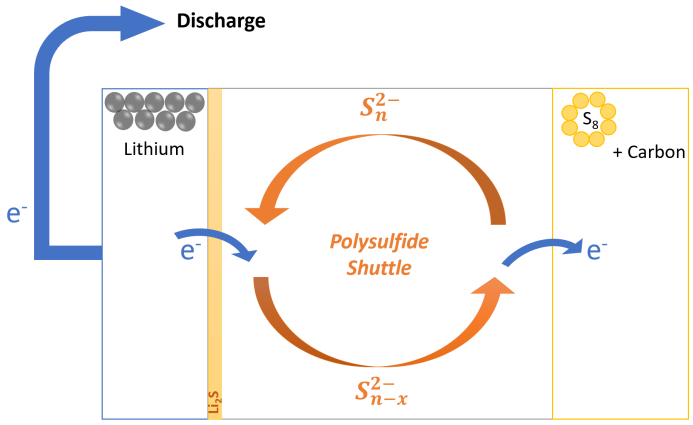

Figure 1.2: The shuttle effect process leading to self-discharge inside Li-S batteries

inside a Li-S battery management system, including a computationally affordable model, a state estimator, and ultimately an optimal control strategy.

1.3 Literature Review

The author reviews the relevant literature of Li-S batteries separately from the perspective of modeling, state estimation, and control, as follows.

1.3.1 Modeling and Parameterization for Li-S Batteries

The current literature on Li-S battery models can be divided into three main categories, namely, spatially-distributed electrochemical models, zero-dimensional electrochemical models, and equivalent circuit models.

Spatially-distributed electrochemical models provide higher fidelity in general, as they are able to include reduction-oxidation, diffusion, migration, precipitation, and self-discharge dynamics in Li-S batteries. White *et al.* introduced the first 1D model along the thickness between the current collectors, based on dilute solution

theory [12]. Other 1D Li-S models [13, 14, 15, 17, 22, 23, 24, 25, 26] contribute more details, such as incorporating size-dependent dissolution [26]. Higher dimensional models are also developed with the consideration of the electrode microstructure/mesostructure [27, 28, 29]. The parameters used in the spatially-distributed electrochemical models are assumed or known based on the experience/knowledge of the thermodynamic properties. Some of the parameter values are manually tuned to fit the capacity of the cell. Parameterization is challenging due to the large number of parameters in the spatially-distributed electrochemical models. However, parameter sensitivity studies are performed to examine the effectiveness/limitation of the 1D Li-S model [30, 31, 32]. The computational complexity of these partial differential algebraic equation (PDAE) Li-S models hinders their implementation into battery management systems.

Zero-dimensional models neglect the diffusion and migration of the species inside Li-S batteries, but use the laws of electrochemistry to model the underlying battery reactions. This approach results in lower-order models with fewer parameters to identify and reduced computational complexity. Simplified two-reaction and multi-reaction zero-dimensional models introduced in [18] and [19] are able to capture the main features of the battery voltage response during discharge. The computational complexity of a zero-dimensional Li-S battery model changes with respect to the specific choice of which reactions to model, and which to ignore. A tank-in-series Li-S model is developed in [33], inside which the cathode and separator are treated as averaged tanks. This model takes into account different phenomena affecting mass flow, including diffusion and migration. The simplification in the

dimension of the zero-dimensional and tank-in-series models provides the potential for real-time applications.

Equivalent circuit models (ECMs) of Li-S batteries typically combine empirical open-circuit voltage maps with (often charge- or temperature-dependent) resistor-capacitor circuits [34, 35, 36, 37, 38, 39]. Parameterization is performed using battery testing techniques such as electrochemical impedance spectroscopy (EIS) [34, 35, 38], Galvanostatic Intermittent Titration technique (GITT) [36], Hybrid Pulse Power Characterization (HPPC) [39], or a mixed charge/discharge impulse test. There is an open opportunity to parameterize zero-dimensional physics-based Li-S battery models given the paucity of the literature on such model parameterization and the computational efficiency of these models. This dissertation begins with the parameter sensitivity and identification of four zero-dimensional models, reflecting different choices of which redox reactions to model. Using this sensitivity analysis, a subset of model parameters is selected for identification. One of the four redox reaction chains is recommended under the proposed model structure based on the parameter identification results. The parameterized zero-dimensional model will be used for the following state estimation study.

1.3.2 State Estimation for Li-S Batteries

Existing research on Li-S battery state estimation relies predominantly on either ECMs or machine learning methods or both. For example, state estimation techniques have been applied to Li-S ECMs in [40, 41, 42] and to machine learning

models in [43]. In [40], the extended Kalman filtering (EKF), unscented Kalman filtering (UKF) and particle filtering techniques are applied and compared for experimental Li-S SOC estimation. In [41], an adaptive neuro-fuzzy inference systems algorithm is developed to estimate SOC based on real-time ECM parameterization. In [42], a dual Kalman filtering technique is used for combined Li-S state and parameter estimation. Finally, in [43], a Long Short-Term Memory Recurrent Neural Network model is built and calibrated for online Li-S state estimation.

The above literature, while encouraging, does not address the problem of estimating the masses of the various species participating in Li-S battery redox reactions. This is an important problem because unlike traditional lithium-ion batteries, where lithium intercalates into and out of the cathode/anode materials, the Li-S chemistry involves multiple reduction reactions that convert S_8 gradually to S^{2-} during discharge. This makes the definition of SOC in Li-S batteries a little ambiguous, in the sense that one can potentially define multiple "states of charge" associated with different reacting species. One possible solution to this problem is: instead of estimating a single overall SOC, one can estimate internal state variables such as the active masses of dissolved sulfur species using a physics-based model. Such state estimation provides a more detailed picture of the internal states of the battery. This, in turn, is potentially useful for predicting and managing phenomena such as the dependence of the Li-S discharge capacity on applied current [1]. This dissertation introduces the online estimation of species masses in a Li-S battery based on the experimentally parameterized zero-dimensional physics-based model. Observability analysis reveals poor observability in the low plateau region, where cell

voltage curve is flat. A reduced-order model is derived through mass conservation can improve the estimation accuracy, given a known total active sulfur mass.

When a lumped SOC is defined in equivalent circuit models, poor SOC observability is also present in the low plateau region. Another way to improves the best theoretically-achievable battery SOC estimation accuracy is to apply a periodic discharge current profile, thereby estimating internal battery resistance and exploiting its dependence on SOC for better SOC estimation. This dissertation proposes and validates this idea through both theoretical analysis and a simulation study on an experimentally-parameterized equivalent circuit model.

1.3.3 Optimal Control for Li-S Batteries

The open circuit voltage and the internal resistance are two of the key elements needed to predict battery performance. Many factors affect the characteristics of the OCV/R_0 curves of Li-S batteries significantly (where R_0 is equivalent series resistance). State of charge and temperature are two of the most important factors [44].

Fig. 1.1(b) indicates that open circuit voltage and internal resistance are sensitive to state of charge. Experiments show that the electrolyte conductivity of Li–S batteries depends on the concentrations of both lithium salt and polysulfides [45, 46]. At high concentrations, increased ionic interactions reduce electrolyte conductivity. During the high plateau region, dissolved polysulfide concentration accumulates to the maximum point, increasing viscosity and causing electrolyte resistance to grow

[19]. Precipitation then decreases electrolyte viscosity, reducing internal resistance. The rebound of the R_0 curve during the second half of the low plateau can be potentially explained by the fact that the precipitate covers the interfacial area, blocking the active reactants.

The internal resistance and the open circuit voltage of a Li-S battery demonstrate strong sensitivity to temperature, shown by experimental measurements [37, 47]. The temperature term shows up directly in the well-known Nernst equation and Butler-Volmer equation, influencing the open circuit voltage. At the same time, diffusion and reaction rates are positively related with temperature, as increased internal energies of the ions speed the movements and reactions. A colder temperature induces higher internal resistance due to slower ion charge transfer in the electrolyte.

The variation in internal resistance and OCV can be both a challenge and an opportunity. It increases the difficulty in characterizing the model, but it also provides a potential to optimize the performance of Li-S batteries. Optimal control tools have already been used to improve the overall energy densities of lithium-ion batteries [48, 49]. However, the lessons learned from this previous literature may not be directly translatable to the Li-S chemistry due to fundamental differences in the underlying reactions and dynamics. The problem of optimizing the input trajectories of Li-S batteries therefore warrants independent investigation: a topic that, to the the best of the author's knowledge, remains unexplored in the literature. In this work, the author utilizes a coupled thermal/electrical equivalent circuit model, based on the existing literature, that captures the dependence of battery resistance on both

temperature and SOC, and constructs an optimal discharge strategy that maximizes total energy release over a fixed time horizon.

1.4 Contributions

The practical use of Li-S batteries can potentially benefit from control-oriented research. The overarching goal of this dissertation is to parameterize models and construct estimation/control algorithms that can be implemented into the battery management system for Li-S batteries. This is a timely topic, particularly because the Li-S battery industry is mainly in the pilot-scale production stage in many companies and universities, and there are few or no commercial Li-S batteries on the market. To obtain necessary experimental data, this work includes a prototype cell fabrication part as the bedrock, presented in Chapter 2. The rest of the dissertation presents 4 main contributions to the literature.

Contribution #1: Chapter 3 explores the problem of parameterizing a zero-dimensional physics-based Li-S model. Due to the dependency between the parameters, a simulation-based sensitivity study is performed to provide guidance on the choice of to-be-identified parameters. These parameters are identified by fitting the simulated voltage profile to the experimental data for four models considering different reaction chains. The best fitted model is suggested for the following state estimation study.

Contribution #2: Chapter 4 examines the problem of estimating the internal states of the zero-dimensional model, which is parameterized with the suggested

reaction chain in Chapter 3. This contribution shows the possibility to construct an algorithm for estimating the masses of various species in Li-S batteries, providing a more detailed picture of the internal states of the battery compared to a more traditional "lumped" SOC estimate. This chapter reformulates the model from a set of differential algebraic equations (DAEs) to a set of ordinary differential equations (ODEs). This is followed by an observability analysis using the empirical observability gramian. This chapter presents and discusses the simulation results of an unscented Kalman filter (UKF)-based state estimation for both the full-order ODE model and a reduced-order ODE model.

Contribution #3: Chapter 5 demonstrates the fundamental insight that battery SOC estimation accuracy can benefit from the dependence of battery resistance on SOC. Fisher information is used for developing this fundamental insight, based on a first-order equivalent circuit battery model. Moreover, experimental data from laboratory prototype coin cells are used to parameterize the equivalent circuit model, and the model is utilized in a Monte Carlo simulation study to support this theoretical insight. The simulation study shows a 50% improvement in SOC estimation accuracy in the low plateau region, where the slope of open-circuit battery voltage with respect to SOC is particularly shallow.

Contribution #4: Chapter 6 examines the problem of optimizing the discharge trajectory of a Li-S battery to maximize its energy release over a fixed time horizon. This optimization study utilizes a coupled thermal/electrical equivalent circuit model, based on the existing literature, that captures the dependence of battery resistance on both temperature and state of charge. The optimization problem

is solved using direct collocation. Simulation results show that trajectory optimization improves total energy delivery over a 2-hour time window compared to both constant-current and constant-power discharge.

The remainder of this dissertation highlights these above contributions in model-based estimation and control for Li-S batteries, and Chapter 7 concludes the dissertation with a brief summary of the completed work.

Chapter 2: Lithium-Sulfur Coin Cell Fabrication

The processes and materials used for cell fabrication play an important role in the electrochemical performance of Li-S batteries. A significant portion of the research presented in this dissertation relies on the experimental cycling of 2016-type laboratory Li-S coin cells. This chapter introduces the process used for fabricating these cells. This process is based on the recipe in [50]. Cycling the prototype cells fabricated using this recipe provides the experimental data serving as as the bedrock to support the further control-oriented research in the following chapters.

2.1 Cathode Materials and Preparation

The cathode material consists of 56 wt% sulfur powder (S, 99.5% purity, Sigma-Aldrich), 24 wt% ketjenblack (EC-600JD powder, Nouryon), 10 wt% carbon nanofiber (PR-24-XT-LHT, Pyrograf Products Inc.) as conductive materials, and 10 wt% polyvinylidene fluoride (PVDF, Sigma-Aldrich) dissolved in NMP (Sigma-Aldrich) as a binder. The main objective of the cathode fabrication is to obtain a homogeneous electrode layer of sulfur carbon composite, while PVDF creates bindings between the particles and with the cathode collector. The sulfur power has an initial average particle size of 40 μm and an orthorhombic crystal structure [51].

Ketjenblack and carbon nanofiber are selected as conductive materials for their high specific surface area, low particle size, and high electrical conductivity to improve the electron transfer between sulfur and collector. Moreover, carbon nanofiber helps to create a conductive, high porosity network allowing reactions to happen at the electrode-electrolyte interface. PVDF is chosen as the binder for its electrochemical, thermal, chemical stability, and its high adherence. Carbon coated aluminum foil of 18 μm thickness is used as the cathode collector. The highly conductive carbon coating improves the adherence of the cathode layer with the current collector and reduces the contact resistance [51]. The cathode fabrication process is performed outside of the glovebox. The cut-out cathodes can be stored in the glovebox until used. The steps needed to fabricate the cathode chips of 2016-type coin cells are listed as follows.

Step 1: Dissolve PVDF into the NMP solvent. The weight ratio of PVDF and NMP is 5:95. Use the magnetic stir bar to stir at least 4 hours until all the solid is dissolved. The PVDF-NMP solution will maintain its best performance for a week.

Step 2: Hand mill 30 wt% ketjenblack and 70 wt% sulfur power until no yellow particles can be visually seen. Heat the mixed power in a vacuum oven at 160 °C for at least 8 hours, preferably in a sealed glass flask.

Step 3: Ball mill or hand mill the C/S composite (from Step 2) with carbon nanofiber. The weight ratio of C/S composite and carbon nanofiber is 8:1. After this step, the cathode active and conductive materials are pre-

pared.

Step 4: Make the slurry. The weight ratio of C/S, nanofiber and PVDF should be 8:1:1. Since the solution made in Step 1 is 5 wt%, the weight ratio of the solid mixture and liquid solution is 9:20. Based on trials involving different solid content percentages (solid weight/(solid+liquid weight)), 10% is a preferred number for a uniform coating. To achieve this content, add more NMP until the solid content reaches 10%. Use a magnetic stirrer to mix the slurry for at least 24 hours to get a shiny, slightly flowing slurry.

Step 5: Spray the surface of a laboratory coating machine with ethanol to help the carbon coated aluminum foil adhere to the machine. Adjust the applicator to 200 to 250 μm. Coat the slurry uniformly. Dry the coated foil under room temperature until no liquid can be seen, then further dry it in the oven at 60 °C for 12 hours.

Step 6: Cut the cathode foil into chips using the disc cutter, and calculate the sulfur loading of the single chip. The loading can be calculated through the following equation. Then, put one cathode chip and one separator chip into a plastic bag, and mark the sulfur loading on the plastic bag. The cathode is ready to be moved into the glovebox for assembling.

$$m_{sulfur} = (m_{cathode\ chip} - \frac{1}{10} \times 10\ m_{aluminum\ discs}) \times 80\% \times 70\%. \quad (2.1)$$

2.2 Anode and Separator Materials

For the anode, plain lithium foil with 16mm diameter x 0.6mm thickness is used (MTI). The lithium foil is stored inside the glovebox to ensure a low oxygen and water vapor environment. The separator is composed of a single porous polypropylene membrane (type 2400, Celgard). The separator should be bigger than the electrode for full separation. Hence, the membrane is cut into 19 mm diameter chips using a disc cutter. While other types of separators are commercially available for lithium batteries [52], the material chosen for this work is known to work well from previous studies [50, 53]. Also, assuming it can be wetted properly, the choice of separator does not affect the performance of the cell significantly, at least for low to medium discharge/charge rates [54].

2.3 Electrolyte Materials and Mixing

Electrolytes are prepared inside the glovebox. The electrolyte used is 1M lithium bis(trifluoromethylsulfonyl)imide (LiTFSI, Gotion) and 0.2M lithium nitrate ($LiNO_3$) (99.99%, Sigma-Aldrich) in the dioxolane/dimethoxylethane (DOL/DME, Gotion) mixture (DOL/DME = 1:1, v/v). This recipe is for 1L. Here, the author calculates the weight of each material for making 10ml electrolyte. The weight information is listed in Table 2.1. All ingredients are added to a glass flask and stirred with a magnetic stir bar at least 24 hours until the salt is entirely dissolved.

Material	LiTFSI	$LiNO_3$	DOL	DME
Volume/mol	0.01 mol	0.002 mol	5 ml	5 ml
Density	287.075 g/mol	68.946 g/mol	1.06 g/ml	0.867 g/ml
Weight	2.87 g	0.1379 g	5.3 g	4.335 g

Table 2.1: Recipe for the electrolyte of Li-S coin cells

2.4 Cell Assembly

The assembly process happens in a Argon-filled glovebox. The stainless steel cell casing parts are dried overnight at 140 °C under vacuum before use to avoid contamination of the electrolyte by residual water. The electrolyte is added to the cell in two drops: put the cathode on the bottom, then the first drop is applied on top of the cathode before adding the separator, the second drop on top of the separator before adding the anode. The separator is larger than both the anode and cathode to prevent short circuits. The amount of electrolyte is slightly more than is needed to fully soak the separator. There is a surplus of liquid electrolyte which causes an adhesive force between the separator and the stainless steel casing around the electrodes and also serves as a reservoir, in case some electrolyte is decomposed or spilled. Cells are assembled using a hydraulic crimper to press all the components to about 1000 psi.

Chapter 3: Parameter Identification for Zero-dimensional Li-S Battery Models

3.1 Overview

The literature presents ongoing efforts to improve the electrochemical performance of Li-S batteries [55]. This chapter is part of a complementary effort to improve Li-S battery performance through modeling, focusing specifically on the problem of parameterizing Li-S battery models from experimental data. This is a critical first step towards model-based estimation and control studies in subsequent chapters[1].

A number of Li-S battery models can be used for parameter estimation and model-based control. These models fall on a spectrum of fidelity and complexity levels. Equivalent circuit models (ECMs) of Li-S batteries sit at one end of this spectrum. They typically combine empirical open-circuit voltage maps with (often charge- and temperature-dependent) resistor-capacitor circuits [34, 35, 36, 37]. Typical uses of such simple models include online state of charge estimation [41, 42, 57]. At the other end of the spectrum, one finds physics-based models of the reduction-

[1]The materials presented in this chapter appear in archival publication in the ASME Letters on Dynamic Systems and Control[56]

oxidation, diffusion, precipitation, and self-discharge dynamics in Li-S batteries. These are typically partial differential algebraic equation (PDAE) models of coupled diffusion-reaction dynamics [12, 13, 14, 15, 16, 17]. They have the advantage of providing higher-fidelity representations of the underlying battery physics, at the expense of high complexity. Zero-dimensional (0D) models provide an important middle ground between these two modeling extremes[2]. They neglect the diffusion of species inside Li-S batteries, but use the laws of electrochemistry to model the underlying battery reactions. As a result, the zero-dimensional models perform better at low C-rates with thin electrodes. This approach results in lower-order models with fewer parameters to identify and reduced computational complexity. Simplified two-reaction and multi-reaction 0D models introduced in [18] and [19] are able to capture the main features of battery voltage response during discharge. The computational complexity of a 0D Li-S battery model depends on the specific choice of which reactions to model, and which to ignore. One potential approach for making this choice is to compare the fidelity with which different 0D models can fit a given experimental data set. Such an exercise is appealing because it can furnish both: (i) a systematic comparison between different battery models using the same data set, and (ii) an experimental parameterization of different 0D Li-S battery models. To the best of the author's knowledge, both of these contributions remain relatively unexplored in the literature. The overarching goal of this chapter is to address this research gap.

[2]The term "zero-dimensional", in this context, comes from the electrochemical battery modeling literature, and refers to the elimination of diffusion-driven spatial concentration gradients from the underlying equations representing battery behavior.

Starting from previous work on 0D Li-S models in the literature, this chapter goes one step further to analyze different 0D models capturing different underlying redox reactions. The goal is to answer the following questions: (i) How does each reaction influence the discharge voltage curve in a 0D model? (ii) Do all the model parameters have a significant impact on the discharge voltage curve? Is it necessary to identify them all? (iii) How accurately can the identified models fit the experimental voltage behavior? Is there a model with a specific reaction chain that performs best? The ultimate goal is to provide guidance on the choice of which reactions to model for future applications, such as state of charge estimation (discussed in Chapter 4).

The remainder of this chapter addresses these questions, and is organized as follows. Firstly, this work describes the 0D model structure adopted from [18, 19], combined with the reduction reactions considered in each model. Secondly, the author provides a simulation study illustrating the effects of different reactions on the discharge voltage performance. Then, a parameter sensitivity study is performed to provide guidance on which parameters are critical to identify from experimental data. Finally, the parameter identification results are presented by fitting the experimental data. The conclusions summarized in this chapter are based on an experimental study at a discharge rate of 0.3C. At this discharge rate, the discharge voltage curve of an Li-S battery exhibits three main features, namely: a high plateau, a low plateau, and a dip point separating these two plateaus. Figure 1 shows two discharge characteristic curves, obtained by cycling Li-S cells fabricated as part of this study at 0.25C and 0.125C. Both of these curves exhibit the three

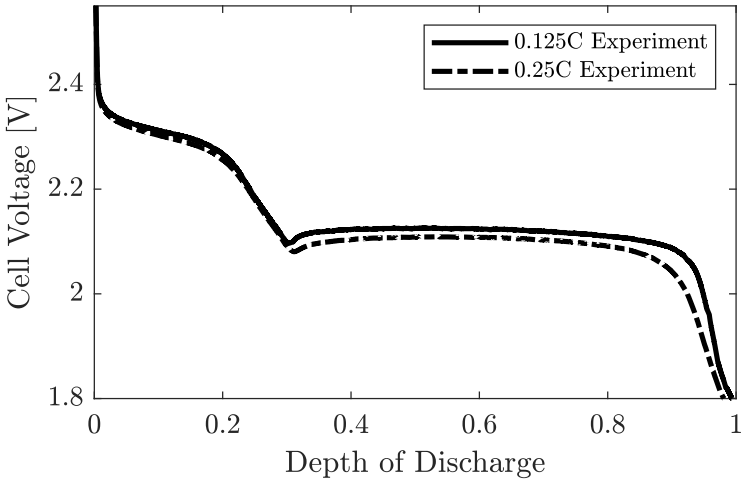

Figure 3.1: Experimental cell voltage profiles under different discharge currents

main features discussed above, namely: the high plateau, low plateau, and dip point. Moreover, the small differences in discharge voltage between these curves can be partially attributed to simple polarization effects, such as Ohmic polarization. Thus, the chapter's focus on a discharge C-rate of 0.3C can help shed light on behaviors observed over a range of C-rates, especially C-rates below 0.3C.

3.2 Zero-dimensional Physics-based Model

This section describes the 0D reaction models used for subsequent analysis. The models build on two existing bodies of work. First, research by Zhang *et al.* [19] develops a lumped model describing the dynamics of dissolved species concentrations and cathode material porosity in Li-S batteries. Moreover, this model includes the full reduction reaction chain and the effective electrolyte resistance. Second, research by Marinescu *et al.* [18] introduces another 0D model taking into account the dynamic evolution of different species' masses as well as the shuttle effect. This model simplifies the chain of sulfur reduction reactions into two steps. The work in this

Models	Model #1	Model #2	Model #3	Model #4
Reduction Reactions	$\frac{1}{4}S_8 + e^- \rightleftharpoons \frac{1}{2}S_4^{2-}$ $\frac{1}{6}S_4^{2-} + e^- \rightleftharpoons \frac{2}{3}S^{2-}$	$\frac{3}{8}S_8 + e^- \rightleftharpoons \frac{1}{2}S_6^{2-}$ $S_6^{2-} + e^- \rightleftharpoons \frac{3}{2}S_4^{2-}$ $\frac{1}{6}S_4^{2-} + e^- \rightleftharpoons \frac{2}{3}S^{2-}$	$\frac{1}{2}S_8 + e^- \rightleftharpoons \frac{1}{2}S_8^{2-}$ $\frac{3}{2}S_8^{2-} + e^- \rightleftharpoons 2S_6^{2-}$ $S_6^{2-} + e^- \rightleftharpoons \frac{3}{2}S_4^{2-}$ $\frac{1}{6}S_4^{2-} + e^- \rightleftharpoons \frac{2}{3}S^{2-}$	$\frac{1}{2}S_8 + e^- \rightleftharpoons \frac{1}{2}S_8^{2-}$ $\frac{3}{2}S_8^{2-} + e^- \rightleftharpoons 2S_6^{2-}$ $S_6^{2-} + e^- \rightleftharpoons \frac{3}{2}S_4^{2-}$ $\frac{1}{2}S_4^{2-} + e^- \rightleftharpoons S_2^{2-}$ $\frac{1}{2}S_2^{2-} + e^- \rightleftharpoons S^{2-}$
Dissolved Sulfur Species	$S_8,\ S_4^{2-}, S^{2-}$	$S_8,\ S_6^{2-},$ S_4^{2-}, S^{2-}	$S_8,\ S_8^{2-}, S_6^{2-},$ S_4^{2-}, S^{2-}	$S_8,\ S_8^{2-}, S_6^{2-},$ $S_4^{2-}, S_2^{2-}, S^{2-}$

Table 3.1: Reduction reactions considered in the models

dissertation combines the underlying structures of these two models, and expands them to capture the dynamics of different sets of reduction reactions. The end result is a set of four 0D models ranging from low to high complexity. The simplest model covers a minimum set of reduction reactions modeled in the literature, whereas the most complex model covers the full set of sulfur reduction reactions in Li-S batteries. The reactions considered in each model are listed in Table 3.1. In this work, the author adopts the following modeling assumptions from the literature: (i) there is an unlimited amount of lithium supply in the cell with a negligible overpotential on the anode side, as in [13]; (ii) the shuttle effect of polysulfides is not included due to this chapter's focus on the voltage performance instead of capacity fade [19]; and (iii) only the lowest polysulfide's precipitation reaction ($2Li^+ + S^{2-} \rightleftharpoons Li_2S \downarrow$) is modeled [18, 19].

Since the model is zero-dimensional, there exists no mass transport due to diffusion/migration. The only dynamics changing the masses of the dissolved species are the electrochemical reaction and precipitation. These dynamics lead to the time-evolution relations for the masses of various sulfur species and the porosity

of the cathode material, which act as the state variables in the model. Below is the resulting differential algebraic equation (DAE) model (assuming discharge), including both state equations and algebraic constraints.

State Equations:

$$\dot{m}_i = \sum_j \frac{n_{S_i} M_s}{n_j F} s_{i,j} i_j \ , \quad \text{for } i = 1, ..., q-1 \tag{3.1}$$

$$\dot{m}_q = \frac{n_{S_q} M_s}{n_p F} s_{q,p} i_p - \dot{m}_{S_p} \tag{3.2}$$

$$\dot{m}_{S_p} = k_p m_{S_p} (m_q - S_{sat}) \tag{3.3}$$

$$\dot{\alpha} = -\omega \dot{m}_{S_p} \tag{3.4}$$

Constraints:

$$E_j = E_j^0 - \frac{RT}{n_j F} \sum_i s_{i,j} \ln(\frac{m_i}{n_{S_i} M_s v}) \tag{3.5}$$

$$i_j = -a_v i_j^0 \{ \prod_i (\frac{m_i}{m_i^0})^{p_{i,j}} e^{\frac{F}{2RT}\eta_j} - \prod_i (\frac{m_i}{m_i^0})^{q_{i,j}} e^{-\frac{F}{2RT}\eta_j} \} \tag{3.6}$$

$$a_v = a_v^0 \alpha^\gamma \tag{3.7}$$

$$I = \sum_j i_j \tag{3.8}$$

$$V = \eta_j + E_j \tag{3.9}$$

The input of the system is current I, and the output of the system is the voltage measurement across the battery V. The state variables include: the masses of the dissolved sulfide species m_i, where i is the species index, the mass of the

precipitated sulfur m_{S_p}, and the relative porosity of the cathode material α.

The rates of mass change for higher-order dissolved sulfide species are governed by Eqn. 3.1. For species S^{2-}, one needs to consider its mass generation from the last reduction reaction and its mass loss due to precipitation, as shown in Eqn. 3.2. The parameters k_p and S_{sat} are the precipitation rate constant and the saturation mass of S^{2-}. The nucleation and growth phenomenon is described by Eqn. 3.3 [18]. The rate of change of precipitate mass is partly driven by the precipitate mass itself, with a rate constant ω. This reflects the fact that the existing precipitate serves as a nucleus for further precipitation/growth, as long as the mass in the electrolyte is above a given saturation mass. The parameters n_{S_i}, n_j, R, T, v, M_s, F and $s_{i,j}$ represent the number of sulfur atoms in species i, number of electrons exchanged in reaction j, gas constant, temperature, cell volume, molar mass of a sulfur atom, Faraday's constant, and stoichiometric coefficients of the reactions, respectively. The coefficients $p_{i,j}$ and $q_{i,j}$ represent the positive and negative elements of $s_{i,j}$.

Relative porosity α is one of the state variables in the model with the dynamics governed by Eqn. 3.4. This variable equals the current porosity of the cathode material divided by initial porosity, and has a direct effect on the active reaction area a_v, as shown in Eqn. 3.7 [12]. When the porosity decreases to zero, all the reactants are blocked by the precipitate from the cathode material surface. This can be one of the indicators of the cell's full discharge, another full discharge scenario being the reduction of all polysulfides to S^{2-}. As the cell approaches complete coverage of the cathode ($\alpha \to 0$), larger overpotentials (η_j) are needed for the same current. This provides one explanation of the low measured voltage at the end of

Li-S battery discharge.

The reduction potential of each reaction E_j is given by the Nerst equation (Eqn. 3.5), assuming that E_j^0 is the equilibrium potential when the concentration of the dissolved species in reaction j is 1 mol/L [19]. The current generated by the corresponding reduction reaction is described by the Butler–Volmer equation (Eqn. 3.6), where η_j is the overpotential, i_j^0 is the exchange current density, γ is a morphology parameter serving as the power of the relative porosity and m_i^0 is the initial mass of species i. All these currents sum to the only input variable, namely, the external discharge current I, as shown in Eqn. 3.8. Finally, Eqn. 3.9 states the relation between the voltage measured across the battery V, the overpotential η_j and the reduction potential E_j of each reaction.

3.3 Voltage Responses for Different Reaction Chains

In the literature, there exist at least two simplifications of the reaction chain on the cathode side, namely, the two-step reduction $S_8 \rightarrow S_4^{2-} \rightarrow S^{2-}$ [27] and the four-step reduction $S_8 \rightarrow S_8^{2-} \rightarrow S_6^{2-} \rightarrow S_4^{2-} \rightarrow S^{2-}$ [15]. Different Li-S battery models, capturing different representations of the overall reaction chain, are built to suit the focus areas of the corresponding research studies. In this section, the author compares the simulated voltage outputs of the models in Table 3.1 under a 0.3C discharge, and analyzes each reaction's influence on the different features of the discharge voltage curve. OpenModelica [58] is used to build and simulate the models with the key parameter values listed in Table 3.2. The simulated discharge

Model	Notations	Values	Units
Model #1	E_j^0 *	2.40, 2.10	V
	i_j^0 **	2.00, 0.02	A/m^2
Model #2	E_j^0 *	2.40, 2.30, 2.10	V
	i_j^0 **	2.00, 0.02, 0.02	A/m^2
Model #3	E_j^0 *	2.46, 2.38, 2.30, 2.10	V
	i_j^0 **	2.00, 0.02, 0.02, 0.02	A/m^2
Model #4	E_j^0 *	2.46, 2.38, 2.30, 2.15, 1.98	V
	i_j^0 **	2.00, 0.02, 0.02, 0.02, 0.02	A/m^2
All Models	v *	0.0114	L
	S_{sat} *	0.0001	g
	a_v^0 *	1	m^2
	γ *	1.5	-
	ω **	0.1	$1/g$
	k_p *	22	$1/(gs)$
	R	8.3145	$J/(Kmol)$
	F	9.649×10^4	C/mol
	T	298	K

* adopted from [18, 19], ** estimated parameters.

Table 3.2: Nominal parameter values in the simulations

voltage-capacity curves are compared in Fig. 3.2.

The main observations from simulation results are as follows. First, all the reaction models provide similar specific capacity values, approximately 1675 mAh/g, matching the theoretical specific capacity value in [55]. Second, the intermediate reactions associated with the high plateau can influence this plateau's shape and duration. Specifically, when the high plateau reaction is simplified to only $S_8 \rightarrow S_4^{2-}$ in Model #1, the voltage curve shows a relatively longer duration for this plateau. Moreover, this high plateau ends with a dramatic, almost vertical voltage drop. The same observation is presented in [14]. This drop can be explained by the potential dynamics given by Eqn. 3.10. At the end of the reaction, the mass of the reactant

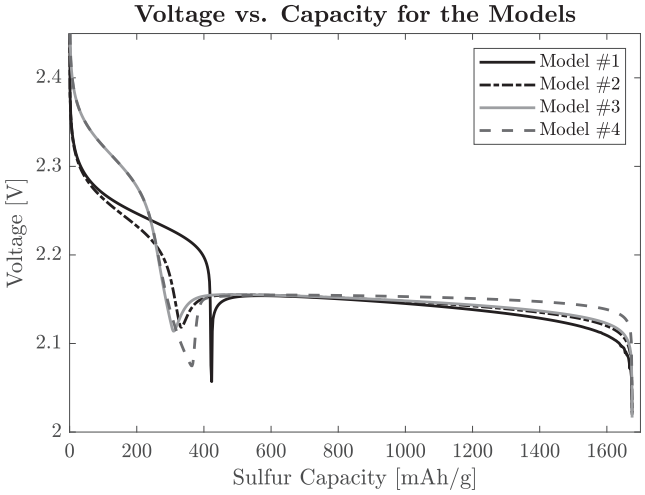

Figure 3.2: Discharge voltages vs. sulfur capacity for the reaction models

approaches zero, while the rate of change of this mass maintains a relatively stable value due to the fact that i_j still needs to meet the external discharge current value. This results in $\dot{E}_j \to -\infty$. Hence, the measured voltage V exhibits an almost vertical drop. When intermediate reactions are added between S_8 and S_4^{2-}, a milder slope emerges with the dip between the plateaus occurring at higher voltages.

$$\dot{E}_j = -\frac{RTM_s v}{n_j F} \sum_i s_{i,j} n_{S_i} \frac{\dot{m}_i}{m_i} \tag{3.10}$$

This analysis provides the characteristics of the voltage curve considering different reactions. The bottom line is that simplified representations of the reduction reactions are reasonable in terms of one's ability to capture theoretical specific capacity, but the influence of different simplifications on the voltage features is significant. One needs to choose the reactions carefully based on the purpose of the given application. For example, studies focusing on capacity fade may choose simpler models, while state of charge estimation may require more complicated reaction models due

to the accuracy required to capture the characteristics of output voltage.

3.4 Parameter Sensitivity Analysis

One can broadly categorize the parameters of the above models into two groups. The first group includes parameters that are known *a priori*, such as Faraday's constant, gas constant, temperature, molar mass, number of electrons transferred in each reaction, etc. The second group contains unknowns such as standard potentials, exchange current densities, initial masses of the dissolved species, and precipitation-relevant parameters (i.e., the morphology parameters γ, ω, and precipitation rate). Increasing the number of reactions and species considered in the model increases the number of unknown parameters. Hence, the difficulty of parameterization increases. Here, the author analyzes the sensitivity of the 0D model's output to the underlying parameters in order to better understand which parameters are critical to identify.

Instead of using a theoretical parameter sensitivity approach [59], this work applies a similar analysis method to the work presented in [30, 31, 32] for a 1D Li-S battery model. Specifically, the author chooses one parameter at a time and investigates the voltage performance changes due to variations in only this parameter. All other parameters are held constant. This parameter sensitivity analysis is performed on all models listed in Table 3.1. Since Model #4 describes the full reaction chain containing the largest number of parameters (total number of 14), the results of Model #4 are chosen for the following sensitivity discussions. Cell

voltage sensitivities to different parameters are plotted for two perturbations from the nominal values.

3.4.1 Sensitivity to Standard Potential E_j^0

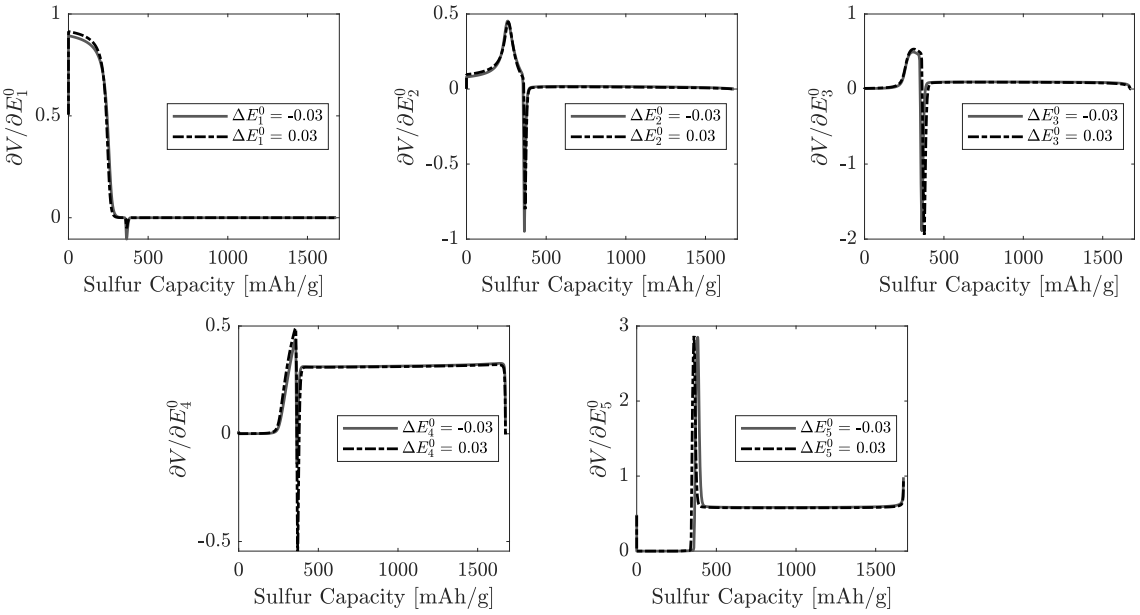

Figure 3.3: Cell voltage changes with respect to the deviations of nominal standard potential E_j^0 for Model #4

Fig. 3.3 presents the results of analyzing the cell voltage sensitivity of Model #4 to parameter E_j^0. One can see the relative dominance of different reactions by observing the corresponding changes in the voltage curve. Reaction $S_8 \rightarrow S_8^{2-}$ ($j = 1$) has a dominant influence on the high plateau voltage level. Reaction $S_8^{2-} \rightarrow S_4^{2-}$ ($j = 2, 3$) has a strong effect on the "ending slope" of the high plateau and the dip point between the two plateaus, while slightly changing the low plateau voltage level. The last two reactions ($j = 4, 5$) occur during the low plateau region, and therefore both of the corresponding standard potentials influence the voltage curve dramatically.

3.4.2 Sensitivity to Exchange Current Density i_j^0

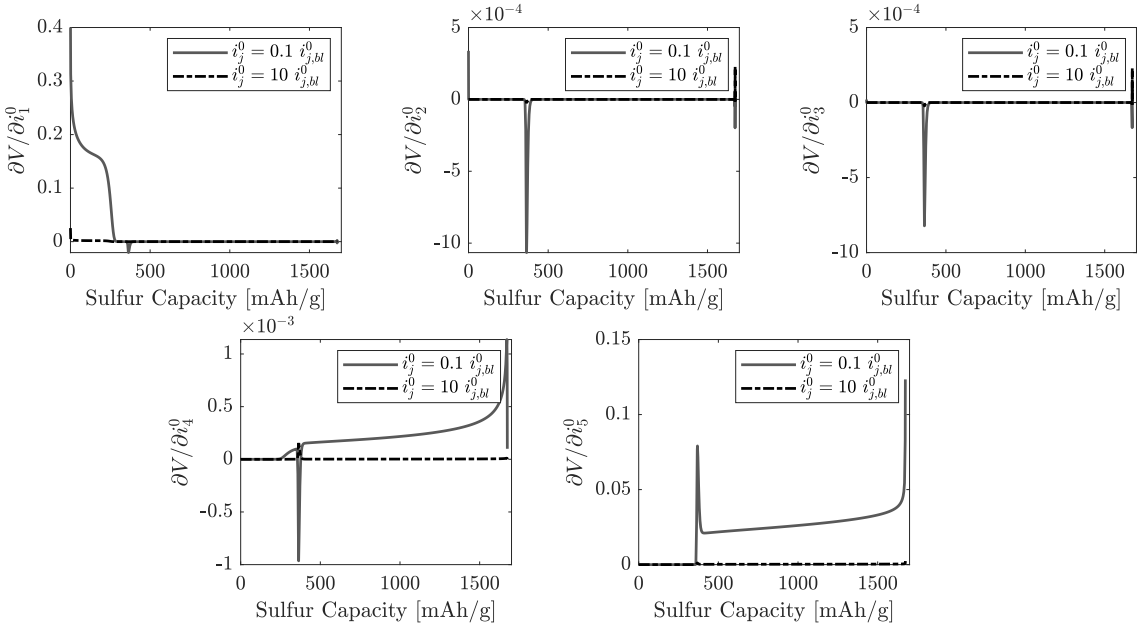

Figure 3.4: Cell voltage changes with respect to the deviations of nominal exchange current density i_j^0 for Model #4

The sensitivity analysis for i_j^0 is shown in Fig. 3.4. One can observe minor changes in the voltage curve within the chosen range of i_j^0. The exchange current densities of the middle reactions have negligible impacts on voltage, as the voltage curves show a negligible difference. Compared to E_j^0, which influences the voltage V through the variable E_j, the parameter i_j^0 affects the overpotential η_j though an exponential function. On the one hand, this shows that E_j^0 and i_j^0 have similar effects on voltage, and highlights the challenge of identifying both i_j^0 and E_j^0 simultaneously from experimental data. On the other hand, bigger variations in i_j^0 produce smaller changes in the voltage curve compared to E_j^0, which suggests the exchange current density has less of an impact on the model's voltage performance.

3.4.3 Sensitivity to Precipitation-related Parameters

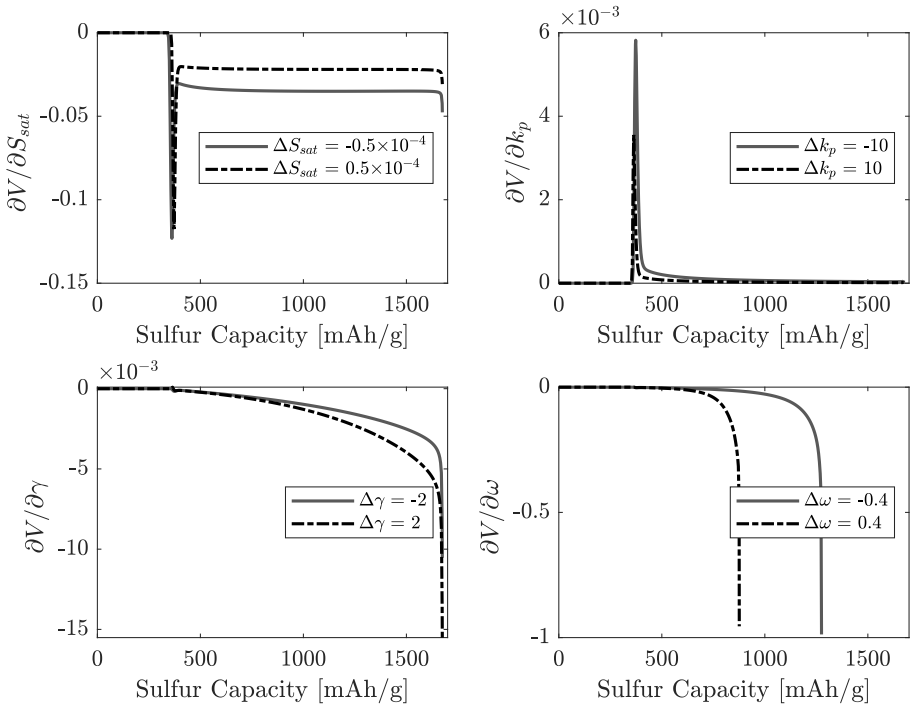

Figure 3.5: Cell voltage changes with respect to the deviations of nominal precipitation relevant parameters for Model #4

Four parameters essentially govern the precipitation phenomenon, namely, the saturation mass of dissolved S^{2-}, the precipitation rate k_p, and the morphology parameters of the relative porosity of the cathode, γ and ω. The variations of each parameter produce changes in the low plateau region without influencing high plateau voltages, as shown in Fig. 3.5. When the saturation mass increases, more S^{2-} is dissolved in the electrolyte, reducing the potential of the reaction $S_x^{2-} \rightarrow S^{2-}$, hence providing a lower cell voltage. The precipitation rate k_p and morphology parameter γ determine the flatness of both the beginning and end regions of the low plateau. Larger values of k_p and smaller values of γ provide a flatter low plateau. The parameter ω is the only parameter dramatically affecting the capacity of S_8.

With an increase in the rate of change of relative porosity, the discharge process can terminate earlier because of the resulting paucity of active reaction area inside the cathode material.

3.4.4 Sensitivity to Initial Mass of Dissolved S_8

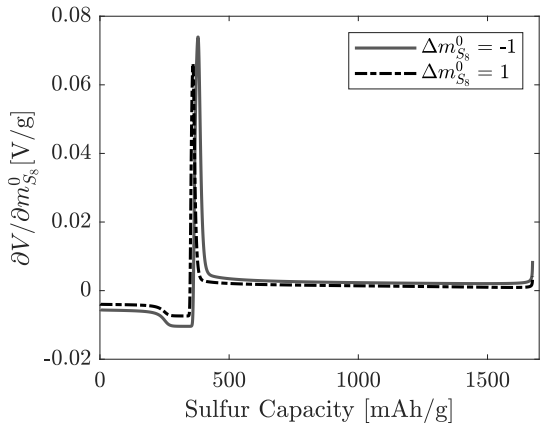

Figure 3.6: Cell voltage changes with respect to the deviations of nominal initial mass of dissolved S_8 for Model #4

This work assumes that all the active sulfur is dissolved into the electrolyte at the beginning of discharge. The mass of the dissolved S_8 is the main factor determining the total amount of active material inside the battery, and the initial masses of other species at the beginning of discharge are comparatively very small. In this case, sensitivity analysis is only performed with respect to the initial mass of dissolved S_8. The results are presented in Fig. 3.6 with negligible impacts on the voltage curve and specific capacity. However, one must note that the voltage curve difference emerges when plotting the voltage with respect to time instead of specific sulfur capacity. Hence, the dip point between the two plateaus changes with respect to time.

From this analysis, the following conclusions are made to guide parameter identification: (i) Although both E_j^0 and i_j^0 affect the voltage curve, V is more sensitive to E_j^0. (ii) In the set of parameters relevant to precipitation, correctly capturing the values ω and γ is more essential for capturing the shape of the low plateau. (iii) The initial mass of dissolved S_8 influences the timing of the dip point between the high and low plateaus. Hence, in the parameter identification study, the author focuses on parameters E_j^0, γ, ω, and $m_{S_8}^0$, with all the other parameters treated as known constants.

3.5 Parameter Identification Study

It is difficult to systematically compare multiple models of Li-S battery dynamics without fitting all of them to the underlying experimental data first. This section presents a parameterization study focusing on the proposed four reaction models. The author obtains the test data through discharging laboratory-made prototype coin cells.

3.5.1 Coin Cell Fabrication and Discharging Experiments

The author fabricated 2016-type coin cells following the procedures described in Chapter 2. The cathode material consisted of Carbon/Sulfur composite with 70 wt% sulfur, Ketjenblack EC60JD to form a conductive framework, and polyvinylidene fluoride (PVDF) dissolved in N-Methyl-2-pyrrolidone (NMP) as a binder. A lithium chip of 0.6 mm thickness served as the anode. The electrolyte used here

was 1M $LiTFSI$ and 4 wt% $LiNO_3$ in the dioxolane/dimethoxylethane mixture (DOL/DME = 1:1, V/V). The sulfur loading of the cell was calculated at 0.521 mg. A constant discharge current of 0.03 mA was applied in the experiment to obtain the discharge voltage curve. Testing was conducted at room temperature, using ARBIN battery test equipment with special attention given to the accuracy of current control. In particular, a separate capacitor charge/discharge test was used for estimating the bias in the cycler's current measurements, and this bias was used to correct measured data.

3.5.2 Scaling From Model to Prototype Using Similitude

One caveat appears when we implement the experimentally-measured Li-S cell current into the simulation model, namely, the need to scale the simulation model to match the physical sizing of the Li-S coin cell used in this study. Here we use the idea of similitude to scale the relative variables/parameters from the model to the prototype. For the fundamental dimensions in the model (i.e. time, mass, charge, length and temperature), charge is scaled by a given value μ, and we want to find the scaling factor for mass and length, with the other dimensions unchanged. Then the input current is scaled by μ due to the fact that time is not scaled. The relationship between the current inputs of the model and prototype is shown in Eqn. 3.11 and applies to i_j as well. The subscripts mod and pro represent model and prototype correspondingly.

$$I_{mod} = \mu \; I_{pro} \tag{3.11}$$

From Eqn. 3.1, we derive the scaling law for mass as shown below:

$$\frac{\dot{m}_{i,mod}}{\sum_j \frac{n_{S_i}}{n_j} s_{i,j}\ \dot{i}_{j,mod}} = \frac{\dot{m}_{i,pro}}{\sum_j \frac{n_{S_i}}{n_j} s_{i,j}\ \dot{i}_{j,pro}} \tag{3.12}$$

where other parameters are independent of mass and charge, except for $\dot{m}_i$ and i_j. Hence, we have

$$m_{mod} = \mu\ m_{pro} \tag{3.13}$$

Using the same logic, one can derive the scale factor for length as $\mu^{\frac{1}{3}}$ from Eqn. 3.6, and the scale factors for parameters a_v, v, i_j^0, ω, k_p are $\mu^{\frac{2}{3}}$, μ, $\mu^{\frac{1}{3}}$, $\frac{1}{\mu}$ and $\frac{1}{\mu}$. In the following parameterization simulation, the author uses 1A as the simulated model's input current with the corresponding μ being 3.33×10^4. This value of μ scales the simulation model down to match the true scale of the fabricated laboratory coin cell.

3.5.3 Optimization Problem Formulation

The parameter identification study uses the least-squares method based on the above 0D reaction models. The least-squares method estimates parameters by minimizing the squared discrepancies between observed data and the expected values. Given the models' highly nonlinear structure, the authors choose the particle swarm optimization algorithm [60] to solve the resulting nonlinear least-squares problem. The goal is to identify the parameter vector $\hat{\boldsymbol{\theta}}$ by solving the problem

below:

$$\min_{\hat{\boldsymbol{\theta}}} J = \sum_{k=1}^{N_{min}} (\hat{V}_k - V_{m,k})^2 + \alpha_w (\hat{T}_{end} - T_{end})^2 \tag{3.14}$$

$$where : \boldsymbol{\theta} = [\ E_j^0,\ \gamma,\ \omega,\ m_{S_8}^0\ ]^T, \quad N_{min} = min\{N, \hat{N}\} \tag{3.15}$$

subject to the dynamics of the system from Eqn. 3.1 to 3.9. In this problem formulation, $\hat{V}_k$ and $V_{m,k}$ represent the estimated and measured output voltages at time step k; $\hat{T}_{end}$ and T_{end} are the final times of the simulation and experiment; and the weight α_w reflects the importance of minimizing the difference between the simulated and experimental discharge durations.

3.5.4 Parameter Identification Results

The identification results are listed in Table 3.3, with the corresponding estimated voltages shown in Fig. 3.7. The identified parameters for all the models are able to fit the experimental data in terms of the total discharging time. The objective function values corresponding to the best estimated parameters for the models are shown in Fig. 3.8 (a). Interestingly, Model #3 performs the best fit with a minimum objective function value among all the models. The over-simplification of reactions in Model #1 leads to failure in capturing the slope of the voltage in the high plateau region. In contrast, the full reaction Model #4 does not provide a good fit in the middle region where the precipitation phenomenon emerges. This is potentially due to the simplification of the precipitation dynamics in the model. A

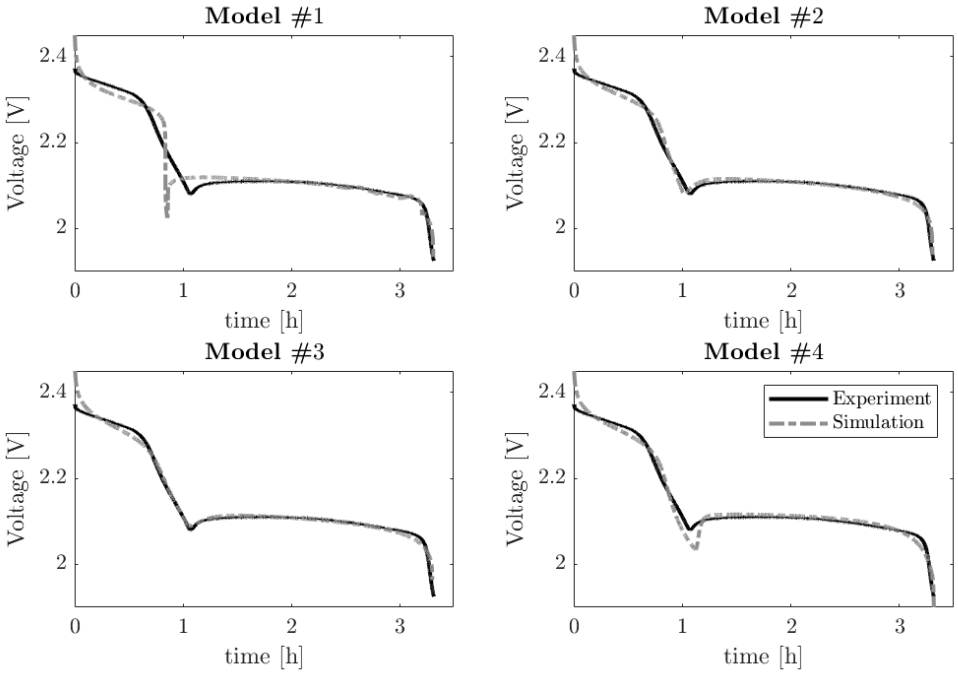

Figure 3.7: Discharge voltage comparison between experiment and simulation using identified parameters for all the models

more sophisticated physics-based precipitation model may improve the accuracy of the full reaction model.

Another observation pertains to the simulation time needed for one discharge cycle, as shown in Fig. 3.8 (b). Intuitively, the computational complexity of the models increases with the number of included reduction reactions. However, the execution time increases from Model #1 to Model #3 are minor, whereas the increase

Parameter	**Model #1**	**Model #2**	**Model #3**	**Model #4**	**Units**
E_j^0	2.453, 2.090	2.464, 2.360, 2.073	2.467, 2.374, 2.342, 2.069	2.467, 2.310, 2.208, 2.094, 1.972	V
γ	0.316	0.437	0.483	0.959	-
ω	0.508	0.570	0.613	0.650	$1/g$
$m^0_{S8,mod}$	2.001	2.628	3.038	3.523	g
$m^0_{S8,pro}$	0.060	0.079	0.091	0.106	mg

Table 3.3: Parameter identification results

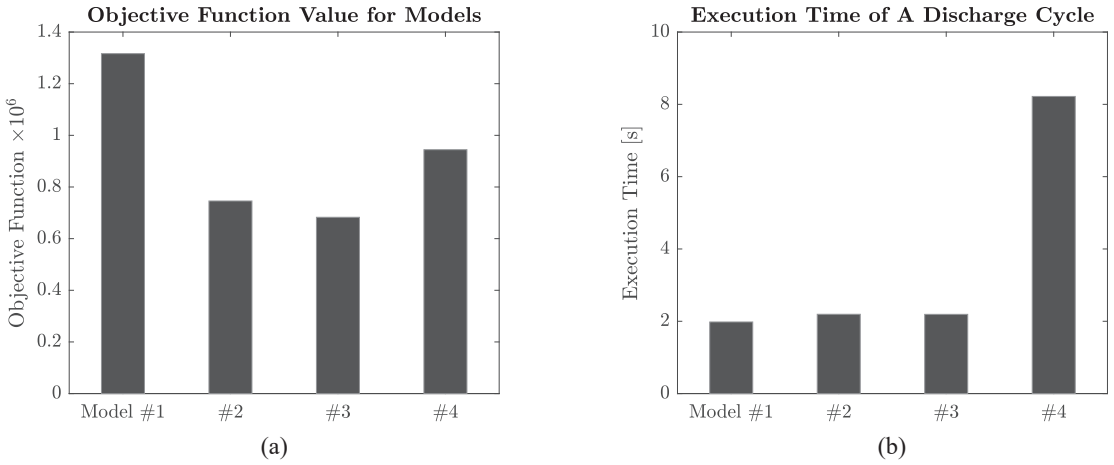

Figure 3.8: (a) Objective function values for the models (b) Execution time of one discharge cycle for the models

from Model #3 to Model #4 is quite significant. One can conclude the best fit for further control application is Model #3, as it provides the least discrepancy between the experimental data and simulation results, without excessive computational cost.

3.6 Conclusions

This chapter performs parameter sensitivity analysis and identification for a variety of zero-dimensional physics-based Li-S battery models. The author provides answers to the questions listed in Introduction: (i) The intermediate reactions between S_8 and S_4^{2-} add slope to the second half of the high plateau, while the reactions between S_4^{2-} and S^{2-} prolong the flat portion of this plateau and deepen the inter-plateau voltage dip. (ii) Sensitivity analysis provides guidance on the final choice of to-be-identified parameters as E_j^0 (the voltage level), γ (the low plateau slope), ω (the low plateau duration) and $m_{S_8}^0$ (the dip location). (iii) Taking into account the intermediate reactions affecting the high plateau, the estimated voltage curve fits

the experimental data well except at the beginning of discharge. Finally, taking into account the importance of balancing parameter identification performance versus execution time, the author recommends Model #3 as the best model for use in future control-oriented applications under this model structure. This recommendation is made with the understanding that significant changes in battery chemistry, design, and/or cycling conditions may necessitate the introduction of additional modeling features, one example being the need to model diffusion dynamics, particularly for battery cells with greater electrode thicknesses compared to ones examined herein. The state estimation study in the following chapter is based on Model #3.

Chapter 4: Online State Estimation for a Zero-dimensional Lithium-Sulfur Battery Model

4.1 Overview

This chapter examines the problem of using measurements of input current and output cell voltage to estimate the internal state of a Lithium-Sulfur (Li-S) battery. Examples of state estimation problems include estimating a given battery's state of charge (SOC), state of health (SOH), and state of power (SOP). The main goal of this chapter is to estimate the masses of the different species that participate in Li-S battery redox reactions. Species mass estimation is valuable, because it provides a more detailed picture of what is occurring inside an electrochemical battery compared to, say, SOC estimation alone[1].

The motivation for Li-S state estimation is the *fundamentally different* behaviors compared to more traditional Lithium-ion batteries, including self-discharge through the shuttle effect. Fundamental insights from the existing Lithium-ion battery state estimation literature [62, 63, 64, 65], while quite valuable, are therefore not always directly applicable to the Li-S state estimation problem. Consider, for

[1]The materials in this chapter appear in an archival publication in the Journal of Power Source [61]

example, the question of whether or not the internal state of an electrochemical battery is observable (i.e., can be estimated from input-output data). The answer to this question depends partly on the given battery's internal dynamics, and can therefore change significantly based on whether or not the battery experiences self-discharge. The problem of designing Li-S battery management systems (BMSs) is important for protecting cells from damage, prolonging battery cycle life, and increasing battery performance metrics such as output power. Typical components of a BMS include a computationally affordable model, a state estimator, and ultimately an optimal control strategy. This chapter focuses on state estimation, a key element within BMS design.

Estimating the state of a dynamic system requires a representation, or model, of the system's underlying dynamics. This model can be derived from the fundamental laws of electrochemistry. It can also be fitted to experimental data using either equivalent circuit methods or machine learning. The literature provides at least three different types of Li-S battery models, as discussed in [66], namely: equivalent circuit models (ECMs) [34, 35, 36, 37], zero-dimensional electrochemical models [18, 19], and spatially-distributed electrochemical models [12, 13, 14, 15, 16, 17, 33]. These models fall on a spectrum of fidelity and complexity levels. Spatially-distributed electrochemical models, for instance, have the advantage of providing higher-fidelity representations of the underlying battery physics compared to equivalent circuit models, at the cost of higher computational complexity. Spatially-invariant zero-dimensional models, as discussed in Chapter 3, provide an attractive middle ground between these two extremes by modeling the underlying redox reactions in Li-S

batteries while minimizing computational complexity.

Existing research on Li-S battery state estimation relies predominantly on either equivalent circuit models or machine learning methods or both. For example, state estimation techniques have been applied to Li-S ECMs in [40, 41, 42] and to machine learning models in [43]. In [40], the extended Kalman filtering (EKF), unscented Kalman filtering (UKF), and particle filtering techniques are compared for experimental Li-S SOC estimation. In [41], an adaptive neuro-fuzzy inference systems algorithm is developed to estimate the SOC based on real-time cell model ECM parameterization. In [42], a dual Kalman filtering technique is used for combined Li-S state and parameter estimation, Finally, in [43], a Long Short-Term Memory Recurrent Neural Network model is built and calibrated for online Li-S state estimation.

The above literature, while encouraging, does not address the problem of estimating the masses of the various species participating in Li-S battery redox reactions. This is an important problem because unlike traditional Lithium-ion batteries, where Lithium intercalates into and out of the electrode materials, the Li-S chemistry involves multiple reduction reactions that convert S_8 gradually to S^{2-} during discharge. This makes the definition of SOC in Li-S batteries a little ambiguous, in the sense that one can potentially define multiple "states of charge" associated with different reacting species. One possible solution to this problem is: instead of estimating a single overall SOC, one can estimate internal state variables such as the active masses of dissolved sulfur species using a physics-based model. Such state estimation provides a more detailed picture of the internal state of the battery.

This, in turn, is potentially useful for predicting and managing phenomena such as the dependence of Li-S discharge capacity on applied current [1].

The main goal of this chapter is to estimate the species masses in a Li-S battery using a zero-dimensional, physics-based model. The particular model used here builds on earlier research in the literature, including previous work by the author on the experimental parameterization and validation of the model [56], presented in Chapter 3. To the best of the author's knowledge, this chapter's use of a zero-dimensional, physics-based model for online species mass estimation is a novel contribution to the literature. Key elements of this contribution include: (i) an observability analysis for the selected Li-S battery model, (ii) the use of model reduction to improve this model's observability, especially in the low plateau region, (iii) the development of the desired Li-S state estimator using unscented Kalman filtering, and (iv) simulation-based validation of the estimator.

The remainder of this chapter is organized as follows. Firstly, this chapter describes the zero dimensional model structure adopted from [18, 19], and reformulates this model from a set of differential algebraic equations (DAEs) to a set of ordinary differential equations (ODEs). Secondly, the author analyzes the model's observability, and relates the observability gramian to Fisher information matrix to obtain the best achievable estimation error bounds on initial states. Moreover, when mass conservation is considered, the number of state variables can be reduced by two and the observability is improved, especially in the low plateau region. Finally, the simulation results of the UKF-based state estimation for both the full-order and reduced-order ODE models are presented and discussed in detail.

Indices	Reactions and Species
Reaction Index j = 1, 2, 3, 4	$\frac{1}{2}S_8 + e^- \rightleftharpoons \frac{1}{2}S_8^{2-}$ $\frac{3}{2}S_8^{2-} + e^- \rightleftharpoons 2S_6^{2-}$ $S_6^{2-} + e^- \rightleftharpoons \frac{3}{2}S_4^{2-}$ $\frac{1}{6}S_4^{2-} + e^- \rightleftharpoons \frac{2}{3}S^{2-}$
Reaction Index i = 1, 2, ..., 5	$S_8,\ S_8^{2-}, S_6^{2-}, S_4^{2-}, S^{2-}$

Table 4.1: Reactions and dissolved species considered in the model

4.2 Lithium-Sulfur Battery Model

The zero-dimensional model used here makes the following assumptions: (i) there is an unlimited lithium supply in the cell with a negligible overpotential on the anode side, as in [13]; (ii) the shuttle effect of polysulfides is not included due to the focus on the voltage performance instead of capacity fade [19]; (iii) only the lowest polysulfide's precipitation reaction ($2Li^+ + S^{2-} \rightleftharpoons Li_2S \downarrow$) is modeled [18, 19]; and (iv) only the redox reactions in Table 4.1 are considered. Although there exist different simplifications of the reaction chain on the cathode side, our choice of the reaction chain is based on previous work by the author [56]. This previous work involved both estimating this model's parameters from experimental cycling data and validating the model's accuracy in capturing Li-S battery discharge dynamics.

4.2.1 Model Derivation

The model in this work captures the physics of key reactions and precipitation phenomena in Li-S batteries. Moreover, by its very nature as a zero-dimensional

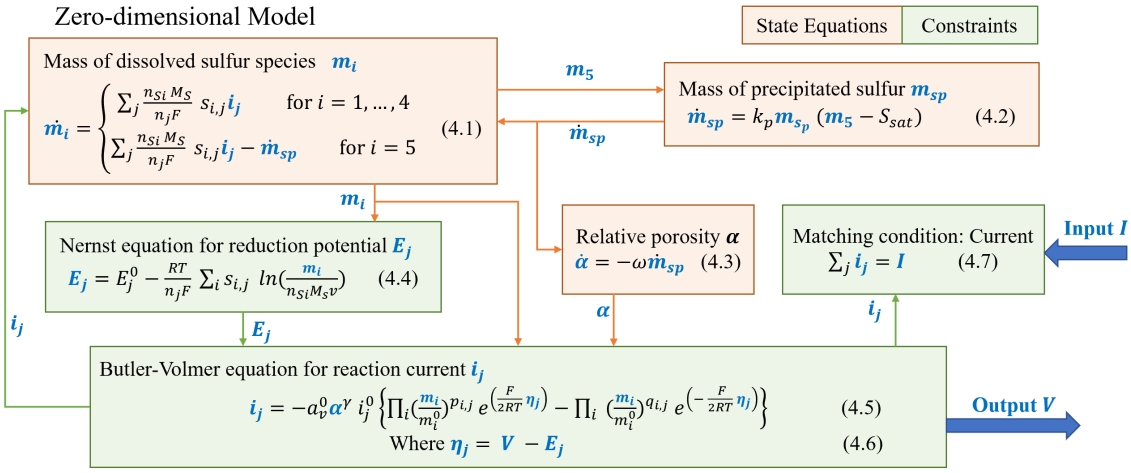

Figure 4.1: The structure of the zero-dimensional Li-S battery model

model, it neglects diffusion/migration dynamics for simplicity. These dynamics lead to the time evolution of the model's state variables, namely: the masses of the various sulfur species and the porosity of the cathode material. The resulting differential algebraic equation (DAE) model (where positive current denotes discharge) and the information flow are shown in Fig 4.1.

The input of the system is external current I, and the output of the system is the cell voltage V. The state variables include: the masses of the dissolved sulfide species m_i $(i = 1, ..., 5)$, the mass of the precipitated sulfur m_{S_p}, and the relative porosity of the cathode material α. The rates of mass change for higher-order dissolved sulfide species relate to the current i_j generated by reaction j $(j = 1, ..., 4)$. For the last dissolved species S^{2-}, one needs to consider its mass generation from the last reduction reaction and its mass loss due to precipitation as in Eqn. 4.1. The nucleation and growth phenomenon is described by Eqn. 4.2. The parameters k_p and S_{sat} are the precipitation rate constant and the saturation mass of S^{2-}. The rate of change of the mass of the precipitate is partly driven by the precipitated

mass. This reflects the fact that the existing precipitate serves as a nucleus for further precipitation/growth, as long as the mass in the electrolyte is above a given saturation mass S_{sat}. Relative porosity equals the current porosity of the cathode material divided by initial porosity, and has a direct effect on the active reaction area [12]. Its rate of change is described in Eqn. 4.3, with a rate constant ω. The parameters n_{S_i}, n_j, R, T, v, M_s, F and $s_{i,j}$ represents the number of sulfur atoms in species i, number of electrons exchanged in reaction j, gas constant, temperature, cell volume, molar mass of a sulfur atom, Faraday's constant, and stoichiometric coefficients of the reactions, respectively. The coefficients $p_{i,j}$ and $q_{i,j}$ represent the positive and negative elements of $s_{i,j}$.

The reduction potential of each reaction E_j is given by the Nerst equation (Eqn. 4.4), assuming that E_j^0 is the corresponding reference potential [19]. The current generated by the corresponding reduction reaction is described by the Butler–Volmer equation (Eqn. 4.5), where η_j is the overpotential, i_j^0 is the exchange current density, γ is a morphology parameter serving as the power of the relative porosity and m_i^0 is the initial mass of species i. All these currents sum to the external discharge current I (Eqn. 4.7). The parameter values used in the following study are obtained from [56], as shown in Table 4.2.

One can also write the model in semi-explicit form, as listed below:

$$\dot{X} = f(X, I) \tag{4.8}$$

$$0 = g(X, Z, I, V) \tag{4.9}$$

Notations	**Values**	**Units**
E_j^0	2.4673, 2.3742, 2.3420, 2.0693	V
i_j^0	2.00, 0.02, 0.02, 0.02	A/m^2
m_i^0	3.0377, 1.83E-05, 1.83E-05 1.83E-05, 3.26E-06	g
v	0.0114	L
S_{sat}	0.0001	g
a_v^0	1	m^2
γ	0.4832	-
ω	0.6133	1/g
k_p	22	1/(g s)
M_s	32	g/mol
n_{S_i}	8, 8, 6, 4, 1	-
n_j	1, 1, 1, 1	-
R	8.3145	J/(K mol)
F	9.649×10^4	C/mol
T	298	K
s_{ij}	$\begin{pmatrix} -1/2 & 0 & 0 & 0 \\ 1/2 & -3/2 & 0 & 0 \\ 0 & 2 & -1 & 0 \\ 0 & 0 & 3/2 & -1/6 \\ 0 & 0 & 0 & 2/3 \end{pmatrix}$	-

Table 4.2: Key parameter values in simulations

where $X = [m_1, ..., m_5, m_{S_p}, \alpha]^T$, $Z = [i_j, E_j, \eta_j]^T$. The state equations include Eqn. 4.1-4.3, and algebraic constraints can be rearranged from Eqn. 4.4-4.7.

4.2.2 Model Reformulation

The Li-S battery model is a differential algebraic equation (DAE) model. State estimators exist for such models [67, 68], but the fundamental theoretical foundations of estimation theory are more established for traditional explicit ordinary differential equation (ODE) models. Methods exist in the literature for solving such a DAE system numerically and/or using perturbation methods to reduce its index, thereby obtaining a set of ODEs [69, 70]. Another way of converting a DAE model to ODEs is to solve for the algebraic variables explicitly (if possible), obtaining an analytical solution. With this in mind, the author employs the second approach, namely, analytically resolving the algebraic loop in the above DAE model, thereby reformulating it into an ODE model. This reformulation also eliminates the need for determining consistent initial conditions for the DAE model, thereby also simplifying the estimation problem. From the information flow described in Fig. 4.1, one can identify that solving Eqn. 4.7 analytically is sufficient for the model reformulation. The goal is to solve for the reaction current i_j in Eqn. 4.7. To do so, the author first solves for the output voltage measurement V using the following steps: Firstly, substitute Eqn. 4.4 and 4.6 into Eqn. 4.5, and rearrange to get Eqn. 4.10:

$$i_j = -a_v^0 \alpha^\gamma \left(\frac{Y}{\Omega_{1j}} \prod_i m_i^{p_{i,j}+\frac{1}{2}s_{i,j}} - \frac{Y^{-1}}{\Omega_{2j}} \prod_i m_i^{q_{i,j}-\frac{1}{2}s_{i,j}} \right) \tag{4.10}$$

where

$$Y = e^{\frac{F}{2RT}V} \tag{4.11}$$

$$\Omega_{1j} = \frac{1}{i_j^0} e^{(\frac{F}{2RT}E_j^0)} \prod_i m_i^{p_{i,j}} (n_{S_i} M_s v)^{\frac{1}{2}s_{i,j}} \tag{4.12}$$

$$\Omega_{2j} = \frac{1}{i_j^0} e^{(-\frac{F}{2RT}E_j^0)} \prod_i m_i^{q_{i,j}} (n_{S_i} M_s v)^{-\frac{1}{2}s_{i,j}} \tag{4.13}$$

Now, substitute Eqn. 4.10 into Eqn. 4.7 to get:

$$\Delta_1 Y - \Delta_2 Y^{-1} + \frac{I}{a_v} = 0 \tag{4.14}$$

where

$$\Delta_1 = \sum_j \left(\frac{\prod_i m_i^{p_{i,j}+\frac{1}{2}s_{i,j}}}{\Omega_{1j}} \right) \tag{4.15}$$

$$\Delta_2 = \sum_j \left(\frac{\prod_i m_i^{q_{i,j}-\frac{1}{2}s_{i,j}}}{\Omega_{2j}} \right) \tag{4.16}$$

One can solve for Y from the quadratic function in Eqn. 4.14. Since Y is an exponential function, it is always a positive scalar. This makes it possible to finally determine an analytic solution for the voltage measurement, V:

$$V = \frac{2RT}{F} \ln \left(\frac{-\frac{I}{a_v} + \sqrt{\frac{I^2}{a_v^2} + 4\Delta_1\Delta_2}}{2\Delta_1} \right) \tag{4.17}$$

In this way, the algebraic loop is broken, and the resulting model can be expressed

in the following standard explicit state-space form:

$$\dot{X} = f(X, I) \tag{4.18}$$

$$V = h(X, I) \tag{4.19}$$

where the state variables form a 7-by-1 vector:

$$X = [m_1, ..., m_5, m_{S_p}, \alpha]^T \tag{4.20}$$

The above model serves as a foundation for the observability analysis and estimation study presented in the remainder of this chapter. One important note is that the precipitated mass m_{S_p} does not directly affect the output battery voltage V. Instead, the impact of precipitation on this output voltage takes place indirectly, through the dynamics of other species masses. This causes the observability of the precipitated mass to be fairly weak, especially in the low plateau region, as discussed in the following sections.

4.3 Observability Analysis

In control theory, observability is an indicator of whether or not the internal state of a dynamic system can be estimated from input/output measurements. For linear systems, the conditions for observability are uniquely/equivalently defined: a linear time invariant system is observable, if and only if the observability matrix is full rank or equivalently the observability gramian is non-singular. In contrast, there

are multiple different tests for observability in nonlinear systems [71]. This section analyzes the so-called "weak observability" of the Li-S ODE model, defined as one's ability to estimate the model's state within a local neighborhood of its true value. This analysis furnishes a Cramér-Rao bound on the best-achievable state estimation accuracy for any give charge/discharge profile and time period, assuming a known measurement noise distribution. The first goal of this analysis is to confirm that the model is locally observable, thereby justifying the subsequent development of an estimator. The second goal is to compare observability for different state variables during different phases of battery operation (e.g., high plateau, low plateau, etc.).

One method to solve the problem of estimating the current state of a dynamic system can be done in two steps: (i) estimating the system's initial state and (ii) propagating the initial state though the system model to obtain the current state. The empirical observability gramian adopts this idea [72]. The observability gramian is calculated by perturbing the initial state X_0 along each state variable by a positive small value ε, and then simulating the system for a time period τ to get the resulting differences in output measurements. This furnishes the following equation for the observability gramian:

$$W_o^{\varepsilon}(\tau, X_0, I) = \frac{1}{\varepsilon^2} \int_0^{\tau} \Phi^{\varepsilon}(t, X_0, I)^T \Phi^{\varepsilon}(t, X_0, I) dt \tag{4.21}$$

where

$$\Phi^{\varepsilon}(t, X_0, I) = [V^{+1} - V^1, \quad ... \quad , V^{+n} - V^n] \tag{4.22}$$

$$V^{+i} = h(X(t, X_0 + \varepsilon e_i), I) \tag{4.23}$$

$$V^i = h(X(t, X_0), I) \qquad \text{for } i = 1, ..., n \tag{4.24}$$

The vectors e_i represent the elements of the standard basis in the state variable domain $\mathbb{R}^n$ (e.g., $e_1 = [1\ 0\ 0\ 0\ 0\ 0\ 0]^T$), and n equals 7. If the observability gramian is non-singular, the nonlinear system is locally observable, which means that one can estimate the initial values of its state variables from input/output measurements. The best theoretically achievable accuracy with which such estimation can be performed is governed by the associated Fisher information matrix [73]. This matrix is formally derived in [74]. Moreover, assuming that the voltage output measurement noise process is white and Gaussian, this Fisher information matrix can be simplified to the following expression:

$$F_M = \frac{1}{\sigma_v^2} \sum_{k=1}^{N} \left[\left(\frac{\partial \mathbf{V}}{\partial X_0} \right) \left(\frac{\partial \mathbf{V}}{\partial X_0} \right)^T \right] \tag{4.25}$$

In the above equation, N is the number of samples within the time period τ, (boldface) $\mathbf{V}$ is a 1-by-N row vector of voltage measurements at every time step, and the sampling time step is $\delta t = \frac{\tau}{N}$. When the sampling time step is small enough, the above equation for the Fisher information matrix can be approximated using the

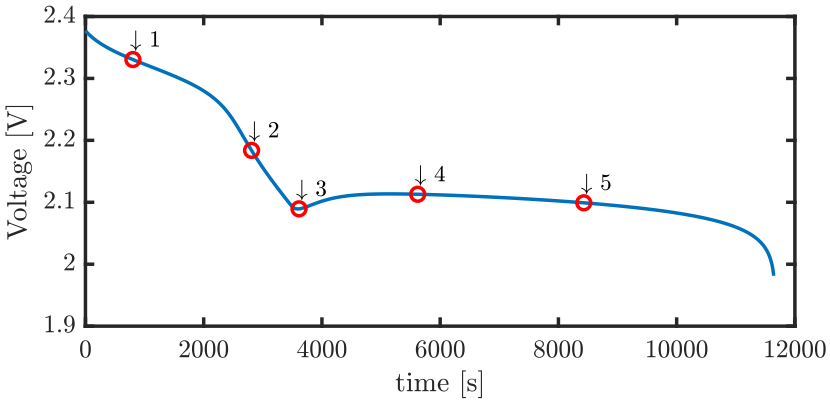

Figure 4.2: Observability check points along the voltage profile

following integral [75]:

$$\begin{aligned} F_M &= \frac{1}{\sigma_v^2\ \delta t} \int_0^\tau \left(\frac{\partial V}{\partial X_0}\right) \left(\frac{\partial V}{\partial X_0}\right)^T dt \\ &= \frac{1}{\sigma_v^2\ \delta t} W_o^\varepsilon(\tau, X_0, I) \end{aligned} \tag{4.26}$$

When the Fisher matrix is invertible (i.e. the system is locally observable), then the inverse of the matrix provides a Cramér-Rao lower bound (CRLB) that represents the best achievable estimation error covariance for the estimated initial state vector X_0.

$$cov(X_0) \geq F_M^{-1} = \sigma_v^2\ \delta t\ W_o^\varepsilon(\tau, X_0, I)^{-1} \tag{4.27}$$

Due to the nonlinearity and complexity of our system model, the author evaluates the observability gramian and the Cramér-Rao lower bound numerically along the system's discharge trajectory, given a constant discharge C-rate of 0.3C. The parameters used in this observability analysis are the perturbation $\varepsilon = 10^{-6}$, the sampling time step $\delta t = 0.1$ second, the time period $\tau = 60$ seconds, and the standard deviation of the output measurement $\sigma_v = 5 \times 10^{-3}$ V.

std [g]	Nr. 1	Nr. 2	Nr. 3	Nr. 4	Nr. 5
m_1	0.028	0.014	0.006	0.039	0.029
m_2	0.022	0.018	0.006	0.031	0.022
m_3	0.014	0.017	0.009	0.094	0.088
m_4	0.017	0.016	0.006	0.092	0.096
m_5	0.002	0.003	0.005	0.063	0.072
m_{S_p}	0.076	0.071	0.046	0.282	0.367
α	0.033	0.024	0.009	0.098	0.106

Table 4.3: Standard deviation of the best achievable estimation error for the full-order model

The author chooses five representative points (two points at each plateau and the middle dip point) to obtain the empirical observability gramian and CRLB along the voltage measurement profile, as shown in Fig 4.2. At all these 5 points, the empirical observability gramian is invertible, leading to the conclusion that the system is indeed locally (or "weakly") observable. This means that if the estimated initial states are in the neighborhood of the true values, one can construct an unbiased observer for the system (i.e., an observer that converges to the true values in an average statistical sense). The best statistical accuracy (i.e., statistical spread of initial state estimates) achievable by this observer is given by the CRLB. Specifically, the square roots of the diagonal elements of the CRLB matrix represent the standard deviations (std) of the best achievable estimation error for each initial state variable. These standard deviations are listed in Table 4.3.

Two main observations are visible from Table 4.3. First, the best local observability shows up at the dip point between the high and low plateau. Estimation

errors are slightly worse in the high plateau compared to this dip point, and the worst estimation errors occur in the low plateau. This observation matches the intuition that the estimation problem is more difficult during the low plateau due to the associated flatness of the measured voltage profile. The smaller sensitivity of the output voltage with respect to underlying state variables in the lower plateau regions increases the difficulty of the state estimation problem, and therefore worsens estimation accuracy. Second, the largest standard deviation of the state estimation error corresponds to the mass of precipitated sulfur m_{S_p}. This is especially problematic in the low plateau region, where this error can be as large as 0.367 g (compared to the total active sulfur mass of 3.0377 g). This is due to the fact that the output voltage is not directly governed by the precipitated mass m_{S_p}, i.e. the variable m_{S_p} does not show up in the output equation, Eqn. 4.19. In practice, when performing state estimation during the low plateau, if the initial estimated m_{S_p} is not close to the true value, this error will persist.

4.3.1 Improving Observability through Model Reduction

When a dynamic system suffers from poor observability, one potential remedy is to estimate a subset of the system's state variables. This subset can be selected to ensure that it has attractive observability properties. Estimates of the remaining state variables must then be computed through other means, such as the exploitation of prior information. The principle of mass conservation provides an opportunity for improving the observability of this Li-S battery model. The basic idea is to assume

that the total active sulfur mass is accurately known *a priori*. Prior knowledge of this mass can be obtained from a number of different sources, one of which is state estimation during the high plateau. Armed with this prior knowledge, one can construct a reduced-order model where the principle of mass conservation is used to eliminate two state variables, namely: the precipitated sulfur mass and relative porosity. One can then construct an estimation algorithm for the remaining 5 state variables using the resulting reduced-order model.

Consider the mass conservation of all the sulfur species. The rate of change of the total sulfur mass is zero. One can therefore eliminate the state variable m_{S_p} as follows:

$$m_{S_p} = M_{tot} - \sum_{i=0}^{5} m_i \tag{4.28}$$

where M_{tot} represents the total sulfur mass, known *a priori*. Moreover, knowing that the initial relative porosity for a fully charged cell equals 1 by definition, and assuming the corresponding precipitated sulfur mass to be approximately 0, one can further reduce the state variable α from the model as follows:

$$\alpha = 1 - \omega(M_{tot} - \sum_{i=0}^{5} m_i) \tag{4.29}$$

The resulting reduced-order ODE model contains 5 state variables. The author performs the same observability analysis to obtain the standard deviations of the corresponding best achievable estimation errors. The results of this analysis are listed in Table 4.4. The observability of the masses of the dissolved species in the

std [g]	Nr. 1	Nr. 2	Nr. 3	Nr. 4	Nr. 5
m_1	0.007	0.009	0.005	0.027	0.030
m_2	0.021	0.015	0.006	0.024	0.020
m_3	0.014	0.013	0.006	0.059	0.088
m_4	0.015	0.009	0.006	0.052	0.071
m_5	0.002	0.002	0.003	0.062	0.056

Table 4.4: Standard deviation of the best achievable estimation error for the reduced-order model

5th-order model is on the same order of magnitude, and generally better, compared to the 7th-order model. More importantly, relative porosity and precipitated sulfur mass are no longer being directly estimated in this reduced-order model, the result being that their estimation accuracy is now a strong function of the fidelity of the prior estimate of total sulfur mass. Accurate prior knowledge of this total mass can therefore benefit the estimation process, as demonstrated in the following discussions. The remainder of this chapter develops and simulates an unscented Kalman filter for estimating the state variables of both of the above 7th-order full model and 5th-order reduced model.

4.4 State Estimation using UKF

Kalman filtering is a popular and well-established approach for state/parameter estimation. The traditional Kalman filter provides state estimates for linear dynamic systems, but nonlinear extensions of this filter exist, including both the extended and unscented Kalman filters. Compared to the extended Kalman filter (EKF), the use

of sigma points for propagating estimation covariance in unscented Kalman filters generally improves estimation accuracy [76, 77, 78]. This section applies unscented Kalman filtering to the full and reduced-order Li-S ODE models, and evaluates the performance of the resulting filters in simulation.

4.4.1 The UKF Algorithm

The state and output equations of the nonlinear Li-S battery model can be discretized in time and augmented with both process and measurement noise signals as below:

$$X_k = f(X_{k-1}, I_k) + v_k \tag{4.30}$$

$$V_k = h(X_k, I_k) + w_k \tag{4.31}$$

In the above discrete-time model, v_k and w_k are the process and measurement noise, respectively, which are both uncorrelated zero-mean Gaussian white sequences with known variances. Then, the UKF algorithm is shown as follows.

(1) Initialization:

Define an initial state estimate $\hat{X}_0$ and covariance matrix P_0. In this work, the initial covariance matrix P_0 is set as $diag(P_0) = 0.1\hat{X}_0$.

(2) Generate sigma points at time step k-1:

$$\chi_{k-1}^{0} = \hat{X}_{k-1} \tag{4.32}$$

$$\chi_{k-1}^{i} = \hat{X}_{k-1} + \sqrt{(N+\lambda)P_{k-1}} \quad i = 1, ..., N \tag{4.33}$$

$$\chi_{k-1}^{i} = \hat{X}_{k-1} - \sqrt{(N+\lambda)P_{k-1}} \quad i = N+1, ..., 2N \tag{4.34}$$

where λ is a scaling factor

$$\lambda = \beta^2(N+\kappa) - N \tag{4.35}$$

Here $\beta \in [0, 1]$ and $\kappa \in [0, \infty]$ are two tuning parameters that determine the spread of the sigma points. In this study, the author chooses $\beta = 0.01$ and $\kappa = 1$.

(3) Time update:

The sigma points are propagated through the nonlinear discrete state equation to obtain the estimated state matrix χ_k^{i-}

$$\chi_k^{i-} = f(\chi_{k-1}^{i}, I_k) \quad i = 0, ..., 2N \tag{4.36}$$

The *a priori* state estimate is then given by:

$$\hat{X}_k^- = \sum_{i=0}^{2N} W_i^m \chi_k^{i-} \tag{4.37}$$

$$W_0^m = \frac{\lambda}{\lambda + N} \tag{4.38}$$

$$W_i^m = \frac{\lambda}{2\lambda + 2N} \quad i = 1, ..., 2N \tag{4.39}$$

Moreover, the *a priori* error covariance is calculated as

$$P_k^- = \sum_{i=0}^{2N} W_i^c [\chi_k^{i-} - \hat{X}_k^-][\chi_k^{i-} - \hat{X}_k^-]^T + Q_k \tag{4.40}$$

$$W_0^c = \frac{\lambda}{\lambda + N} + (1 - \beta^2 - \mu) \tag{4.41}$$

$$W_i^c = \frac{\lambda}{2\lambda + 2N} \quad i = 1, ..., 2N \tag{4.42}$$

In this work, a constrained version of the UKF which considers allowable limits on species mass values is implemented. The sizing of the process noise covariance matrix is used for adjusting the spread of the UKF sigma points. It does not necessarily imply or preclude the existence of substantial process noise in the physical system. A bigger covariance matrix leads to a broader spread of the sigma points. If Q_k is too big, it is possible to generate infeasible sigma points with negative species mass values. Hence, the authors enforce a cap on the maximum values of the diagonal elements of Q_k as below:

$$diag(Q_k) = min[0.005, \quad 0.005\hat{X}_{k-1}] \tag{4.43}$$

The estimated measurement matrix Z_k, is calculated by transforming the sigma points using the nonlinear discrete output equation

$$Z_k^i = h(\chi_{k-1}^i, I_k) \quad i = 0, ..., 2N \tag{4.44}$$

Moreover, the estimated measurement $\hat{V}_k$ is given by:

$$\hat{V}_k = \sum_{i=0}^{2N} W_i^m Z_k^i \tag{4.45}$$

(4) Measurement update:

The Kalman gain K_k is calculated from the measurement covariance P_z and the cross-correlation covariance P_{xz}

$$P_z = \sum_{i=0}^{2N} W_i^c [Z_k^i - \hat{V}_k][Z_k^i - \hat{V}_k]^T + R_k \tag{4.46}$$

$$P_{xz} = \sum_{i=0}^{2N} W_i^c [\chi_k^{i-} - \hat{X}_k^-][Z_k^i - \hat{V}_k]^T \tag{4.47}$$

$$K_k = P_{xz} P_z^{-1} \tag{4.48}$$

where $R_k = \sigma_v^2$, with the standard deviation of the output measurement $\sigma_v = 5 \times 10^{-3}$ V.

The state estimate is updated by the measurement

$$\hat{X}_k = \hat{X}_k^- + K_k(V_k - \hat{V}_k) \tag{4.49}$$

Finally, the error covariance matrix is updated through

$$P_k = P_k^- - K_k P_z K_k^T \tag{4.50}$$

4.4.2 Simulation Results and Discussion

The UKF algorithm is tested both in the high and low plateau regions in simulation, for both the full- and reduced-order models. Although state estimation is performed at different check points, consistent results are observed for points located in the same plateau region. The author therefore chooses one initial state for each plateau as representatives for demonstration and discussion. For the full-order ODE model, a constant current discharge scenario is tested with the discharge current set to 1 Ampere (corresponding to a C-rate of 0.3C). This simulated scenario is repeated for the reduced-order model. The author also simulates the reduced-order model for a sinusoidal current input, as discussed below.

4.4.2.1 State Estimation for Full-order ODE Model

Fig. 4.3 and 4.4 show the simulation results for the full-order ODE model with a constant current input of 1 Ampere. In the high plateau region, the masses of the three main species S_8, S_8^{2-} and S_6^{2-} demonstrate good convergence. The masses of both the sulfur precipitate and dissolved S^{2-} are small in this region, and so are the UKF estimates of these masses. Broadly speaking, therefore, the performance of the full-state UKF estimator in the high plateau region is reasonable. This is consistent with the earlier analysis showing good state observability in this region.

An obvious disadvantage shows up in the estimation of precipitated sulfur mass: this precipitated mass is estimated with poor accuracy, especially in the low plateau region. Errors in estimating this precipitated mass do not converge to

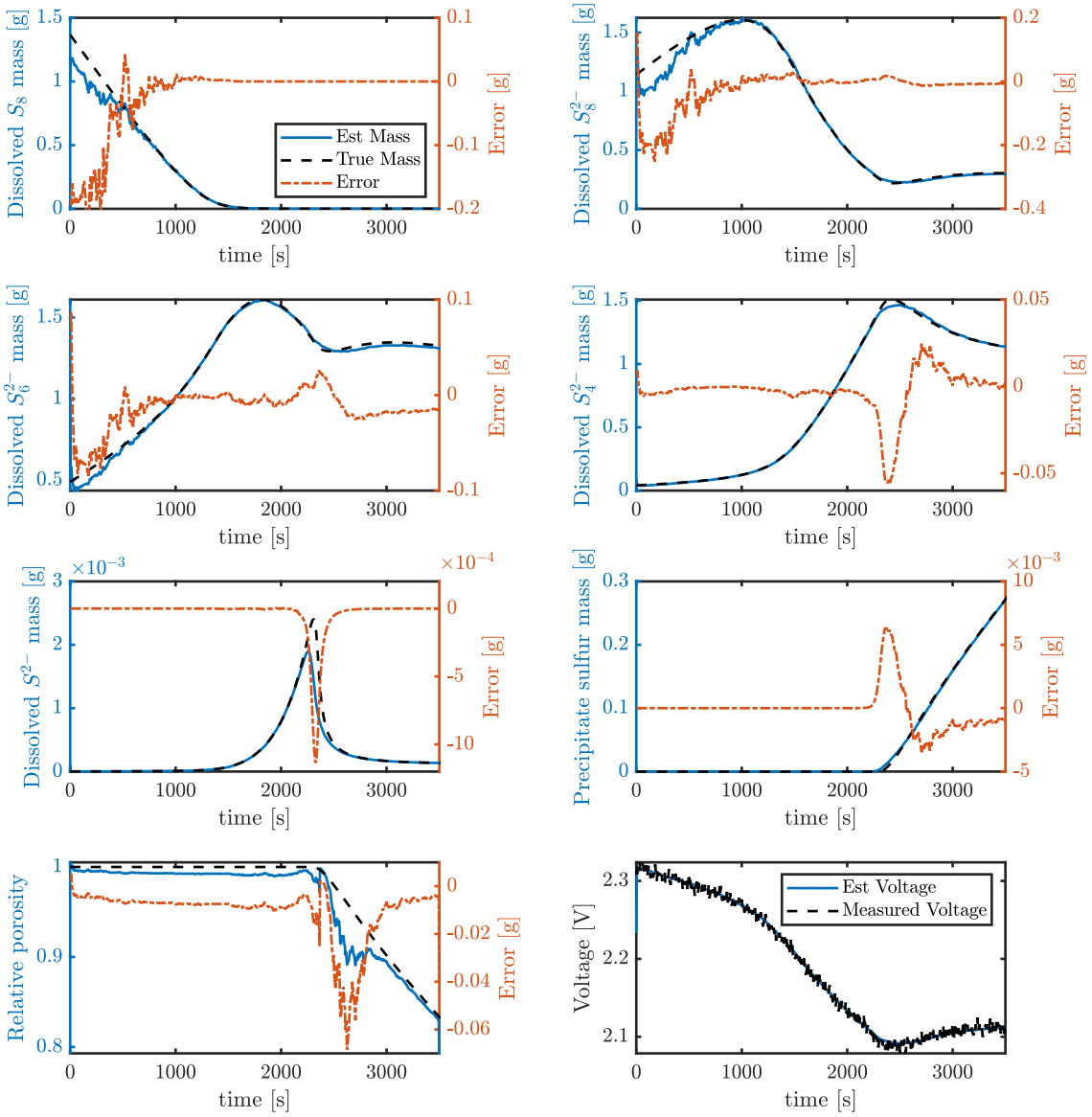

Figure 4.3: High plateau state estimation with a constant discharge current for the full-order model

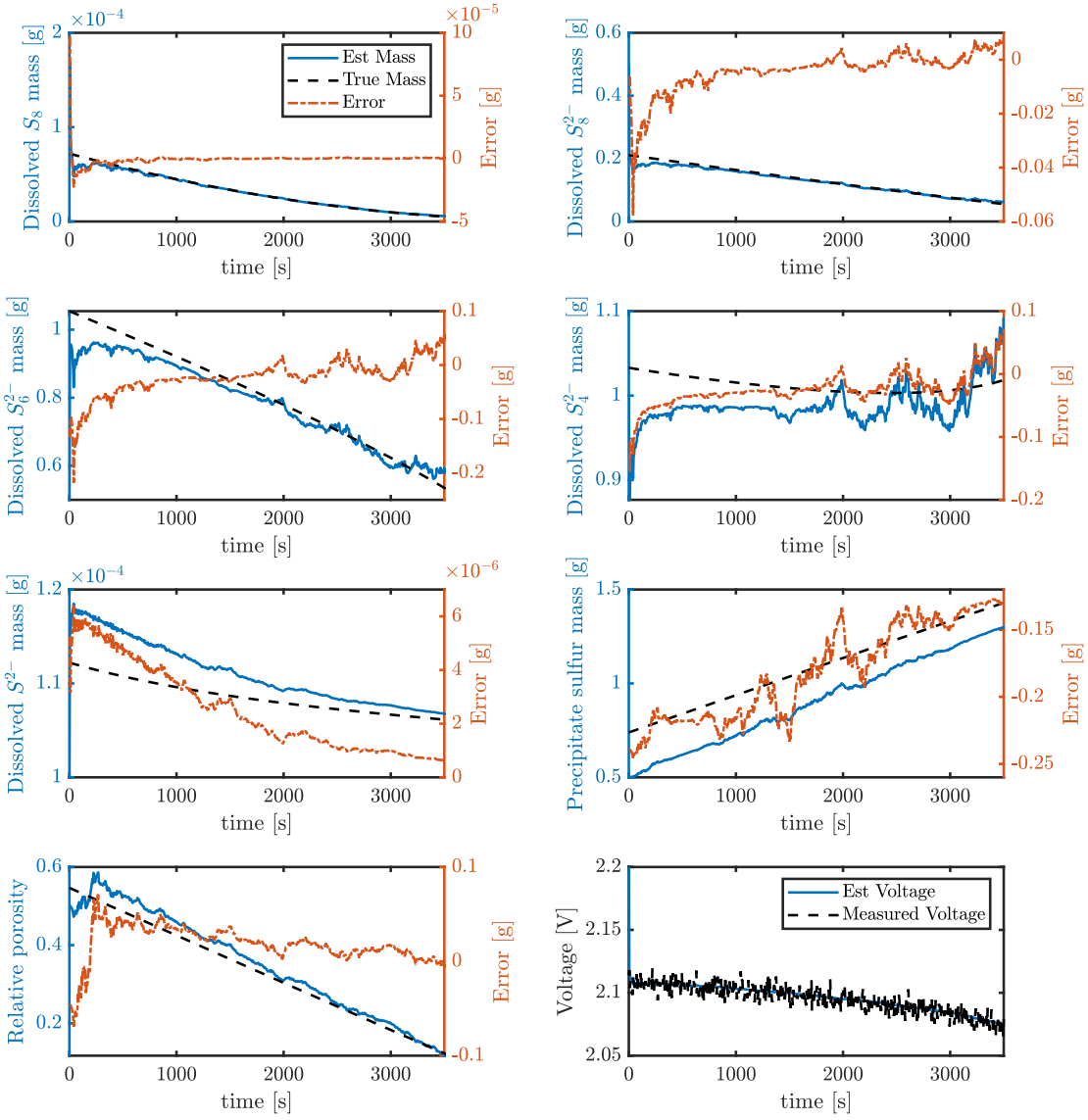

Figure 4.4: Low plateau state estimation with a constant discharge current for the full-order model

negligible values even after an hour of battery discharge, as shown in Fig. 4.4. This can be explained by the observability analysis earlier in this chapter. The output voltage measurement only relates to the dissolved sulfur species, as they affect the associated reduction potentials through the Nernst equation. When performing state estimation in the low plateau region, if the initial estimated m_{S_p} is not close to the true value, the error will persist without substantial improvement. This is a fundamental issue, rather than a problem specific to the filtering algorithm used in this work, as evident from the earlier observability analysis.

4.4.2.2 State Estimation for Reduced-order ODE Model

Two simulation scenarios are examined for unscented Kalman filtering using the reduced-order battery model, namely: a 1-Ampere constant-current discharge scenario and a sinusoidal input current scenario with $I = 1 + sin(0.005t)$ Ampere. The simulation results for high plateau estimation with both of these current profiles are shown in Fig. 4.5 and 4.6, respectively. One can observe the state estimates converge to the true value within about 5 minutes. The slow-changing current input does not lead to significant change in the convergence rate.

Fig. 4.7 and 4.8 present the estimation results for the low plateau. The convergence of the estimator takes more time in the low plateau region. This is because the low plateau manifests less observability, and the estimator requires a longer time duration to gather information. This poor observability can be explained in terms of the reduced sensitivity of the output voltage to the values of the underlying

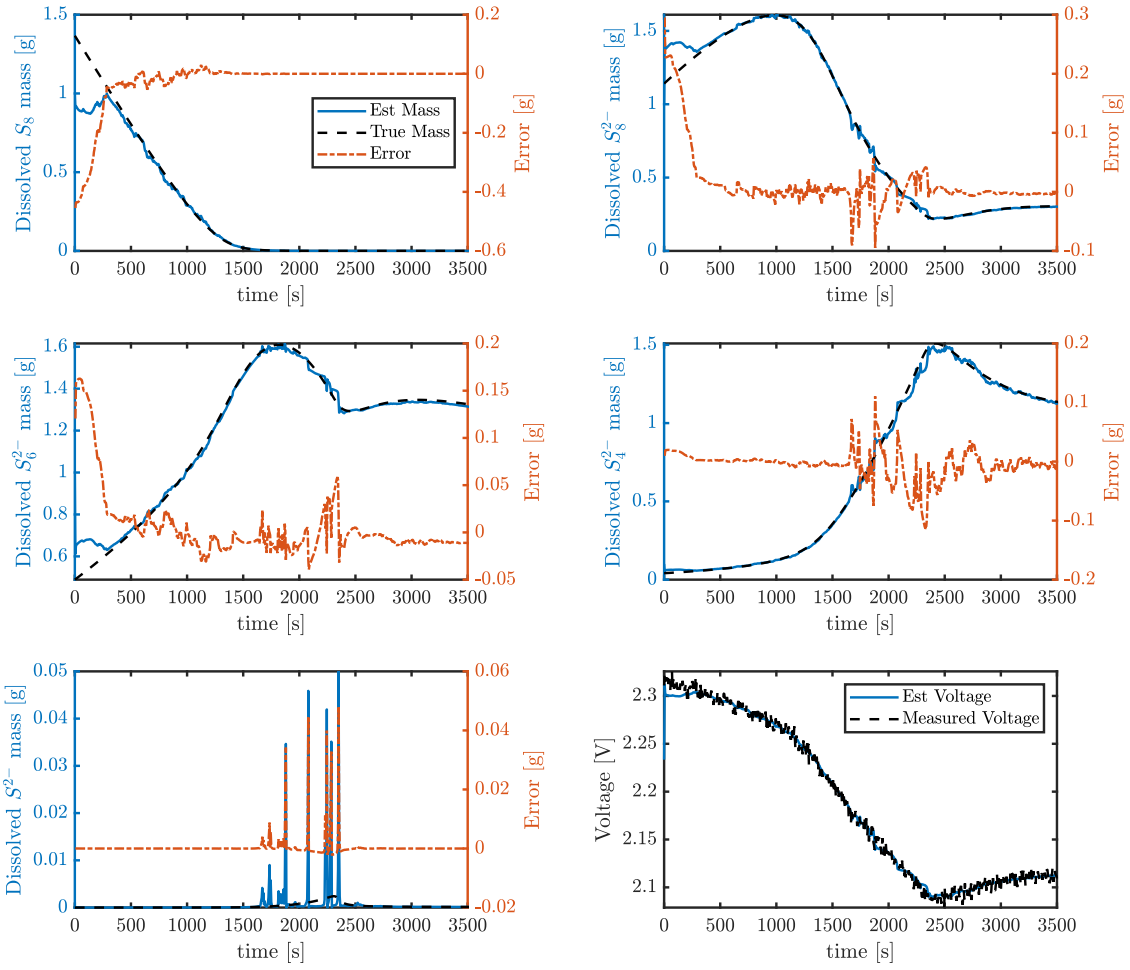

Figure 4.5: High plateau state estimation with a constant discharge current for the reduced-order model

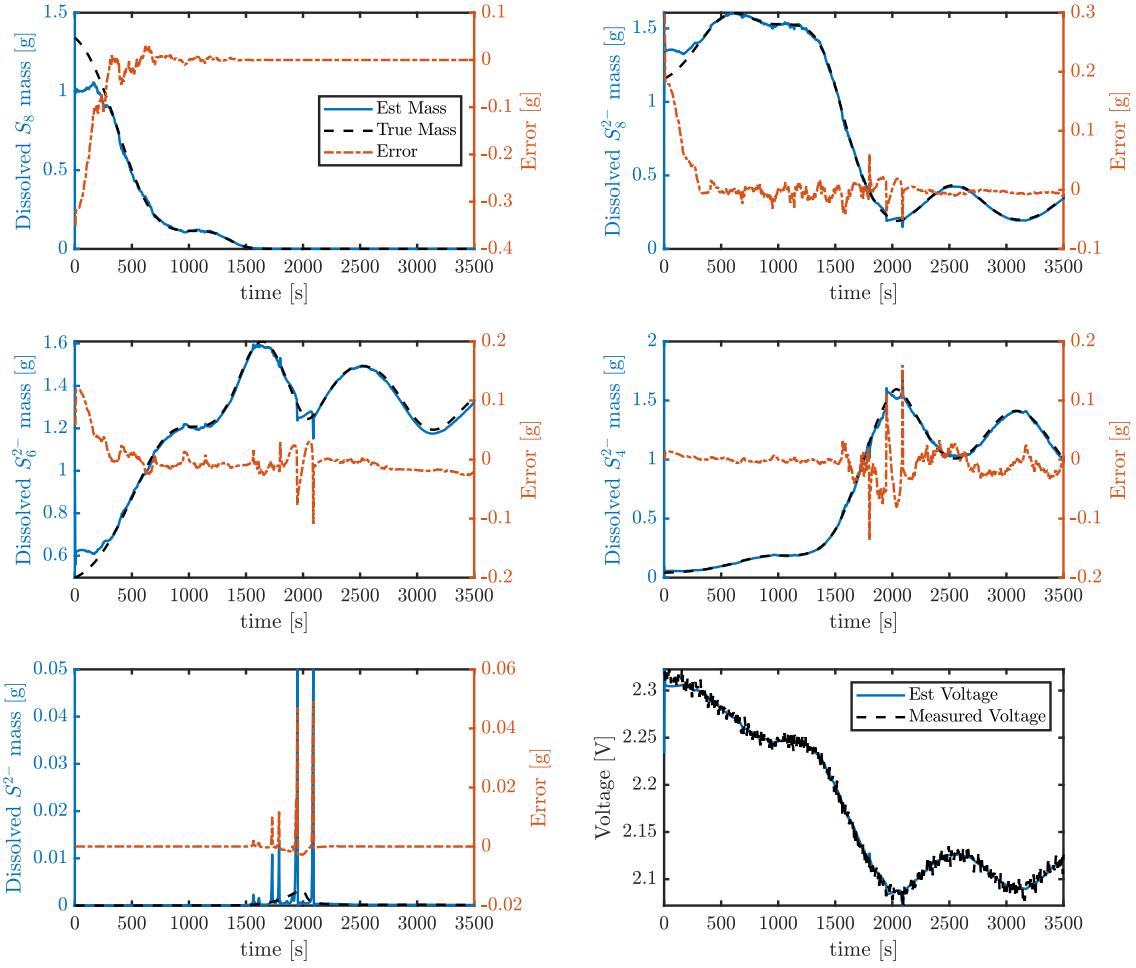

Figure 4.6: High plateau state estimation with a constant plus sinusoidal discharge current for the reduced-order model

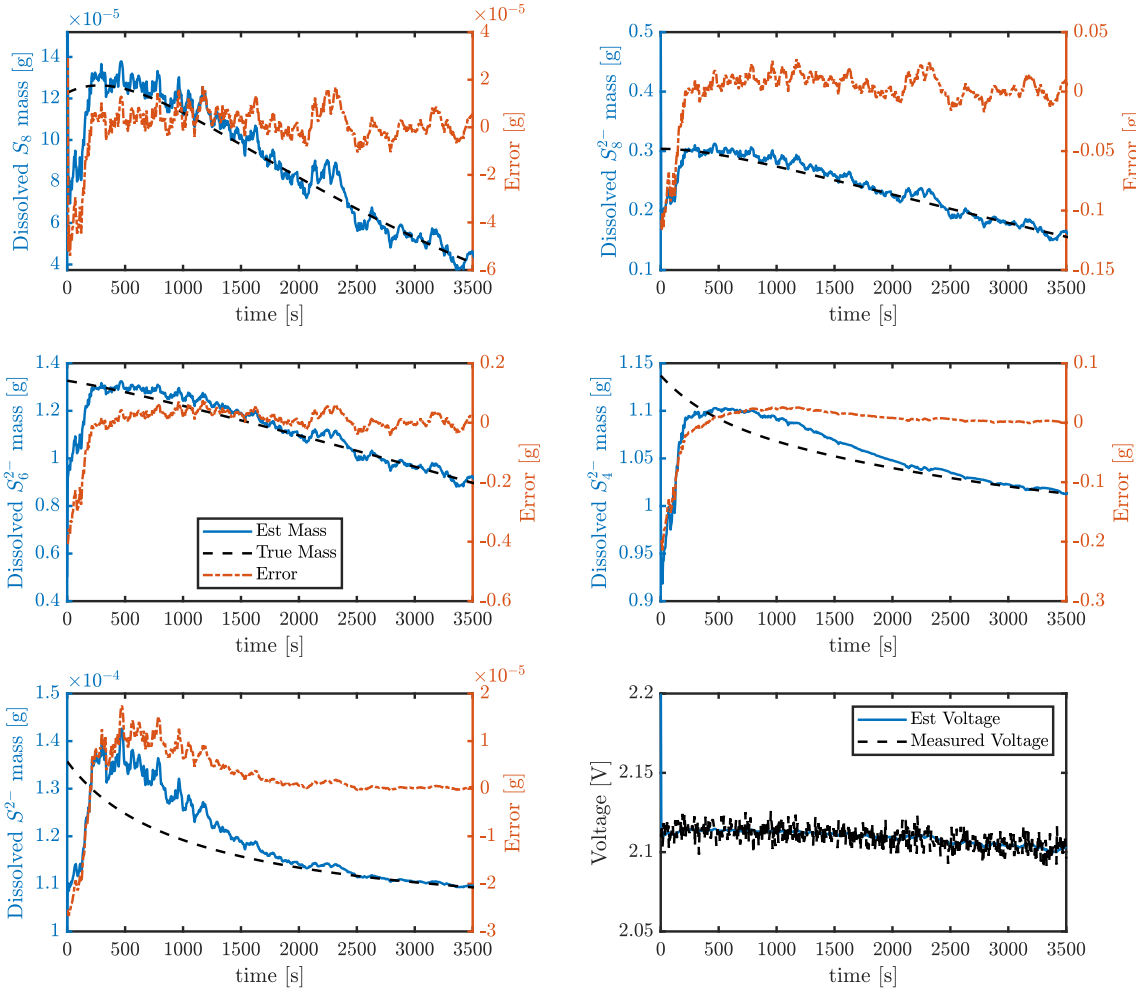

Figure 4.7: Low plateau state estimation with a constant discharge current for the reduced-order model

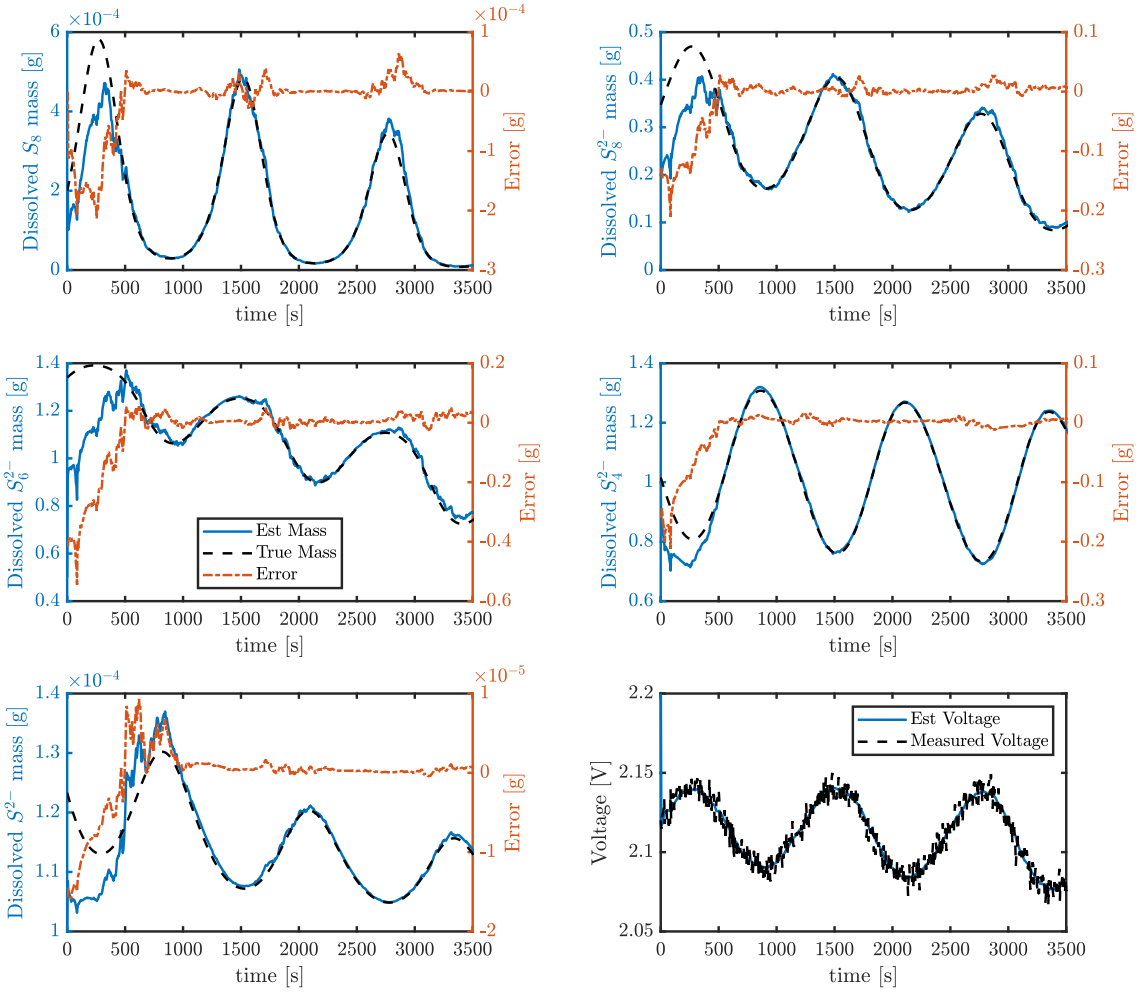

Figure 4.8: Low plateau state estimation with a constant plus sinusoidal discharge current for the reduced-order model

states (i.e. the "flatness" of the output voltage curve in the low plateau region). Significant differences between the initial state estimates and the corresponding true values take longer to diminish because of this reduced sensitivity. This slow convergence occurs even when the estimated voltage quickly converges to the measured voltage: a sign of poor observability. Intuitively, because of the poor sensitivity of the output voltage with respect to the underlying state estimates, one cannot rely on the voltage measurement error to achieve fast convergence of the state estimates.

Regardless of the above caveats, state estimation accuracy using the reduced-order model is generally attractive. Better observability and estimation accuracy is achievable in the high plateau region, compared to the low plateau region, for both the full and reduced-order estimators. Therefore, it is recommended to launch estimation in the high plateau region if possible, particularly if the total active sulfur mass is unknown. Then one can gather the estimated total active mass during the high plateau region. Once the cell voltage enters the low plateau region, a reduced-order state estimator can be used for better performance.

4.5 Conclusions

This chapter shows that it is generally possible to construct an algorithm for estimating the masses of various species in Li-S batteries. This is important because it provides a more detailed picture of the internal state of the battery compared to a more traditional "lumped" SOC estimate. The author reformulates the zero-dimensional physics-based Li-S battery DAE model into an ODE model, and

analyzes the model's local observability. Observability analysis reveals poor observability in the low plateau region, where cell voltage is less sensitive to precipitated sulfur mass. A reduced-order model is derived through mass conservation, showing attractive observability properties in both the high and low plateau regions. Simulation-based internal state estimation is performed on the physics-based Li-S model using an unscented Kalman filter. The simulation results illustrate the effectiveness of the estimator and show consistency with the fundamental discoveries of the observability analysis.

Chapter 5: Exploiting the Dependence of Battery Resistance on State of Charge for Improving State Estimation Accuracy: Theory and Li-S Application Example

5.1 Overview

This chapter examines the problem of improving state of charge (SOC) estimation accuracy for Li-S battery cells by exploiting the dependence of these cells' internal resistance on SOC[1]. Accurate SOC estimation for Li-S batteries is particularly problematic in the low plateau region, because of the very low associated sensitivity of battery voltage to SOC. The fact that small sensitivities of battery voltage to SOC can hinder accurate SOC estimation is already well-recognized in the literature, given its negative impact on established battery chemistries such as the LFP chemistry [79, 80]. The main insight behind this chapter is that this estimation accuracy challenge can be mitigated at least partially by exploiting the dependence of battery resistance on SOC for more accurate SOC estimation. In the specific case of Li-S batteries, due to the low solubility of S^{2-}, precipitation occurs inside the cell in the low plateau region. This results in a change in internal resis-

[1] The work presented in this chapter is in preparation for submission to a peer-reviewed journal.

tance as a function of SOC. This change can benefit SOC estimation, particularly when battery current is "dithered" in an attempt to increase its mean square value.

The literature presents a number of algorithms for Li-S state estimation, including SOC estimation. These algorithms can be classified based on whether they utilize equivalent circuit models (ECMs) [40, 41, 42] or machine learning methods [43] or both as foundations for estimation. While different estimation algorithms continue to be applied and developed for Li-S batteries, there still exist fundamental limitation on the best achievable accuracy with which one can estimate a battery's SOC from current-voltage measurements. These best achievable estimation error bounds are imposed by the Cramér-Rao theorem [81]. A shallow slope of a battery's open circuit voltage versus SOC ($d\ OCV/d\ SOC$) plays an undesirable role in limiting SOC estimation accuracy. This is particularly problematic for Li-S batteries during the low voltage plateau region, where the OCV curve is flat, providing a small $d\ OCV/d\ SOC$ slope. This results in poor state observability of the system, as indicated in the author's previous publication [61]. In this scenario, the changing internal resistance with SOC can play a role in improving estimation accuracy. Moreover, there exists an open opportunity to tailor the system's input current in a manner that improves this estimation accuracy.

This chapter aims to improve SOC estimation accuracy for Li-S batteries by superimposing periodic discharge current "dither signals" on top of the main discharge current signal. The underlying reasons for the improvement in the theoretical estimation error bounds include: (i) the fact that the derivative of the internal resistance of Li-S batteries with respect to SOC is not zero, and (ii) the fact that the

additional periodic "dither" current furnishes a Fisher information matrix with a bigger determinant, providing tighter Cramér-Rao bounds on estimation accuracy. In the presence of voltage measurement noise, estimating state of charge is essentially an exercise in estimating the battery's initial SOC, and then propagating an estimate of battery SOC to any future moment in time using the current measurements, assuming a reliable battery model. This work focuses on the estimation error bounds for the initial SOC for Li-S batteries. The contributions of this analysis are to provide a way to furnish tighter estimation error bounds during the flat region of an OCV curve by dithering the external current, given a nonzero internal resistance slope.

In the remainder of this chapter, the author employs Fisher information analysis based on a first-order equivalent circuit model. This analysis quantifies the degree to which SOC estimation accuracy benefits from the dependence of battery resistance on SOC. Moreover, this analysis quantifies the improvement in SOC estimation accuracy that results from applying a sinusoidal current dither profile. Prototype Li-S coin cells are fabricated and tested in the laboratory in order to illustrate these ideas experimentally. The resulting experimental data sets are analyzed statistically, and used to parameterize an equivalent circuit model. This model is utilized in Monte Carlo simulation studies to support the above theoretical insights. Monte Carlo simulation results show that the exploitation of dithering plus the dependence of battery resistance on SOC results in a 50% reduction in SOC estimation errors at the point of lowest OCV-SOC slope.

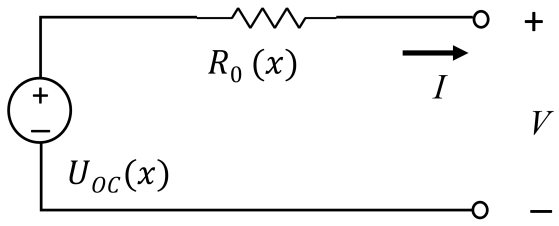

Figure 5.1: First-order ECM structure

5.2 Fisher Information Analysis Based on First-order ECM

This section presents a theoretical estimation accuracy study based on a simple first-order equivalent circuit model. Given this model's structure, one can derive local analytical estimation error bounds using Fisher information analysis. This study is not exclusively constructed for Li-S batteries. In fact, it can be employed to different types of batteries, hence the lessons learned here are widely applicable.

5.2.1 ECM Structure and Linearization

The author considers a simple nonlinear first-order equivalent circuit battery model for simplicity, with the understanding that the model can be extended to higher orders if necessary. The model consists of an open circuit voltage U_{oc} and an internal resistance R_0, as shown in Fig. 5.1. Both U_{oc} and R_0 can be represented as functions of x, which is the SOC of the battery. The state space model is as follows:

State Equation:

$$\dot{x} = -\frac{1}{Q}u \tag{5.1}$$

Output Equation:

$$V = U_{oc}(x) - R_0(x)u \tag{5.2}$$

where Q is the battery's charge capacity in Coulombs. The input and output variables of the system are the external current $u(t)$ (positive during discharge) and the voltage across the battery $V(t)$. The only state variable is the SOC of the battery, namely, x.

This chapter uses $(\bar{x},\bar{V})$ to represent a specific reference equilibrium point around which the initial battery SOC is to be estimated. The underlying assumption is that deviations in SOC from this equilibrium are small enough to justify model linearization, at least for the purpose of local Fisher information-based estimation error analysis. Linearizing the model around the equilibrium point $\bar{x}$ to get:

$$V = \bar{V} + \gamma(x - \bar{x}) - \beta(x - \bar{x})u \tag{5.3}$$

where

$$\gamma = \frac{\partial U_{oc}}{\partial x}|_{\bar{x}} \tag{5.4}$$

$$\beta = \frac{\partial R_0}{\partial x}|_{\bar{x}} \tag{5.5}$$

Suppose that the output voltage of the battery is measured at discrete moments in time with a sampling period δt. Moreover, suppose that the resulting discrete-time output measurement is afflicted with measurement noise, as presented

in Eqn. 5.6.

$$V_k = (\bar{V} - \gamma\bar{x} + \beta\bar{x}u_k) + \gamma x_k - \beta x_k u_k + e_k \tag{5.6}$$

where

$$x_k = x_0 - \frac{1}{Q}\sum_{i=1}^{k} u_i \delta t \tag{5.7}$$

$$k = 1, 2, 3, ..., N$$

There are N time steps in the above equations, with k as the sampling index. The symbol x_0 denotes the initial SOC of the battery, and e_k accounts for the observation error or measurement noise.

The above equations can be written in the standard linear regression form if one defines a new fictitious output variable, Y_k, as follows:

$$Y_k = (\gamma - \beta u_k)x_0 + e_k \tag{5.8}$$

Given this definition of the regression equation's output, one can combine Eqn. 5.7 and Eqn. 5.6 and rearrange to get Eqn. 5.9.

$$Y_k = V_k - \bar{V} + (\gamma - \beta u_k)(\bar{x} + \frac{1}{Q}\sum_{i=1}^{k} u_i \delta t) \tag{5.9}$$

The signal Y_k becomes the new output of the linear system. Instead of being measured directly, it can be calculated knowing: (i) the input measurement at each instant of time and (ii) the reference equilibrium battery SOC. This work aims

to locate the estimate of x_0 that best fits the corresponding system model, from a large set of observations. Furthermore, the author examines the estimation accuracy bounds given different input profiles.

5.2.2 Fisher Information Analysis

Fisher information analysis is a tool that makes it possible to quantify the amount of information a given experiment generates for estimating an unknown parameter. Fisher information analysis is particularly well-suited for assessing local parameter estimation accuracy in the neighborhood of a reference parameter value - in this case, the reference equilibrium SOC value $\hat{x}$. The Fisher information matrix is mathematically guaranteed to be positive semi-definite. If it is positive definite, the inverse of the Fisher information matrix provides the best achievable local estimation error covariance for the unknown parameter(s) [74]. The mathematical definitions of the Fisher information matrix $\boldsymbol{F}$ and Cramér-Rao lower bound(s) $cov(\boldsymbol{\theta})$ can be represented using the following equations [74]:

$$\boldsymbol{F} = E\{(\frac{\partial}{\partial \boldsymbol{\theta}} ln\ p(\boldsymbol{Y}|\boldsymbol{\theta}))(\frac{\partial}{\partial \boldsymbol{\theta}} ln\ p(\boldsymbol{Y}|\boldsymbol{\theta}))^T\} \tag{5.10}$$

$$cov(\boldsymbol{\theta}) \geq \boldsymbol{F}^{-1} \tag{5.11}$$

where $\mathbf{Y}$ is the observable output with embedded measurement noise, $\boldsymbol{\theta}$ is the unknown parameter vector to be estimated, and $p(\mathbf{Y}|\boldsymbol{\theta})$ is the likelihood function for

$\mathbf{Y}$ conditioned on the value of $\boldsymbol{\theta}$. The optimal value of the parameter $\boldsymbol{\theta}$ is the value that maximizes the likelihood function $p(\mathbf{Y}|\boldsymbol{\theta})$.

A parameter estimation problem is linear in the unknown parameters if the relationship between the output measurement vector $\boldsymbol{Y}$, the unknown parameter vector $\boldsymbol{\theta}$, and the measurement noise vector $\boldsymbol{e}$ is given by:

$$\boldsymbol{Y} = \boldsymbol{S^T\theta} + \boldsymbol{e} \tag{5.12}$$

where $\boldsymbol{S}$ is a so-called sensitivity matrix. Moreover, if one makes the assumption that the measurement noise is zero-mean, Gaussian, and independent, identically distributed (iid), then one can write the probability density function of $\boldsymbol{Y}$ or $\boldsymbol{e}$ as shown in Eqn. 5.13.

$$p(\boldsymbol{Y}|\boldsymbol{\theta}) = p(\boldsymbol{e}|\boldsymbol{\theta}) = \frac{1}{\sqrt{(2\pi)^N\ \sigma^2}} exp(-\frac{1}{2\sigma^2}\ \boldsymbol{e}^T\boldsymbol{e}) \tag{5.13}$$

The above definitions lead to the following log-likelihood function:

$$\ln\ p(\boldsymbol{Y}|\boldsymbol{\theta}) = -\frac{1}{2}\ln\ ((2\pi)^N\sigma^2) - \frac{1}{2\sigma^2}\boldsymbol{e}^T\boldsymbol{e} \tag{5.14}$$

Taking the partial derivative of this function with respect to $\boldsymbol{\theta}$ gives:

$$\frac{\partial}{\partial\boldsymbol{\theta}}\ln\ p(\boldsymbol{Y}|\boldsymbol{\theta}) = \frac{1}{\sigma^2}\boldsymbol{S}\boldsymbol{e} \tag{5.15}$$

Finally, plugging Eqn. 5.15 into Eqn. 5.10, yields the following expression for the

Fisher information matrix (note that in this case, because the only parameter being estimated is SOC, the matrix is effectively a scalar):

$$\boldsymbol{F} = E\{\frac{1}{\sigma^4}\boldsymbol{S}\boldsymbol{e}\boldsymbol{e}^T\boldsymbol{S}^T\} = \frac{1}{\sigma^4}\boldsymbol{S}\ E\{\boldsymbol{e}\boldsymbol{e}^T\}\ \boldsymbol{S}^T = \frac{1}{\sigma^2}\boldsymbol{S}\boldsymbol{S}^T \tag{5.16}$$

The above formula relates the sensitivity matrix of the output to the parameters to be estimated [74, 80], and allows us to calculate the Fisher information matrix numerically. In this chapter, the to-be-identified parameter x_0 is a scalar, leading to a $1 \times N$ deterministic sensitivity matrix $\boldsymbol{S}$. By taking the partial derivative of measurement with respect to x_0, one can obtain the k^{th} element of the sensitivity matrix:

$$S_k = \frac{\partial Y_k}{\partial x_0} = \gamma - \beta u_k \tag{5.17}$$

Assume that the duration of the estimation experiment (in seconds) is represented by T. The number of time steps N is related to T by formula $T = N\delta t$, and σ_v is the standard deviation of the voltage measurement noise. One can, therefore, derive the Fisher information matrix for the first-order ECM, either exactly (as a summation) or approximately (by replacing the summation with a time integral), as shown below:

$$\begin{aligned} F &= \frac{1}{\sigma_v^2\delta t}(T\gamma^2 - 2\gamma\beta\sum_{k=1}^{N} u_k\delta t + \beta^2\sum_{k=1}^{N} u_k^2\delta t) \\ &\approx \frac{1}{\sigma_v^2\delta t}(T\gamma^2 - 2\gamma\beta\int_0^T u dt + \beta^2\int_0^T u^2 dt) \end{aligned} \tag{5.18}$$

The Cramér-Rao lower bound (CRLB) for the initial state of charge estimation variance is the inverse of the Fisher information, representing the bound achieved by the best-possible unbiased estimator. A tighter error bound for x_0 indicates that it is easier to locate the true initial state of charge accurately.

5.2.3 Insights from Fisher Information Analysis

The above Fisher analysis provides three main insights into SOC estimation accuracy.

First, Fisher information is essentially a signal-to-noise ratio, reflecting the degree to which one is able to gather useful information about a given parameter versus the noise affecting this parameter's estimation accuracy. Therefore, it makes sense for the above expression for Fisher information to decrease with σ_v^2, the output voltage measurement noise variance. Intuitively, the larger this measurement noise variance, the worse the parameter estimation variance. Moreover, it makes sense for the above expression for Fisher information to depend on the ratio of the total experiment time, T, to the sampling period, δt. This ratio equals the number of samples taken during a given experiment. Intuitively, it makes sense that the larger this number of samples, the more accurately one can estimate battery SOC.

Second, the slope of the open circuit voltage and internal resistance versus SOC, denoted by γ and β, affect the ability to estimate x_0. One can observe from Eqn. 5.18 that a larger γ benefits estimation accuracy due to the increased value of the first term $T\gamma^2$. If the open circuit voltage versus state of charge curve has

a relatively flat region, i.e., a small γ, SOC estimation accuracy becomes poor. Furthermore, a nearly constant internal resistance with respect to SOC (i.e., $\beta = 0$) causes the second and third term of Eqn. 5.18 to be close to zero, thereby causing SOC estimation accuracy to depend almost entirely on γ, the slope of the battery's OCV-SOC curve. However, when the internal resistance changes with respect to SOC, two new effects take hold, both of them affecting SOC estimation accuracy:

- The first effect depends on the product of γ and β, as well as the sign of the battery current. To understand the impact of this term, consider the problem of estimating battery SOC during constant-current charge or discharge. In such a scenario, battery terminal voltage will change with time, both due to the slope of the OCV-SOC curve and due to the changing battery resistance. If these two effects cause opposite changes in battery terminal voltage, the end result will be a worsening of SOC estimation accuracy. In contrast, if these two effects cause same-sign changes in battery voltage, the end result will be an improvement in SOC estimation accuracy. Thus, the term in Eqn. 5.18 that contains the product $\gamma\beta$ causes SOC estimation accuracy to depend on the direction of battery current, and to be different during charge versus discharge.

- The second effect depends on the square of the slope, β, of battery resistance with respect to SOC. This term causes battery estimation accuracy to improve as this slope increases. In fact, the main goal of this chapter is to show that this term allows for more accuracy SOC estimation, even for batteries where

the slope of the OCV-SOC curve, γ, is very shallow.

The final insight is that when battery SOC estimation accuracy is poor, dithering the input current signal to increase its mean square value helps improve this accuracy by amplifying the third term of Eqn. 5.18. Intuitively, this insight can be rephrased as follows: *the use of input current dithering for online battery resistance estimation helps improve SOC estimation accuracy in batteries where internal resistance is a strong function of SOC.* To see this insight mathematically, consider two different battery charge or discharge scenarios, one where the battery input current is some constant u_o, and one where a sinusoidal dither signal is added to u_o:

$$u_1 = u_0 \tag{5.19}$$

$$u_2 = u_0 + Asin(\omega t) \tag{5.20}$$

Using the two current profiles from Eqn. 5.18, one can obtain the following expressions for Fisher information:

$$F_1 = \frac{1}{\sigma_v^2 \delta t}(T\gamma^2 - 2\gamma\beta T u_0 + \beta^2 T u_0^2) \tag{5.21}$$

$$F_2 = F_1 + \frac{2A\beta(u_0\beta - \gamma)}{\sigma_v^2 \delta t}\int_0^T sin(\omega t)dt + \frac{A^2\beta^2}{\sigma_v^2 \delta t}\int_0^T sin^2(\omega t)dt \tag{5.22}$$

When the total time duration T is chosen to be an integer multiple of the period of the sinusoidal dither current, the integral of $sin(\omega t)$ equals zero. Hence, one

can have $F_2 > F_1$, leading to the conclusion that a sinusoidally-dithered discharge current trajectory provides more "information" and tightens the estimation error bounds.

5.3 Li-S Battery ECM Parameterization

This section introduces Li-S battery parameterization experiments performed by the author in order to obtain a first-order equivalent circuit battery model. Both C-rate and aging are factors that can potentially influence the internal resistance and open circuit voltage curves for Li-S cells. From the literature [37], the sensitivity of the Li-S ECM parameters to C-rate is particularly high above 1C. However, higher current operation causes Li-S battery performance to deteriorate significantly. In this chapter, the test plan includes a relatively low discharge current range reflecting health-conscious Li-S battery use. Each fabricated battery cell is cycles fewer than 20 times, such that the resulting parameter estimates reflect fresh rather than aged cells. Given these experiment design choices, the author neglects the dependence of battery parameters on C-rate and age in the analysis below.

5.3.1 Experiment Setup

The author fabricates 2016-type prototype Li-S coin cells in the laboratory using the recipe in [50]. The cathode material of the coin cells consists of 56 wt% sulfur powder, 24 wt% ketjenblack, 10 wt% carbon nanofiber as s conductive material, and 10 wt% polyvinylidene fluoride dissolved in NMP as a binder. Carbon-coated alu-

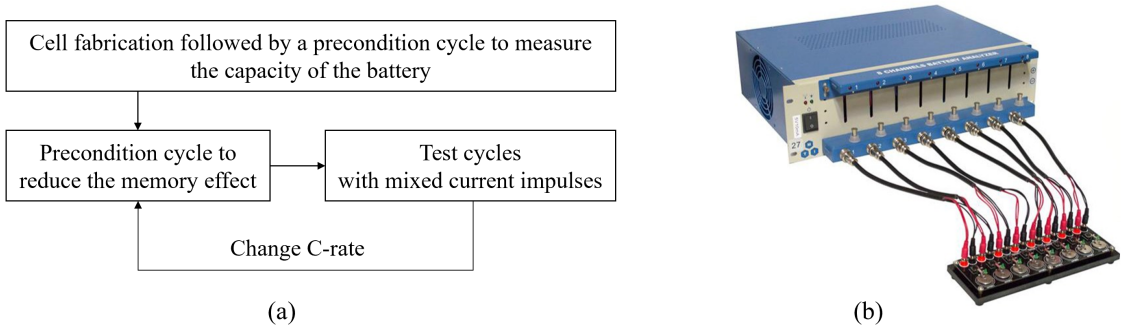

Figure 5.2: (a) Test procedure for the characterization of the first-order ECM (b) Coin cell testing equipment

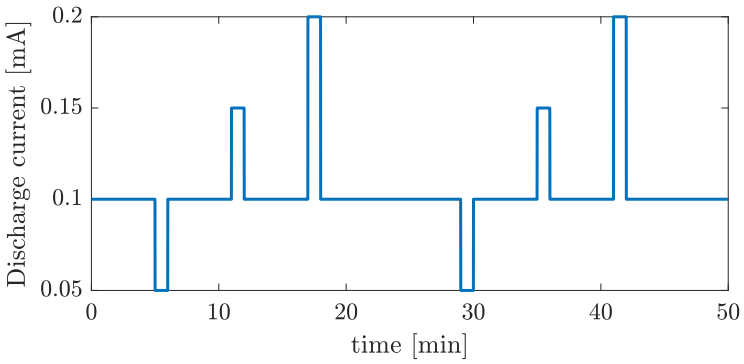

Figure 5.3: An example of the mixed-pulse discharge current profile

minum foil of 18 μm thickness is used as the cathode collector. A plain lithium chip with 16mm diameter $\times$ 0.6mm thickness is used as the anode. The separator material is cut into 19 mm diameter chips from a single porous polypropylene membrane. The electrolyte used is 1M LiTFSI and 0.3M lithium nitrate in the DOL/DME mixture (DOL/DME = 1:1, v/v).

Cycling the prototype cells provides the experimental data to parameterize the equivalent circuit model. The author performs a set of cycling tests covering three different C-rates at room temperature, as shown in Fig. 5.2(a). The discharge C-rates include $\frac{1}{10}$C, $\frac{1}{5}$C, and $\frac{1}{2}$C. For each C-rate test cycle, the author begins with a precondition cycle to eliminate history effects. The precondition cycle charges

the cell through CC-CV (constant current constant voltage) of 0.1mA (with a total capacity about 1.5mAh) to 3V, followed by a constant 0.1mA current discharge. Then, a constant current discharge cycle is conducted with mixed current pulses to obtain the internal resistance along the discharge process. The mixed current pulses are imposed with the width of one minute, the interval of five minutes, and the magnitudes of -0.05, 0.05, and 0.1 mA, as shown in Fig. 5.3. The charging phase of the test cycle is the same as the one of the precondition cycle. The cells are tested using an 8-channel battery analyzer by MTI (0.005-1mA, up to 5V), as shown in Fig. 5.2(b).

5.3.2 Experimentally Parameterized ECM

Six coin cells are tested using the above procedure. From the experimental data, one can observe variations of the internal resistance curves between different cells. The obtained open circuit voltage curves exhibit consistent behavior. This chapter focuses on the improvement in estimation accuracy resulting from the changing internal resistance. The author assumes $R_0(x)$ as a fourth-order polynomial of the battery's SOC, as shown in Eqn. 5.23. Experimental data of the internal resistance for all testing cycles of the six tested cells are used to fit the polynomial. Fig. 5.4 plots the fitted curve and the measured internal resistance. Table 5.1 summarizes the estimated coefficients of the polynomial and their 95% confidence intervals. Note that the confidence intervals will be potentially smaller in commercially fabricated

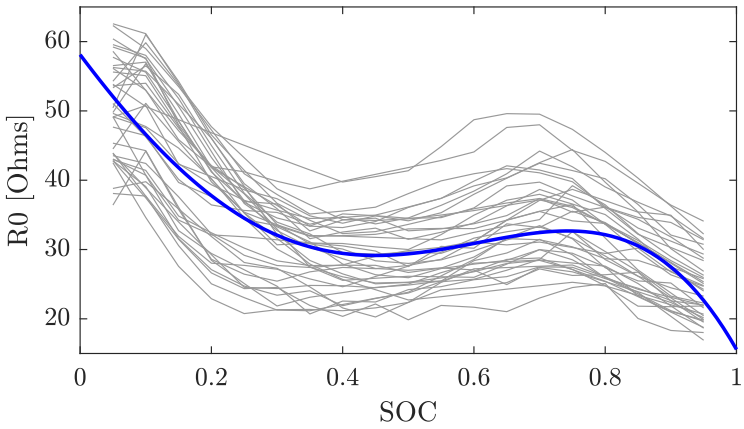

Figure 5.4: The fitted internal resistance R_0 curve (blue line) and the measured curves for all testing cycles (grey lines)

Coeff	**Estimates**	**LCL**	**UCL**
p_1	-200.44	-315.92	-84.96
p_2	193.84	-38.69	426.38
p_3	89.88	-66.75	246.51
p_4	-125.80	-165.72	-85.89
p_5	58.11	55.06	61.16

Table 5.1: Estimated coefficients of the polynomial and their 95% upper confidence limits (UCL) and lower confidence limits (LCL)

batteries with industrial-grade quality control.

$$R_0(x) = p_1x^4 + p_2x^3 + p_3x^2 + p_4x + p_5 \tag{5.23}$$

For the open circuit voltage, the author obtains an averaged OCV curve using the measured experimental data of all the cycles. Fig. 5.5 illustrates the R_0 and OCV curves used in the following simulation study to verify the estimation accuracy improvement.

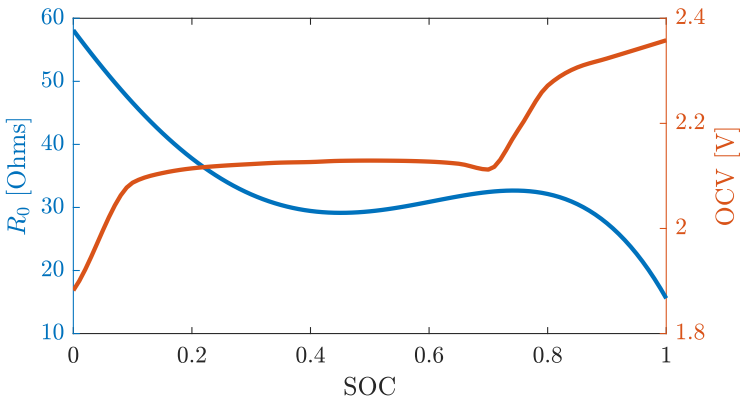

Figure 5.5: Obtained R_0 and OCV curves from the six tested coin cells

5.4 Monte Carlo Simulation Study

This section presents a simulation study based on the linearized Li-S equivalent circuit model, performing least squares regression to find the best estimate of the to-be-identified parameter, namely, the initial state of charge x_0. The least-squares method estimates parameters by minimizing the squared discrepancies between observed data and the expected values. In our case, the goal is to identify the best-fit initial state of charge $\hat{x}_0$ which minimizes

$$\min_{\hat{x}_0} J = \sum_{k=1}^{N} (\hat{Y}_k - Y_k) \tag{5.24}$$

subject to:

$$\hat{Y}_k = S_k^T \ \hat{x}_0 \tag{5.25}$$

The optimal estimate of the parameter vector $\hat{x}_0$ can be obtained by the least squares linear regression equation as shown in Eqn. 5.26. This is also the estimate

that maximize the log-likelihood function in the Fisher information analysis.

$$\hat{x}_0 = (\boldsymbol{S}^T \boldsymbol{S})^{-1} \boldsymbol{S}^T \boldsymbol{Y} \tag{5.26}$$

where $\boldsymbol{Y} = [Y_1 \;\; Y_2 \;\; ... \;\; Y_k \;\; ... \;\; Y_N]^T$, and Y_k is expressed by Eqn. 5.9.

The above linear regression can be repeated for different realizations of the voltage measurement noise process, producing different maximum-likelihood estimates of the parameter $\hat{x}_0$. The author simulates the model 2000 times with random sampling of the noise signal. To obtain the best-achievable estimation accuracy and compare with the Cramér-Rao lower bounds, this work chooses the initial condition of the system to be the equilibrium point, meaning $\overline{x} = x_0$. The author chooses two different initial SOC locations ($x_0 = 0.5, 0.8$) to perform the Monte Carlo simulation, using parameters listed in Table 5.2. For each location, the differences of estimation accuracy are compared between a constant and a sinusoidally dithered input current.

Table 5.3 lists the mean values and standard deviations of the estimated x_0 from the simulation results for both cases. To better visualize the estimation accuracy, the author plots Figure 5.6 to illustrate the estimated initial SOC $\hat{x}_0$ in the 2000 repeated simulation.

The main observations from simulation results are as follows. Firstly, for every combination of input current and initial SOC, the mean value of the estimated parameter $\hat{x}_0$ coincides with the true parameter value x_0. This is due to the fact that the noise signal is zero-mean and the author deliberately chose the initial condition

Notation	Value	Unit
u_0	0.5	mA
A	1	mA
ω	0.5	rad/s
δt	0.1	s
T	125	s
N	1250	-
σ_v	0.01	V
Q	1.5	mAh

Table 5.2: Parameters used in the Monte Carlo simulation

of the system to be the equilibrium point. Together, these assumptions/conditions lead to unbiased parameter estimation, in the sense that the mean of the Monte Carlo points approaches the true parameter estimates. Secondly, the standard deviations of the estimates $\sigma_{\hat{x}_0}$ are consistent with the error bounds calculated from the previous Fisher information analysis. In other words, the probabilistic distributions of the estimated parameters are matching nicely with the theoretical Cramér-Rao bounds. Thirdly, in the scenario of 0.5 initial SOC, the standard deviation of the estimated parameter shrinks 50% when applying a sinusoidal current. This scenario provides the best estimation improvement due to the flatness of the OCV curve, i.e., a small value of γ. The third term of Eqn. 5.18 dominates, and a sinusoidal input increases this term, leading to a better estimation accuracy. Finally, in the scenario of 0.8 initial SOC, applying a periodic current does not provide significant benefit. The observability of this point is good enough that the room for improvement is limited. These observations validate the author's assumption that applying

Initial SOC	$x_0 = 0.5$		$x_0 = 0.8$	
Input	u_1	u_2	u_1	u_2
σ_{x_0}	4.6507E-2	2.2722E-2	5.3059E-4	5.3405E-4
Mean $\hat{x}_0$	0.4992	0.4998	0.8001	0.8002
$\sigma_{\hat{x}_0}$	4.6256E-2	2.2608E-2	5.1679E-4	5.2070E-4

Table 5.3: Parameters used in the Monte Carlo simulation

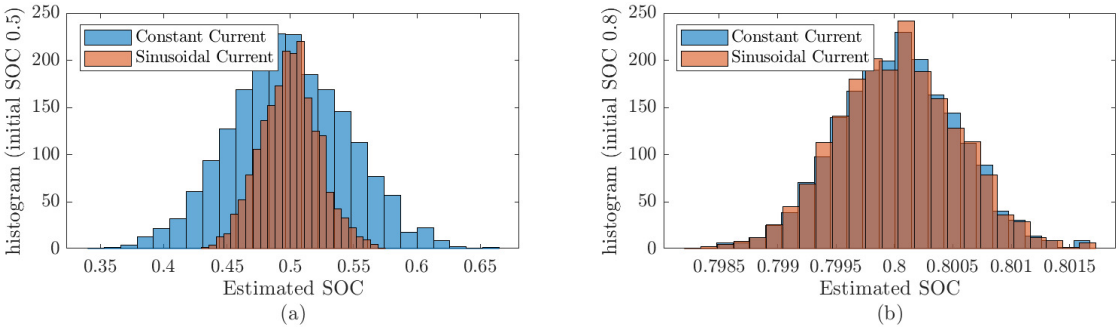

Figure 5.6: Histogram of the estimated initial SOC $\hat{x}_0$ for (a) $x_0 = 0.5$ and (b) $x_0 = 0.8$

a sinusoidal discharge current improves theoretical estimation error bounds for Li-S battery SOC. Such improvement is more obvious at the point of poor observability of the system, which is valuable due to the need for improvement at such a point.

5.5 Conclusions

This work proposes and validates the hypothesis that applying a periodic discharge current profile improves the best theoretically-achievable battery SOC estimation accuracy, compared to a constant current, provided that the internal resistance is changing with respect to SOC. Such improvement can be particularly important for batteries with limited SOC observability due to the flatness of their OCV-SOC curves. Fisher information analysis applied to a linearized equivalent

circuit model proves the improvement in the estimation accuracy of the battery's initial charge. The author performs Monte Carlo simulation studies and conduct repeated tests to validate this theoretical result for an equivalent circuit Li-S battery model. This research provides the important insight that at points where the OCV-SOC cure of a given battery is shallow, one can change the dither the battery input current periodically to improve estimation accuracy.

Chapter 6: Lithium-Sulfur Battery Discharge Optimization using a Thermally-Coupled Equivalent Circuit Mode

6.1 Overview

After the examining the problem of parameterization and estimation of Li-S battery management system, this chapter explores the control side by optimizing the discharge trajectory of a Li-S battery to maximize the total energy released over a fixed time horizon[1]. Optimal control can play an important role in improving the performance of Li-S batteries, in parallel with innovation in materials/chemistries. Optimal control tools have already been used to improve the overall energy densities of lithium-ion batteries [48, 49]. However, the lessons learned from this previous literature may not be directly translatable to the Li-S chemistry due to fundamental differences in the underlying reactions and dynamics. The problem of optimizing the input trajectories of Li-S batteries therefore warrants independent investigation: a topic that, to the the best of the author's knowledge, remains unexplored in the literature.

Unlike traditional lithium-ion batteries, where lithium intercalates in/out of

[1]The work presented in this chapter has been accepted for publication in the peer-reviewed proceedings of the 2021 Modeling, Estimation, and Control Conference. The final conference manuscript is currently in preparation

the electrodes, Li-S batteries are based on conversion reactions. The multi-reaction chain and precipitation inside the battery create complexity, nonlinearity, and non-monotonicity of both open circuit voltage and internal resistance profiles with respect to state of charge. Such features offer a potential to develop an optimal control strategy that maximizes the total energy release by strategically discharging the battery faster when its open-circuit voltage is high and/or its internal resistance is low. The optimal discharge trajectory for an electrochemical battery changes based on the battery's precise chemistry. This chapter focuses on a traditional Li-S battery chemistry utilizing a lithium metal negative electrode, liquid electrolyte, and carbon/sulfur composite positive electrode. Fig. 6.1 plots the open circuit voltage (OCV) and internal resistance profiles of a Li-S battery at 20°C, experimentally measured by [37]. The OCV curve consists of a high plateau, a low plateau, and a dipping point between these two regions. In the high plateau region, the active material, S_8, in the cathode accepts electrons to produce the polysulfide, S_x^{2-} (x can be 8, 6, 4). Further polysulfide reduction takes place in the lower voltage plateau region, furnishing S_2^{2-} and S^{2-} ions [20]. Due to the low solubility of S^{2-}, there exists precipitation inside the cell, generating the dipping point in the OCV curve. In parallel, lithium is oxidized in the anode to furnish lithium ions.

Many factors affect the characteristics of the OCV/R_0 curves of Li-S batteries significantly (where R_0 is equivalent series resistance). State of charge and temperature are two of the most important factors:

- Fig. 6.1 indicates that open circuit voltage and internal resistance are sensitive

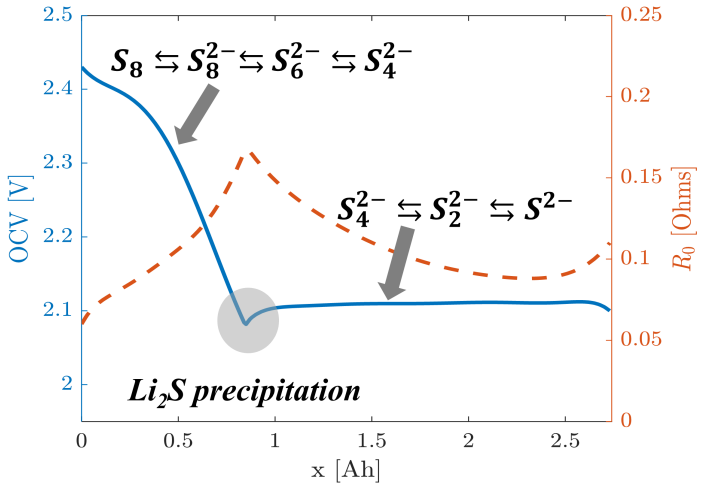

Figure 6.1: The OCV and internal resistance profiles of a Li-S battery at 20°C

to state of charge. Experiments show that the electrolyte conductivity of Li–S batteries depends on the concentrations of both lithium salt and polysulfides [45, 46]. At high concentrations, increased ionic interactions reduce electrolyte conductivity. During the high plateau region, dissolved polysulfide concentration accumulates to the maximum point, increasing viscosity and causing electrolyte resistance to grow [19]. Precipitation then decreases electrolyte viscosity, reducing internal resistance. The rebound of the R_0 curve during the second half of the low plateau can be potentially explained by the fact that the precipitate covers the interfacial area, blocking the active reactants.

- The internal resistance and the open circuit voltage of a Li-S battery demonstrate strong sensitivity to temperature, shown by experimental measurements [37, 47]. The temperature term shows up directly in the well-known Nernst equation and Butler-Volmer equation, influencing the open circuit voltage. At the same time, diffusion and reaction rates are positively related with temperature, as increased

internal energies of the ions speed the movements and reactions. A colder temperature induces higher internal resistance due to slower ion charge transfer in the electrolyte, as shown in Fig. 6.3(b).

To optimize Li-S battery discharge, one needs an effective, computationally-efficient battery model. Ideally, such a model should account for the high sensitivity of both OCV and R_0 to cell temperatures. Electrochemical Li-S models are well developed in the literature [12, 13, 14, 15, 16, 17]. However, the computational complexity of these models does not always lend itself to trajectory optimization. Thermally-coupled equivalent-circuit models (ECMs), in contrast, provide both computational tractability without compromising one's ability to capture the dependence of OCV and R_0 on cell temperatures [34, 35, 36, 37]. These models are typically parameterized using laboratory tests such as the Galvanostatic Intermittent Titration technique (GITT) [36], Hybrid Pulse Power Characterization (HPPC) [39], or a mixed charge/discharge impulse test [37].

In this chapter, the author utilizes a coupled thermal/electrical equivalent circuit model, based on the existing literature, that captures the dependence of battery resistance on both temperature and SOC. The model's parameters are fitted to experimental data published by [37]. This model is then used to construct an optimal discharge strategy that maximizes total energy release over a fixed time horizon. The resulting discharge current profile provides a power burst at the beginning of the discharge duration. This implies that Li-S batteries are well-suited for applications with a high initial power demand followed by a low power maintenance

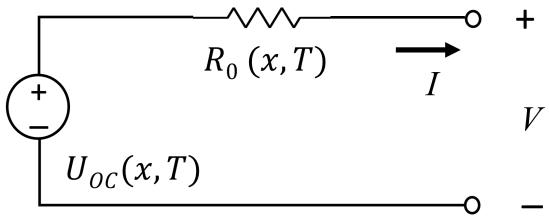

Figure 6.2: Thermally-coupled first-order ECM structure for Li-S batteries

requirement. One such application is electrified flight, where the demand power for takeoff is much larger than for en-route operation.

The remainder of this chapter describes the thermally-coupled ECM structure, parameterizes the model based on data from the literature, presents the optimization problem formulation, and discusses the optimization results, focusing on how it differs from the constant-current and constant-power benchmarks.

6.2 Thermally-Coupled ECM Structure

The Li-S battery model used in obtaining the desirable optimal discharge strategy is introduced here. The author considers a thermally-coupled ECM to simulate the dynamics of the charge and temperature of the Li-S battery. From the equivalent circuit perspective, a first-order ECM is chosen for simplicity with the understanding that the model can be extended to higher order if necessary. The model includes an open circuit voltage U_{oc} and an internal resistance R_0, as shown in Fig. 6.2. These two variables are essential to predict Li-S battery performance. The literature shows that the parameters of Li-S battery ECMs typically change with SOC, C-rate, and temperature [36]. The sensitivity of model parameters to C-rate is particularly high above 1C [37]. However, higher current operation causes

Li-S battery performance to deteriorate significantly. With this in mind, this work assumes a relatively low discharge C-rate. Hence, current is not considered as a factor affecting the internal resistance and open circuit voltage profiles. These two profiles are represented as functions of the charge stored inside the battery and the cell temperature. In applications where higher C-rates are required, the models used in this chapter can be extended to incorporate the dependence of battery resistance and open-circuit voltage on C-rate.

From the thermal perspective, this work assumes that the battery temperature is spatially uniform, such that convection heat transfer with the ambient environment is slow compared to conduction heat transfer within the battery cell. In this way, the cell temperature dynamics can be represented by one state variable. Combining the ECM and the thermal effect, the proposed state space model is as follows. State Equations:

$$\dot{x} = \frac{I}{3600} \tag{6.1}$$

$$\dot{T} = \frac{1}{mC_p}[-hA(T - T_{amb}) + P_{rev} + P_{irrev}] \tag{6.2}$$

where

$$P_{rev} = IT\frac{\partial U_{oc}(x,T)}{\partial T} \tag{6.3}$$

$$P_{irrev} = I^2 R_0(x,T) \tag{6.4}$$

Output Equation:

$$V = U_{oc}(x, T) - IR_0(x, T) \tag{6.5}$$

This model has two state variables, namely, the total charge transferred out of the battery x in Ah, and the battery temperature T in Celsius. The input of the system is current I (positive during discharge), and the output is the cell voltage V. The parameters m and C_p represent the mass and the effective specific heat capacity of the Li-S battery. The parameter h is the convection heat transfer coefficient, and A is the surface area of the battery. The open circuit voltage and internal resistance are represented, respectively, by two nonlinear functions, U_{oc} and R_0, of the state variables x and T.

The heat balance includes three power terms in Eqn. 6.2. The first term represents convection between the battery and the ambient temperature T_{amb}. The second term P_{rev} is the reversible heat generated due to "entropy of reaction" effect [82]. The third term P_{irrev} denotes heat dissipation due to internal resistance, always contributing to temperature increase.

6.3 Model Parameterization

Table 6.1 lists the values of the constant parameters in the above thermally-coupled ECM model, obtained from [83].

In addition to the above constants, parameterizing the ECM model involves determining the functions $U_{oc}(x, T)$ and $R_0(x, T)$. Propp *et al.* developed and parameterized a multi-temperature state-dependent ECM using experimental data

Notations	Values	Units
m	129	g
C_p	2	J/(gK)
hA	0.2	W/K
T_{amb}	20	Celsius

Table 6.1: Heat transfer relevant parameters

corresponding to a mixture of current pulses of different magnitudes at different battery operating temperatures [37]. They used two 10th-order polynomials (one for the high plateau region and the other for the low plateau region) to represent each element in the ECM (i.e., the open circuit voltage, the internal resistance, and an RC pair). In this chapter, the author extracts the experimental data representing open circuit voltage and internal resistance from the work by Propp *et al.* [37]. Then continuous and differentiable functions are found to fit these data sets for the whole discharge duration, instead of separating it into two portions. This simplifies the subsequent optimization of the battery discharge trajectory by avoiding the use of a discontinuous discharge model. The fitting functions used in this work are listed below.

Internal resistance function:

$$R_0(x,T) = p_3(T)x^3 + p_2(T)x^2 + p_1(T)x + p_0(T) \tag{6.6}$$

where

$$p_i(T) = a_{2i}T^2 + a_{1i}T + a_{0i} \tag{6.7}$$

$$i = 3, 2, 1, 0 \tag{6.8}$$

Open circuit voltage function:

$$U_{oc}(x, T) = \frac{s_1(T)}{1 + exp(s_2(T)x + s_3(T))} + s_4(T) \tag{6.9}$$

where

$$s_i(T) = b_{2i}T^2 + b_{1i}T + b_{0i} \tag{6.10}$$

$$i = 3, 2, 1, 0 \tag{6.11}$$

The internal resistance function is chosen to be a third-order polynomial of the state variable x. One can increase the order of the polynomial to improve fitting accuracy at the expense of an increased number of parameters to be estimated. The open circuit voltage is chosen to be a sigmoid function. Such a function naturally provides two plateaus, which can describe the characteristics of the OCV curve except at the dipping point. All the coefficients in these two functions are represented by a quadratic function of temperature T. The coefficients a_{ni} and b_{ni} are identified using the MATLAB curve fitting toolbox implementation of least squares methods. Table 6.2 summarizes the outcome of this estimation effort.

	OCV coefficients			R_0 coefficients		
n	a_{2n}	a_{1n}	a_{0n}	b_{2n}	b_{1n}	b_{0n}
3	3.35e-5	-3.5e-3	0.097	-3e-5	3.1e-3	0.251
2	-1.93e-4	1.92e-2	-0.496	2.7e-2	-1.393	27.23
1	2.04e-4	-2.15e-2	0.590	6.3e-4	0.077	-7.435
0	7.11e-5	-5.7e-3	0.128	2.8e-5	-1.3e-3	2.122

Table 6.2: Coefficient values of the fitting functions $OCV(x,T)$ and $R_0(x,T)$

	Mean	RMSE	Error %
OCV [V]	2.1557	0.0084	0.39
R_0 [Ohms]	0.0728	0.0067	9.17

Table 6.3: Curve fitting performance

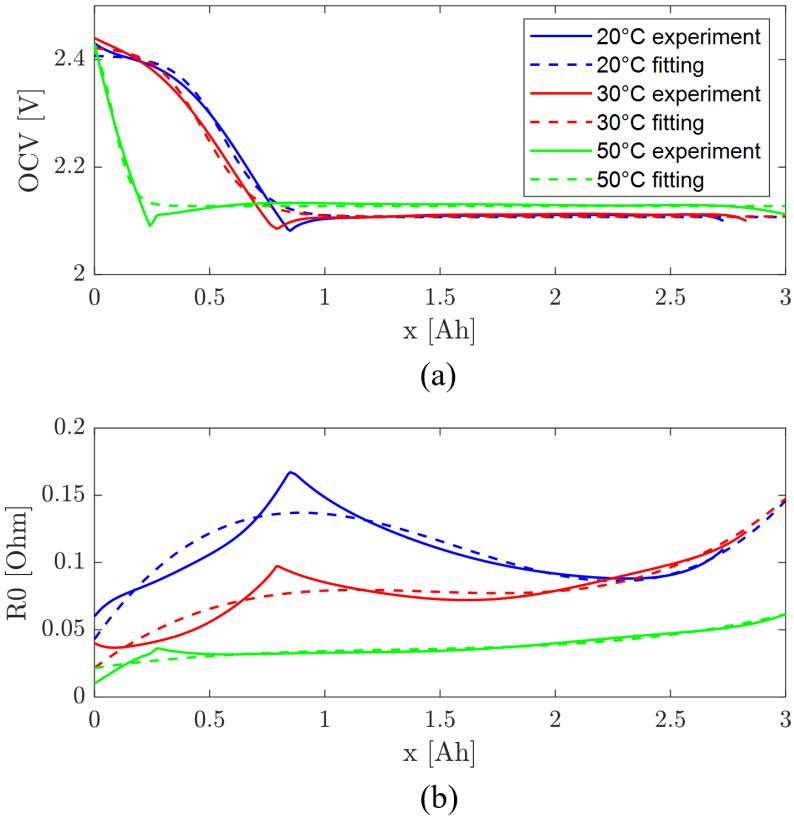

Figure 6.3: (a) Comparison between the fitting function and the experimental data of the open circuit voltage (b) Comparison between the fitting function and the experimental data of the internal resistance

To quantify the fitting performance, the root mean square errors (RMSE) and the mean values of the measurements R_0 and U_{oc} are listed in Table 6.3. The results indicate that the sigmoid function provides a good fit of the open circuit voltage with only 0.39% error. One can also observe the quality of this fit visually from Fig. 6.3(a). The low plateau voltage is almost a constant for all three temperature scenarios, and the sigmoid function easily provides this feature. Meanwhile, the fitting error of the internal resistance R_0 is 9.17%. The comparison of the experimental data and fitting functions of R_0 is shown in Fig. 6.3(b). The error percentage for internal resistance is higher as the third order polynomial lacks the ability to fit the peak of the curve accurately. However, the broad trend that cell resistance increases, then decreases, then finally increases again with state of charge is captured by the curve fit. Knowing the expression for OCV as a function of x and T, one can obtain P_{rev} by taking the derivative of U_{oc} with respect to T. Note that the open circuit voltage function is generated by curve fitting, instead of direct experimental measurements. This approach may introduce errors into the entropy of reaction. The goal of this chapter focuses on the optimal discharge strategy, not the analysis of irreversible heating in Li-S batteries. Hence, the author keeps this approach due to the good fitting performance of the OCV function. The following optimization problem is based on this parameterized model.

6.4 Optimization Problem Formulation

The optimization problem is formulated in this section. The optimization objective is to maximize total output energy within a predefined discharge time duration, described as the integrated output power from $t = 0$ to $t = t_{end}$.

$$\max_{I(t)} J = \int_0^{t_{end}} V(t)I(t)\ dt \tag{6.12}$$

subject to the system dynamics in Eqn. 6.1-6.5, and the following constraints:

$$0 \leq x(t) \leq x_{max} \tag{6.13}$$

$$T_{min} \leq T(t) \leq T_{max} \tag{6.14}$$

$$0 \leq I(t) \leq I_{max} \tag{6.15}$$

$$V(t) \geq V_{cutoff} \tag{6.16}$$

The total discharge time t_{end} is set to be 2 hours. The total charge extracted from the battery x cannot exceed the battery capacity x_{max}. This work adopts the Li-S battery capacity from earlier experimental work [37] as $3.02Ah$. The battery temperature T is constrained between 20°C to 50°C, the same as the experiment temperature range. The maximum discharge current is defined as 1C ($I_{max} = 3.02A$) and the cutoff voltage V_{cutoff} as $1.8V$.

By solving this optimization problem, an optimal discharge current trajectory is obtained. A simulation-based study is performed to validate the optimal current

control strategy compared with room-temperature baseline operation. The optimization problem is solved using the trapezoidal collocation method. This method works by converting a continuous-time trajectory optimization problem into a nonlinear program. This is done by using trapezoid rule for integration to obtain a discrete approximation of the system dynamics [84]. The resulting nonlinear program is solved in Matlab using the *fmincon* solver.

6.5 Simulation Results and Discussion

In this section, three simulation scenarios are presented: two baselines (namely, constant current and constant power discharge) plus the strategy obtained by solving the above optimization problem. The simulation results of these three scenarios are compared and discussed in detail.

6.5.1 Initial Conditions of the Three Simulation Studies

To extract all the possible energy out of the Li-S battery, the initial extracted charge x_0 is set to be zero for all three scenarios. For the two baseline scenarios, the initial cell temperature T_0 is defined to be the same as the ambient temperature T_{amb}. The optimal discharge scenario is examined both for a fixed initial temperature equal to T_{amb} and for the case where the initial temperature is chosen optimally. The optimal control strategy with a fixed initial temperature provides an energy release improvement purely from discharge current control. There also exists a possibility that preheating the battery to a higher temperature can decrease the in-

ternal resistance, hence reducing the irreversible energy dissipation. When the initial temperature is free, it can be simultaneously optimized together with the discharge current trajectory in the nonlinear program. The resulting output energy improvement comes from both the optimal battery preheating and the optimal discharge current trajectory. The heating energy required to increase the cell temperature initially is not considered in the optimization problem formulation. The intent is to examine the degree to which pre-heating can improve battery discharge behavior, irrespective of the energy cost associated with pre-heating. This type of analysis is useful for electrified mobility applications, where one could potentially pre-heat a battery back prior to the launch of an electric vehicle (e.g., electric airplane).

6.5.2 System Inputs of the Three Simulation Studies

For the constant current baseline, the discharge current is set to be 1/2C to fully discharge the battery. For the constant power baseline, the input of the system becomes the demand power. The variable I in the state space model Eqn. 6.1-6.5 can be derived from the demand power P_{dem}, as shown in Eqn. 6.17. The discharge capacity reaches the maximal cell capacity in two hours when the system demands a $3.023W$ power. Hence, this value is used in the constant power baseline study.

$$I = \frac{U_{oc}(x,T) - \sqrt{U_{oc}(x,T)^2 - 4R_0(x,T)P_{dem}}}{2R_0(x,T)} \tag{6.17}$$

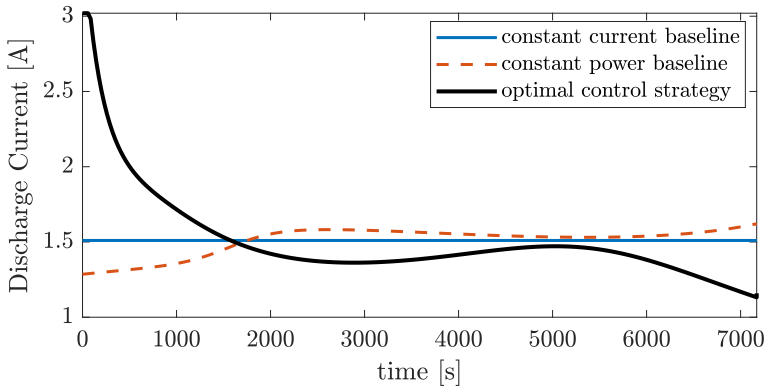

Figure 6.4: Cell current profiles of the three simulation studies

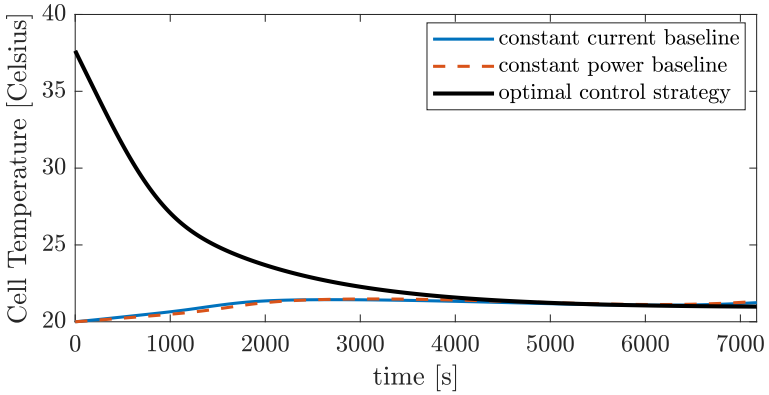

Figure 6.5: Cell temperature profiles of the simulation studies

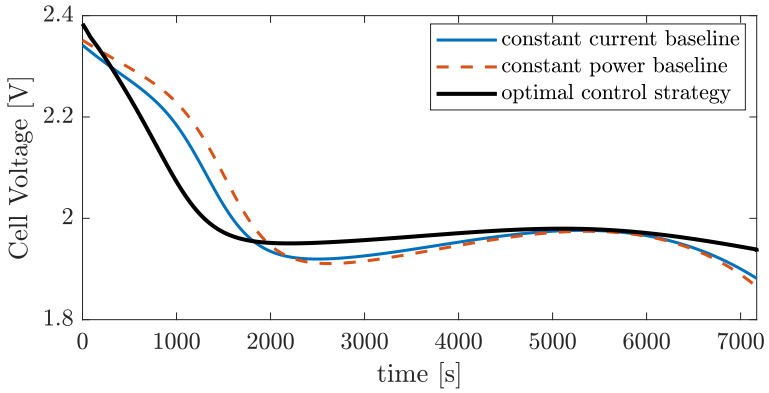

Figure 6.6: Cell voltage profiles of the three simulation studies

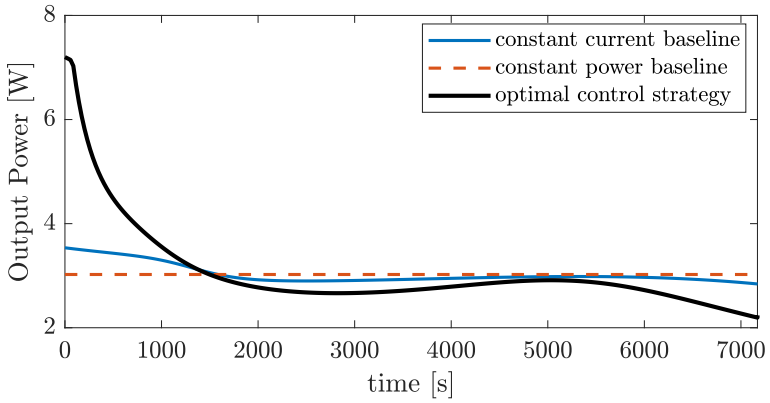

Figure 6.7: Cell output power profiles of the simulation studies

6.5.3 Results and Discussion

The discharge current, cell temperature, cell voltage, and output power profiles of the constant current, constant power and optimal strategy with free initial temperature are plotted in Fig. 6.4-6.7 respectively. The main outcomes of the simulation results are listed as follows.

Firstly, the results show that the optimal current control strategy with free initial temperature provides $22.16KJ$ total output energy during the 2-hour discharge time, 1.75% higher than the constant current and 1.83% higher than constant power discharge baseline. The optimal current control with the initial temperature $T_0 = T_{amb}$ provides 0.75% and 0.84% total output energy improvements compared to constant current and constant power discharge baselines. These output energy improvements may be modest, but they reveal some important insights regarding the discharge of Li-S batteries, as discussed further below.

Secondly, the energy release improvement from the optimal discharge strategy is higher when the initial temperature is free. This improvement comes from both

the optimal battery preheating and the optimal discharge current trajectory. This is due to the fact that higher temperature reduces the internal resistance of the Li-S battery, leading to less irreversible energy dissipation. Preheating consumes energy, but provides some benefit. Therefore, we can think of preheating as a form of pre-charging in the optimal control strategy.

Thirdly, the initial temperature of the optimal control strategy is 37.64°C, and it does not activate the maximum temperature constraint. This suggests that there exists an internal optimum for initial temperature. Although the internal resistance keeps decreasing with increasing temperature (higher than 37.6°C), the duration of the high voltage plateau shrinks, as shown in 6.3(a), leading to a lower energy output in the high plateau. This tradeoff explains the existence of an interior-optimal initial temperature.

Finally, the optimal current control strategy generates a power burst at the beginning of discharge. This suggests that to maximize the total output energy, it is better to use a higher discharge current in the high plateau region for Li-S batteries. The power burst can be explained by the high open circuit voltage and low internal resistance during the high plateau region. It is reasonable to extract more power, as the energy dissipation is lower and the high OCV can further increase the power level. This is perhaps the most important finding arising form this optimization studies: optimal discharge in Li-S batteries innately involves very high initial rates of discharge, corresponding to the high plateau region. Li-S batteries can therefore be used in applications characterized by a high initial power demand followed by a low power maintenance requirement. One such application is electrified flight,

where the demand power for takeoff is much larger than the power needed for en-route operation.

6.6 Conclusions

This chapter parameterizes a thermally-coupled Li-S battery ECM using experimental data in the existing literature. This model is further used to construct an optimal discharge strategy with the objective of maximizing total battery output energy. One can conclude that Li-S batteries have the potential to be used in applications requiring a high initial burst of power, followed by reduced power requirements. This is particularly appealing in the context of mobility applications where vehicle power requirements are much higher for launch compared to en-route operation, such as electrified air propulsion applications.

Chapter 7: Summary of Contributions

This dissertation focuses on the control-oriented study/analysis of Li-S batteries. It examines the problem of estimating the internal states of lithium-sulfur (Li-S) batteries based on an experimentally-parameterized multi-physics model, and optimizing the discharge current trajectory to maximize output power. Each chapter of this dissertation is summarized as follows.

Chapter 2 introduces the 2016-type prototype coin cell fabrication process in the laboratory. The cathode material consisted of a C/S composite with 70 wt% sulfur, KB EC60JD to form a conductive framework, and PVDF dissolved in NMP as a binder. A lithium chip with 0.6 mm thickness served as the anode. The electrolyte used here was 1M $LiTFSI$ and 4 wt% $LiNO_3$ in the dioxolane/dimethoxylethane mixture (DOL/DME = 1:1, V/V). Since there are few or no commercial Li-S batteries in the market currently, fabricating prototype cells is important to analyze the performance of the Li-S batteries. Cycling the prototype cells provides the experimental data to support the model parameterization.

Chapter 3 performs parameter sensitivity analysis and identification for a variety of zero-dimensional physics-based Li-S battery models. Due to the dependency between the parameters, a simulation-based sensitivity study is performed to pro-

vide guidance on the choice of to-be-identified parameters. These parameters are identified by fitting the simulated voltage profile to the experimental data for four models considering different reaction chains. Taking into account the importance of balancing parameter identification performance versus execution time, the best fitted model has the potential to be implemented online, and is suggested for the following state estimation study.

Chapter 4 examines the problem of estimating the internal states of the zero-dimensional model, which is parameterized based on the suggested reaction chain in Chapter 3. The model is reformulated from a set of differential algebraic equations (DAEs) to a set of ordinary differential equations (ODEs). Observability analysis reveals poor observability in the low plateau region, where cell voltage is less sensitive to precipitated sulfur mass. A reduced-order model is derived through mass conservation, showing attractive observability properties in both the high and low plateau regions. Simulation-based internal state estimation is performed on the physics-based Li-S model using an unscented Kalman filter. The simulation results illustrate the effectiveness of the estimator and show consistency with the fundamental discoveries of the observability analysis.

Chapter 5 demonstrates improved theoretical estimation error bounds on Li-S battery SOC by applying a periodic discharge current. This chapter employs Fisher information analysis based on a first order equivalent circuit model to quantify the estimation accuracy improvement. Experimental data from lab-made prototype coin cells is analyzed statistically, and is further used to parameterize the equivalent circuit model. This model is utilized in Monte Carlo simulation studies to

support this theoretical insight with 50% accuracy error bound improvement at a poor observability point.

Chapter 6 examines the problem of optimizing the discharge trajectory of a Li-S battery to maximize its energy release over a fixed time horizon. This optimization study utilizes a coupled thermal/electrical equivalent circuit model, based on the existing literature, that captures the dependence of battery resistance on both temperature and state of charge. The optimization problem is solved using direct collocation. Simulation results show that trajectory optimization improves total energy delivery over a 2-hour time window compared to both constant-current and constant-power discharge.

From a high-level perspective, this dissertation has six main conclusions. First, it is possible to construct Li-S battery management systems using experimentally parameterized dynamics models that capture the nonlinear underlying physics while remaining computationally tractable. Second, online estimation algorithms can be constructed based on these models, which is appealing because it provides real-time estimates of the distribution of active mass among different species. Third, fundamental pathways exist for addressing challenges pertaining to Li-S battery state observability. These pathways include the use of reduced-order state estimators as well as the exploitation of the dependence of battery resistance on SOC for more accurate state estimation. Fourth, the optimization of Li-S battery discharge trajectories can improve total energy release, particularly during the initial phases of discharge. Fifth, when examined together in their totality, the above conclusions suggest that model-based Li-S battery management is a feasible proposition. This

is important as a potential enabler for the commercial deployment of Li-S batteries. Sixth, the fact that model-based Li-S battery management is feasible despite critical challenges such as the nonlinearity of the underlying dynamics and multiplicity of underlying active species suggests that it may be important to examine additional Li-S battery estimation and control problems, beyond those discussed herein. Examples of such problems include Li-S state of health estimation, as well as trajectory optimization for Li-S battery charging (as opposed to discharging).

Bibliography

[1] Mark Wild and Gregory J Offer. *Lithium-Sulfur Batteries*. John Wiley & Sons, 2019.

[2] H Yanin and E Peled. Low-rate lithium/sulfur organic battery. In *Proc.-Electrochem. Soc.;(United States)*, volume 84. Department of Chemistry, Tel-Aviv University, Tel-Aviv, 1983.

[3] Jia-Qi Huang, Xiao-Fei Liu, Qiang Zhang, Cheng-Meng Chen, Meng-Qiang Zhao, Shu-Mao Zhang, Wancheng Zhu, Wei-Zhong Qian, and Fei Wei. Entrapment of sulfur in hierarchical porous graphene for lithium–sulfur batteries with high rate performance from- 40 to 60 c. *Nano Energy*, 2(2):314–321, 2013.

[4] Ian A Hunt, Yatish Patel, Maciej Szczygielski, Lukasz Kabacik, and Gregory J Offer. Lithium sulfur battery nail penetration test under load. *Journal of Energy Storage*, 2:25–29, 2015.

[5] Yuriy V Mikhaylik and James R Akridge. Polysulfide shuttle study in the li/s battery system. *Journal of The Electrochemical Society*, 151(11):A1969–A1976, 2004.

[6] Dominic Bresser, Stefano Passerini, and Bruno Scrosati. Recent progress and remaining challenges in sulfur-based lithium secondary batteries–a review. *Chemical communications*, 49(90):10545–10562, 2013.

[7] Hailiang Wang, Yuan Yang, Yongye Liang, Joshua Tucker Robinson, Yanguang Li, Ariel Jackson, Yi Cui, and Hongjie Dai. Graphene-wrapped sulfur particles as a rechargeable lithium–sulfur battery cathode material with high capacity and cycling stability. *Nano letters*, 11(7):2644–2647, 2011.

[8] Scott Evers and Linda F Nazar. New approaches for high energy density lithium–sulfur battery cathodes. *Accounts of chemical research*, 46(5):1135–1143, 2013.

[9] Min-Kyu Song, Elton J Cairns, and Yuegang Zhang. Lithium/sulfur batteries with high specific energy: old challenges and new opportunities. *Nanoscale*, 5(6):2186–2204, 2013.

[10] Jiangxuan Song, Mikhail L Gordin, Terrence Xu, Shuru Chen, Zhaoxin Yu, Hiesang Sohn, Jun Lu, Yang Ren, Yuhua Duan, and Donghai Wang. Strong lithium polysulfide chemisorption on electroactive sites of nitrogen-doped carbon composites for high-performance lithium–sulfur battery cathodes. *Angewandte Chemie*, 127(14):4399–4403, 2015.

[11] Zhe Yuan, Hong-Jie Peng, Ting-Zheng Hou, Jia-Qi Huang, Cheng-Meng Chen, Dai-Wei Wang, Xin-Bing Cheng, Fei Wei, and Qiang Zhang. Powering lithium–sulfur battery performance by propelling polysulfide redox at sulfiphilic hosts. *Nano letters*, 16(1):519–527, 2016.

[12] Karthikeyan Kumaresan, Yuriy Mikhaylik, and Ralph E White. A mathematical model for a lithium–sulfur cell. *Journal of The Electrochemical Society*, 155(8):A576–A582, 2008.

[13] David N Fronczek and Wolfgang G Bessler. Insight into lithium–sulfur batteries: Elementary kinetic modeling and impedance simulation. *Journal of power sources*, 244:183–188, 2013.

[14] Andreas F Hofmann, David N Fronczek, and Wolfgang G Bessler. Mechanistic modeling of polysulfide shuttle and capacity loss in lithium–sulfur batteries. *Journal of Power Sources*, 259:300–310, 2014.

[15] YX Ren, TS Zhao, M Liu, P Tan, and YK Zeng. Modeling of lithium-sulfur batteries incorporating the effect of li2s precipitation. *Journal of Power Sources*, 336:115–125, 2016.

[16] Petru Andrei, Chao Shen, and Jim P Zheng. Theoretical and experimental analysis of precipitation and solubility effects in lithium-sulfur batteries. *Electrochimica Acta*, 284:469–484, 2018.

[17] Timo Danner and Arnulf Latz. On the influence of nucleation and growth of s8 and li2s in lithium-sulfur batteries. *Electrochimica Acta*, 322:134719, 2019.

[18] Monica Marinescu, Teng Zhang, and Gregory J Offer. A zero dimensional model of lithium–sulfur batteries during charge and discharge. *Physical Chemistry Chemical Physics*, 18(1):584–593, 2016.

[19] Teng Zhang, Monica Marinescu, Laura O'Neill, Mark Wild, and Gregory Offer. Modeling the voltage loss mechanisms in lithium–sulfur cells: the importance of electrolyte resistance and precipitation kinetics. *Physical Chemistry Chemical Physics*, 17(35):22581–22586, 2015.

[20] M Wild, L O'neill, T Zhang, R Purkayastha, G Minton, M Marinescu, and GJ Offer. Lithium sulfur batteries, a mechanistic review. *Energy & Environmental Science*, 8(12):3477–3494, 2015.

[21] Arumugam Manthiram, Yongzhu Fu, Sheng-Heng Chung, Chenxi Zu, and Yu-Sheng Su. Rechargeable lithium–sulfur batteries. *Chemical reviews*, 114(23):11751–11787, 2014.

[22] Jonathan P Neidhardt, David N Fronczek, Thomas Jahnke, Timo Danner, Birger Horstmann, and Wolfgang G Bessler. A flexible framework for modeling multiple solid, liquid and gaseous phases in batteries and fuel cells. *Journal of the Electrochemical Society*, 159(9):A1528, 2012.

[23] Nisa Erisen, Nur Ber Emerce, Sevgi Can Erensoy, and Damla Eroglu. Modeling the effect of key cathode design parameters on the electrochemical performance of a lithium-sulfur battery. *International Journal of Energy Research*, 42(8):2631–2642, 2018.

[24] Nur Ber Emerce and Damla Eroglu. Effect of electrolyte-to-sulfur ratio in the cell on the li-s battery performance. *Journal of The Electrochemical Society*, 166(8):A1490, 2019.

[25] Nisa Erisen and Damla Eroglu. Modeling the discharge behavior of a lithium-sulfur battery. *International Journal of Energy Research*, 2020.

[26] Cheng Xiong, TS Zhao, YX Ren, HR Jiang, and XL Zhou. Mathematical modeling of the charging process of li-s batteries by incorporating the size-dependent li2s dissolution. *Electrochimica Acta*, 296:954–963, 2019.

[27] Timo Danner, Guanchen Zhu, Andreas F Hofmann, and Arnulf Latz. Modeling of nano-structured cathodes for improved lithium-sulfur batteries. *Electrochimica Acta*, 184:124–133, 2015.

[28] Vigneshwaran Thangavel, Kan-Hao Xue, Youcef Mammeri, Matias Quiroga, Afef Mastouri, Claude Guéry, Patrik Johansson, Mathieu Morcrette, and Alejandro A Franco. A microstructurally resolved model for li-s batteries assessing the impact of the cathode design on the discharge performance. *Journal of The Electrochemical Society*, 163(13):A2817, 2016.

[29] Vigneshwaran Thangavel, Oscar Xavier Guerrero, Matias Quiroga, Adelphe Matsiegui Mikala, Alexis Rucci, and Alejandro A Franco. A three dimensional kinetic monte carlo model for simulating the carbon/sulfur mesostructural evolutions of discharging lithium sulfur batteries. *Energy Storage Materials*, 24:472–485, 2020.

[30] Mahmoudreza Ghaznavi and P Chen. Sensitivity analysis of a mathematical model of lithium–sulfur cells part i: Applied discharge current and cathode conductivity. *Journal of power sources*, 257:394–401, 2014.

[31] M. Ghaznavi and P. Chen,. Sensitivity analysis of a mathematical model of lithium–sulfur cells: Part ii: Precipitation reaction kinetics and sulfur content. *Journal of Power Sources*, 257:402–411, 2014.

[32] Mahmoudreza Ghaznavi and P Chen. Analysis of a mathematical model of lithium-sulfur cells part iii: Electrochemical reaction kinetics, transport properties and charging. *Electrochimica Acta*, 137:575–585, 2014.

[33] Caitlin D Parke, Akshay Subramaniam, Suryanarayana Kolluri, Daniel T Schwartz, and Venkat R Subramanian. An efficient electrochemical tanks-in-series model for lithium-sulfur batteries. 2020.

[34] VS Kolosnitsyn, EV Kuzmina, EV Karaseva, and SE Mochalov. A study of the electrochemical processes in lithium–sulphur cells by impedance spectroscopy. *Journal of Power Sources*, 196(3):1478–1482, 2011.

[35] Zhaofeng Deng, Zhian Zhang, Yanqing Lai, Jin Liu, Jie Li, and Yexiang Liu. Electrochemical impedance spectroscopy study of a lithium/sulfur battery: modeling and analysis of capacity fading. *Journal of The Electrochemical Society*, 160(4):A553–A558, 2013.

[36] Vaclav Knap, Daniel-Ioan Stroe, Remus Teodorescu, Maciej Swierczynski, and Tiberiu Stanciu. Electrical circuit models for performance modeling of lithium-sulfur batteries. In *2015 IEEE Energy Conversion Congress and Exposition (ECCE)*, pages 1375–1381. IEEE, 2015.

[37] Karsten Propp, Monica Marinescu, Daniel J Auger, Laura O'Neill, Abbas Fotouhi, Karthik Somasundaram, Gregory J Offer, Geraint Minton, Stefano Longo, Mark Wild, et al. Multi-temperature state-dependent equivalent circuit discharge model for lithium-sulfur batteries. *Journal of Power Sources*, 328:289–299, 2016.

[38] Natalia A Cañas, Kei Hirose, Brigitta Pascucci, Norbert Wagner, K Andreas Friedrich, and Renate Hiesgen. Investigations of lithium–sulfur batteries using electrochemical impedance spectroscopy. *Electrochimica Acta*, 97:42–51, 2013.

[39] Jiuchun Jiang, Yan Liang, Qun Ju, Linjing Zhang, Weige Zhang, and Caiping Zhang. An equivalent circuit model for lithium-sulfur batteries. *Energy Procedia*, 105:3533–3538, 2017.

[40] Karsten Propp, Daniel J Auger, Abbas Fotouhi, Stefano Longo, and Vaclav Knap. Kalman-variant estimators for state of charge in lithium-sulfur batteries. *Journal of Power Sources*, 343:254–267, 2017.

[41] Abbas Fotouhi, Daniel J Auger, Karsten Propp, and Stefano Longo. Lithium–sulfur battery state-of-charge observability analysis and estimation. *IEEE Transactions on Power Electronics*, 33(7):5847–5859, 2017.

[42] Karsten Propp, Daniel J Auger, Abbas Fotouhi, Monica Marinescu, Vaclav Knap, and Stefano Longo. Improved state of charge estimation for lithium-sulfur batteries. *Journal of Energy Storage*, 26:100943, 2019.

[43] Zhihuo Wang, Abbas Fotouhi, and Daniel J Auger. State of charge estimation in lithium-sulfur cells using lstm recurrent neural networks. In *2020 European Control Conference (ECC)*, pages 1079–1085. IEEE, 2020.

[44] Martin Rolf Busche, Philipp Adelhelm, Heino Sommer, Holger Schneider, Klaus Leitner, and Jürgen Janek. Systematical electrochemical study on the parasitic shuttle-effect in lithium-sulfur-cells at different temperatures and different rates. *Journal of Power Sources*, 259:289–299, 2014.

[45] H Yamin and E Peled. Electrochemistry of a nonaqueous lithium/sulfur cell. *Journal of Power Sources*, 9(3):281–287, 1983.

[46] Duck-Rye Chang, Suck-Hyun Lee, Sun-Wook Kim, and Hee-Tak Kim. Binary electrolyte based on tetra (ethylene glycol) dimethyl ether and 1, 3-dioxolane for lithium–sulfur battery. *Journal of Power Sources*, 112(2):452–460, 2002.

[47] Daniel Ioan Stroe, Vaclav Knap, Maciej Swierczynski, and Erik Schaltz. Thermal behavior and heat generation modeling of lithium sulfur batteries. *Ecs Transactions*, 77(11):467–476, 2017.

[48] Reinhardt Klein, Nalin A Chaturvedi, Jake Christensen, Jasim Ahmed, Rolf Findeisen, and Aleksandar Kojic. Optimal charging strategies in lithium-ion battery. In *Proceedings of the 2011 american Control Conference*, pages 382–387. IEEE, 2011.

[49] Marcello Torchio, Nicolas A Wolff, Davide M Raimondo, Lalo Magni, Ulrike Krewer, R Bushan Gopaluni, Joel A Paulson, and Richard D Braatz. Real-time model predictive control for the optimal charging of a lithium-ion battery. In *2015 American Control Conference (ACC)*, pages 4536–4541. IEEE, 2015.

[50] Guoxing Li, Yue Gao, Xin He, Qingquan Huang, Shuru Chen, Seong H Kim, and Donghai Wang. Organosulfide-plasticized solid-electrolyte interphase layer enables stable lithium metal anodes for long-cycle lithium-sulfur batteries. *Nature communications*, 8:850, 2017.

[51] Natalia A Cañas. *Fabrication and Characterization of Lithium–Sulfur Batteries*. PhD thesis, Universität Stuttgart, 2015.

[52] Pankaj Arora and Zhengming Zhang. Battery separators. *Chemical reviews*, 104(10):4419–4462, 2004.

[53] Mumin Rao, Xiangyun Song, and Elton J Cairns. Nano-carbon/sulfur composite cathode materials with carbon nanofiber as electrical conductor for advanced secondary lithium/sulfur cells. *Journal of Power Sources*, 205:474–478, 2012.

[54] John Cannarella and Craig B Arnold. Ion transport restriction in mechanically strained separator membranes. *Journal of Power Sources*, 226:149–155, 2013.

[55] Demir-cakan Rezan. *Li-S Batteries: The Challenges, Chemistry, Materials, and Future Perspectives*. # N/A, 2017.

[56] Chu Xu, Timothy Cleary, Guoxing Li, Donghai Wang, and Hosam Fathy. Parameter identification and sensitivity analysis for zero-dimensional physics-based lithium-sulfur battery models. *ASME Letters in Dynamic Systems and Control*, 1(4):041001, 2021.

[57] Abbas Fotouhi, Daniel J Auger, Karsten Propp, Stefano Longo, Rajlakshmi Purkayastha, Laura O'Neill, and Sylwia Waluś. Lithium–sulfur cell equivalent circuit network model parameterization and sensitivity analysis. *IEEE Transactions on Vehicular Technology*, 66(9):7711–7721, 2017.

[58] Peter Fritzson, Peter Aronsson, Adrian Pop, Hakan Lundvall, Kaj Nystrom, Levon Saldamli, David Broman, and Anders Sandholm. Openmodelica-a free open-source environment for system modeling, simulation, and teaching. In *2006 IEEE Conference on Computer Aided Control System Design, 2006 IEEE International Conference on Control Applications, 2006 IEEE International Symposium on Intelligent Control*, pages 1588–1595. IEEE, 2006.

[59] Mahsa Doosthosseini, Elsa Hansen, and Hosam K Fathy. On the accuracy of drug-resistant cell population estimation from total cancer size measurements. In *2019 18th European Control Conference (ECC)*, pages 343–350. IEEE, 2019.

[60] J Kennedy and R Eberhart. Particle swarm optimization (pso). In *Proc. IEEE International Conference on Neural Networks, Perth, Australia*, pages 1942–1948, 1995.

[61] Chu Xu, Timothy Cleary, Daiwei Wang, Guoxing Li, Christopher Rahn, Donghai Wang, Rajesh Rajamani, and Hosam K Fathy. Online state estimation for a physics-based lithium-sulfur battery model. *Journal of Power Sources*, 489:229495, 2021.

[62] Ji Liu, Sergio Mendoza, and Hosam K Fathy. Total least squares state of charge estimation for lithium-ion batteries: An efficient moving horizon estimation approach. *IFAC-PapersOnLine*, 50(1):14489–14494, 2017.

[63] Shunli Wang, Carlos Fernandez, Chunmei Yu, Yongcun Fan, Wen Cao, and Daniel-Ioan Stroe. A novel charged state prediction method of the lithium ion battery packs based on the composite equivalent modeling and improved splice kalman filtering algorithm. *Journal of Power Sources*, 471:228450, 2020.

[64] Xiaosong Hu, Haifu Jiang, Fei Feng, and Bo Liu. An enhanced multi-state estimation hierarchy for advanced lithium-ion battery management. *Applied Energy*, 257:114019, 2020.

[65] Weihan Li, Yue Fan, Florian Ringbeck, Dominik Jöst, Xuebing Han, Minggao Ouyang, and Dirk Uwe Sauer. Electrochemical model-based state estimation for

lithium-ion batteries with adaptive unscented kalman filter. *Journal of Power Sources*, 476:228534, 2020.

[66] Abbas Fotouhi, Daniel J Auger, Laura O'Neill, Tom Cleaver, and Sylwia Walus. Lithium-sulfur battery technology readiness and applications—a review. *Energies*, 10(12):1937, 2017.

[67] Mohamed Boutayeb and Mohamed Darouach. Observers design for nonlinear descriptor systems. In *Proceedings of 1995 34th IEEE Conference on Decision and Control*, volume 3, pages 2369–2374. IEEE, 1995.

[68] Victor Manuel Becerra, PD Roberts, and GW Griffiths. Applying the extended kalman filter to systems described by nonlinear differential-algebraic equations. *Control Engineering Practice*, 9(3):267–281, 2001.

[69] Linda Petzold. Differential/algebraic equations are not ode's. *SIAM Journal on Scientific and Statistical Computing*, 3(3):367–384, 1982.

[70] Matthew T Lawder, Venkatasailanathan Ramadesigan, Bharatkumar Suthar, and Venkat R Subramanian. Extending explicit and linearly implicit ode solvers for index-1 daes. *Computers & Chemical Engineering*, 82:283–292, 2015.

[71] Robert Hermann and Arthur Krener. Nonlinear controllability and observability. *IEEE Transactions on automatic control*, 22(5):728–740, 1977.

[72] Nathan D Powel and Kristi A Morgansen. Empirical observability gramian rank condition for weak observability of nonlinear systems with control. In *2015 54th IEEE Conference on Decision and Control (CDC)*, pages 6342–6348. IEEE, 2015.

[73] John D Gorman and Alfred O Hero. Lower bounds for parametric estimation with constraints. *IEEE Transactions on Information Theory*, 36(6):1285–1301, 1990.

[74] John P Norton. *An introduction to identification*. Courier Corporation, 2009.

[75] Aabhas Sharma and Hosam K Fathy. Fisher identifiability analysis for a periodically-excited equivalent-circuit lithium-ion battery model. In *2014 American Control Conference*, pages 274–280. IEEE, 2014.

[76] Eric A Wan and Rudolph Van Der Merwe. The unscented kalman filter for nonlinear estimation. In *Proceedings of the IEEE 2000 Adaptive Systems for Signal Processing, Communications, and Control Symposium (Cat. No. 00EX373)*, pages 153–158. Ieee, 2000.

[77] Eric A Wan, Rudolph Van Der Merwe, and Simon Haykin. The unscented kalman filter. *Kalman filtering and neural networks*, 5(2007):221–280, 2001.

[78] Simo Sarkka. On unscented kalman filtering for state estimation of continuous-time nonlinear systems. *IEEE Transactions on automatic control*, 52(9):1631–1641, 2007.

[79] Shi Zhao, Stephen R Duncan, and David A Howey. Observability analysis and state estimation of lithium-ion batteries in the presence of sensor biases. *IEEE Transactions on Control Systems Technology*, 25(1):326–333, 2016.

[80] Michael J Rothenberger, Joel Anstrom, Sean Brennan, and Hosam K Fathy. Maximizing parameter identifiability of an equivalent-circuit battery model using optimal periodic input shaping. In *ASME 2014 Dynamic Systems and Control Conference*. American Society of Mechanical Engineers Digital Collection, 2014.

[81] C Radhakrishna Rao. Information and the accuracy attainable in the estimation of statistical parameters. *Reson. J. Sci. Educ*, 20:78–90, 1945.

[82] D Bernardi, E Pawlikowski, and John Newman. A general energy balance for battery systems. *Journal of the electrochemical society*, 132(1):5, 1985.

[83] Xiao Hua, Teng Zhang, Gregory J Offer, and Monica Marinescu. Towards online tracking of the shuttle effect in lithium sulfur batteries using differential thermal voltammetry. *Journal of Energy Storage*, 21:765–772, 2019.

[84] Matthew Kelly. An introduction to trajectory optimization: How to do your own direct collocation. *SIAM Review*, 59(4):849–904, 2017.